



The
University
Of
Sheffield.

Access to Electronic Thesis

Author: Da Xu
Thesis title: Reconstruction and applications of QED final state radiation photons in $Z \rightarrow \mu\mu$ decays produced in 7 TeV proton-proton collisions at the Large Hadron Collider
Qualification: PhD

This electronic thesis is protected by the Copyright, Designs and Patents Act 1988. No reproduction is permitted without consent of the author. It is also protected by the Creative Commons Licence allowing Attributions-Non-commercial-No derivatives.

If this electronic thesis has been edited by the author it will be indicated as such on the title page and in the text.



**Reconstruction and applications of QED
final state radiation photons in $Z \rightarrow \mu\mu$
decays produced in 7 TeV proton-proton
collisions at the Large Hadron Collider**

Da Xu

Supervisor: Stathes Paganis

**A Thesis Submitted for the Degree of Doctor Of
Philosophy in Physics**

**Department of Physics and Astronomy
University of Sheffield**

To my dear Dad♥Mum

ABSTRACT

This thesis presents a method for including the final state radiation (FSR) photon in the reconstruction of Z bosons decaying into pairs of muons ($Z \rightarrow \mu\mu\gamma$). An algorithm for the reconstruction of FSR photons has been developed. The FSR photon candidates with $E_{T,\gamma} > 1.3$ GeV are reconstructed within a $\Delta R_{\gamma,\mu} < 0.15$ cone about the axis defined by the muon momentum direction at the interaction point, using the liquid argon calorimeter of ATLAS and a special clustering efficient at low energies. Based on an integrated luminosity of 164 pb^{-1} , the cross-section of the $Z \rightarrow \mu\mu\gamma$ events with at least one FSR photon within fiducial region ($E_{T,\gamma} > 1.3$ GeV and $\Delta R_{\gamma,\mu} < 0.15$) is measured: $\sigma_{Z \rightarrow \mu\mu\gamma}^{fid} = 0.073 \pm 0.001(\text{stat}) \pm 0.006(\text{sys}) \pm 0.002(\text{lum}) \text{ nb}$. This is consistent with the expectation from a NNLO QCD calculation including QED FSR. Photons within the fiducial region are reconstructed with a 70% average efficiency which increases to 85% for $E_T > 4$ GeV. Inclusion of these photons in the dimuon invariant mass calculation was shown to lead to improved Z-boson invariant mass resolution and scale: a Gaussian fit shows that the peak of the distribution moves from 89 GeV to 91.31 ± 0.06 GeV with a standard deviation of 2.5 ± 0.07 GeV. A $\simeq 20\%$ of all inclusive $Z \rightarrow \mu\mu$ events are corrected in the tail of the invariant mass ($M < 80$ GeV). Moreover, based on a test with simulated Higgs $\rightarrow ZZ^* \rightarrow 4\mu$ samples, more than 20% of the events are expected to find a reconstructed FSR photon around. The improvement of the Higgs invariant mass resolution and scale by adding the reconstructed FSR photons is presented.

ACKNOWLEDGMENTS

I would like to record my gratitude to my supervisor, Stathes Paganis, for his patience, motivation, enthusiasm, and immense knowledge. Without his guidance and support, this thesis would not have been possible. I gratefully acknowledge Christos Anastopoulos for his valuable advices and constant help. I heartily thank Hongbo Zhu, Nicolas Kerschen, Tulay Donszelmann, for their insightful comments and kindly help. I would also like to thank Dan Tovey, Davide Costanzo, Matt Robinson, and all other members of the High Energy Physics group at the University of Sheffield, for their help. It has been a pleasure working with them. Finally, I am grateful to my family for their support during all these years.

This work was supported by the China Scholarship Council (CSC) and the Science and Technology Facilities Council (STFC).

Contents

1	Introduction	1
2	The Standard Model	4
2.1	Particles and Interactions	4
2.2	The Electroweak Theory	7
2.3	The Higgs Mechanism	10
3	The Drell-Yan Process	15
3.1	The leading order Drell-Yan model	15
3.1.1	Parton Distribution Functions	15
3.1.2	The dynamics of the Drell-Yan process	19
3.1.3	Cross-section formalism	20
3.2	High order QCD corrections	22
3.2.1	Feynman diagrams	24
3.2.2	Theoretical calculations	24
3.3	High order electroweak corrections	26
3.3.1	Feynman diagrams	26

3.3.2	Theoretical predictions	27
3.4	Monte-Carlo Event Generation	31
3.4.1	Hard process	32
3.4.2	Initial- and final-state radiation	33
3.4.3	Hadronisation and hadron decays	34
3.4.4	Multiple parton interactions (MPI)	35
3.4.5	MC generators for ATLAS	35
4	The ATLAS Experiment at the Large Hadron Collider	40
4.1	Large Hadron Collider	40
4.2	ATLAS Detector	43
4.2.1	Inner Detector	44
4.2.2	Calorimeters	47
4.2.3	Muon Spectrometer	53
4.2.4	Forward Detectors	55
4.2.5	Magnet System	57
4.2.6	Trigger and Data Acquisition	57
4.3	ATLAS Offline Software	60
4.3.1	The Athena Framework	60
4.3.2	The Simulation Data Flow	60
5	Event Reconstruction	64
5.1	Muon Reconstruction	64
5.1.1	Muon Trigger	64

5.1.2	Muon Reconstruction	67
5.2	EM Cluster Reconstruction	70
5.2.1	Topological clustering	71
5.2.2	Sliding-Window clustering	72
5.2.3	EM Calibration	73
6	Reconstruction of QED final state radiation photons in $Z \rightarrow \mu\mu$ decays in 7 TeV pp collisions	80
6.1	Introduction	80
6.2	Data and Monte Carlo Samples	81
6.2.1	Data Samples	82
6.2.2	Simulated Event Samples	82
6.2.3	Photon Final State Radiation at generator level	82
6.3	Event Selection	85
6.3.1	Preselection: $Z \rightarrow \mu\mu$ candidates	85
6.3.2	Final selection: $Z \rightarrow \mu\mu\gamma$ candidates	87
6.4	FSR Photon Reconstruction Performance	94
6.4.1	Special low energy clustering: EM topo-seeded clustering	94
6.4.2	Photon Cluster Energy Calibration	95
6.5	Measurements of the $Z \rightarrow \mu\mu\gamma$ yields and the fiducial cross-section	97
6.5.1	Correction of MC predictions for trigger efficiency	104
6.5.2	Measurements of the $Z \rightarrow \mu\mu\gamma$ yields	106
6.5.3	Measurement of the $Z \rightarrow \mu\mu\gamma$ fiducial cross-section	112
6.6	Systematic Uncertainties	113

6.6.1	Theoretical uncertainties	113
6.6.2	Systematic Uncertainties due to the event selection	114
6.6.3	Systematic uncertainties on the background normalization	115
6.6.4	Summary	119
6.7	Improvement of the Z invariant mass	119
6.8	Pile-up effects and Monte Carlo reweighting	126
6.9	Conclusions	128
7	Improving the invariant mass of Higgs $\rightarrow ZZ^* \rightarrow 4l(l = e, \mu)$ by adding FSR photons	133
7.1	Introduction	133
7.2	Monte Carlo Samples	134
7.3	Analysis Overview	134
7.4	Results	135
7.5	Conclusion	140
8	Summary	141
A	Monte Carlo Event Generator	143
B	FSR Tool	146

List of Figures

2.1	A potential that leads to spontaneous symmetry breaking.	11
2.2	Exclusion regions for the mass of the Higgs, updated with results from the Tevatron.	13
2.3	Experimental limits from ATLAS on Standard Model (SM) Higgs production in the mass range 110-600 GeV. The solid curve reflects the observed experimental limits, expressed in terms of the ratio (μ) of the observed cross-section to the cross-section predicted by the SM (vertical axis), for the production of Higgs for each possible mass value (horizontal axis). The region for which the solid curve dips below the horizontal line at the value of 1 is excluded with a 95% confidence level (CL). The dashed curve shows the expected limit in the absence of the Higgs boson, based on simulations. The green and yellow bands correspond (respectively) to 68%, and 95% confidence level regions from the expected limits.	14
3.1	Illustration of Drell-Yan process in case of γ^*/Z	16
3.2	Standard Model cross-sections at the Tevatron and the LHC as function of the centre-of-mass energy.	18
3.3	Parton distribution functions as determined for the CT10 PDF set evaluated at $\mu(Q)=2$ GeV.	18

3.4	Neutral current Drell-Yan scattering cross section (top plot), as a function of the mass M of the e^+e^- pair integrated over the boson rapidity y . At small M the cross section is dominated by the pure photon contribution. The Z part determines the resonance region. The photon and Z unify at large M . The γZ interference contribution is shown in absolute value. The relative fraction of the interference cross section to the total Born cross section is shown in the bottom plot. The γZ interference changes sign at $M = M_Z$	23
3.5	The Feynman diagram for the first-order Drell-Yan process in QCD: (a) the annihilation graph with the vertex correction; (b) and (c) are the annihilation digrams involving gluon emission in the final state; (d) and (e) are Compton diagrams.	24
3.6	Vertex and box diagrams for weak $O(\alpha)$ corrections with light incoming quarks $q = u, d, c, s, b$	28
3.7	Diagrams for photonic $O(\alpha)$ corrections.	29
3.8	Dilepton invariant mass distribution and the relative EW NLO correction factors at the LHC in the resonance region and the high-invariant-mass region.	30
3.9	Dilepton invariant mass distribution and the relative EW correction factors beyond $O(\alpha)$ at the LHC in the resonance region and the high-invariant-mass region.	31
4.1	Schematic layout of the LHC injector chain.	41
4.2	Cumulative luminosity versus day delivered to (green), and recorded by ATLAS (yellow) during stable beams for pp collisions at $\sqrt{s} = 7$ TeV in 2010(left) and 2011(right). The left plot is shown in logarithmic scale.	42
4.3	Cut-away view of the ATLAS detector. The dimensions of the detector are 25 m in height and 44 m in length. The overall weight is approximately 7000 tonnes.	43
4.4	Plan view of a quarter-section of the ATLAS inner detector showing each of the major detector elements with its active dimensions and envelopes.	45

4.5	Cumulative amount of material, in units of interaction length, as a function of $ \eta $, in front of the electromagnetic calorimeters, in the electromagnetic calorimeters, in each hadronic layer, and the total amount at the end of the active calorimetry.	48
4.6	A sketch of a barrel module of the EM calorimeter.	50
4.7	Measured 3×3 cluster energy distributions in the range $0.3 < \eta < 0.4$ in the LAr EM calorimeter, using cosmic muons.	51
4.8	Left: Cross-section of the barrel muon system perpendicular to the beam axis (non-bending plane), showing three concentric cylindrical layers of eight large and eight small chambers. Right: Cross-section of the muon system in a plane containing the beam axis (bending plane). Infinite-momentum muons would propagate along straight trajectories which are illustrated by the dashed lines and typically traverse three muon stations.	54
4.9	Placement of the forward detectors along the beam-line around the ATLAS interaction point (IP).	56
4.10	Geometry of magnet windings and tile calorimeter steel.	57
4.11	Block diagram depicting the interactions, connections, hardware and data-flow of the trigger and data acquisition systems.	59
4.12	Athena Component Model.	61
4.13	The simulation data flow. Rectangles represent processing stages and rounded rectangles represent objects within the event data model. Pile-up and ROD emulation are optional processing stages.	62
5.1	Muon “Vertical” Slice diagram.	65
5.2	Schematic view of an electromagnetic shower developing in the ATLAS LAr calorimeter.	75
5.3	The longitudinal weights s , b , W_0 and W_3 as a function of $ \eta $	77
5.4	Mean fractional-energy deviation from truth (points) and energy resolution (error bars) as a function of $ \eta $ before (left) and after (right) calibration.	78

6.1	(a) Fraction of $Z \rightarrow \mu\mu$ events with zero, one or more FSR photons, (b) fraction of events as a function of the leading FSR photon transverse energy and (c) fraction of events as a function of $\Delta R(=\sqrt{\Delta\eta^2 + \Delta\varphi^2})$ between the leading FSR photon and the radiating muon at generator level. Note that in the generator PHOTOS the value of the infrared cut-off parameter E_γ^{min}/M is set to $\sim 10^{-7}$ in the CMS frame of the decaying Z boson.	84
6.2	Distributions of f_1 and $\Delta R_{cluster,\mu}$ discriminants from $Z \rightarrow \mu\mu$ Monte Carlo: the f_1 distribution (top) is shown after an $E_T > 1.3$ GeV cut. The $\Delta R_{cluster,\mu}$ distribution (bottom) is shown after the $E_T > 1.3$ GeV and $f_1 > 0.15$ cuts. Black histograms correspond to signal. The backgrounds are shown in coloured filled histograms (μ background in blue and hadronic background in green).	89
6.3	Distributions of f_1 and $\Delta R_{cluster,\mu}$ discriminants from $Z \rightarrow \mu\mu$ Monte Carlo: the $\Delta R_{cluster,\mu}$ distribution (top) is shown after an $E_T > 1.3$ GeV cut. The f_1 distribution (bottom) is shown after the $E_T > 1.3$ GeV and $\Delta R_{cluster,\mu} < 0.15$ cuts. Black histograms correspond to signal. The backgrounds are shown in coloured filled histograms (μ background in blue and hadronic background in green).	90
6.4	2D correlation plots of discriminants f_1 and $\Delta R_{cluster,\mu}$ after an $E_T > 1.3$ GeV cut from $Z \rightarrow \mu\mu$ Monte Carlo. The FSR signal $Z \rightarrow \mu\mu\gamma$ is shown in (a). The μ background (clusters produced by muon ionization in the LAr calorimeter) is shown in (b) and the hadronic background (clusters generated by hadrons) in (c). The same distributions for the signal and the two background components is shown in (d).	92
6.5	Fraction of $Z \rightarrow \mu\mu$ events with a fake photon as a function of $\Delta R_{cluster,\mu}$. These events are obtained from $Z \rightarrow \mu\mu$ Monte Carlo events without any QED FSR radiation. The fake fraction is defined as the ratio of the events passing the full event selection divided by all $Z \rightarrow \mu\mu$ events without FSR radiation. The top figure shows the fake fraction for $E_T > 1.3$ GeV region. The bottom figure focuses in the $E_T > 3$ GeV region. The statistic errors are negligible.	93

6.6	Top (Data vs MC): reconstructed EM topo-seeded 3×5 photon cluster E_T compared to the standard sliding-window cluster E_T after final selection for data and $Z \rightarrow \mu\mu\gamma$ MC. The MC is normalized to the data luminosity. The EM topo-seeded clustering used in this work extends the photon acceptance to lower E_T . Bottom (MC-only): E_T distributions for reconstructed photon clusters matched to true FSR photons for the two different clusterings.	96
6.7	Calibrated photon energy resolution in bins of energy before applying a cluster energy correction.	98
6.8	Calibrated photon energy resolution in bins of energy after application of a correction for the overlapping muon energy (see text).	99
6.9	Calibrated photon energy resolution in bins of eta before applying a cluster energy correction.	100
6.10	Calibrated photon energy resolution in bins of eta after application of a correction for the overlapping muon energy (see text).	101
6.11	Photon energy linearity (top) and uniformity (bottom) before photon energy correction.	102
6.12	Photon energy linearity (top) and uniformity (bottom) after photon energy correction.	103
6.13	The trigger efficiencies as a function of p_T , η and φ with respect to selected muons, for barrel region and endcap region.	105
6.14	FSR photon transverse energy, energy, $ \eta $, φ , f_1 and $\Delta R_{\text{cluster},\mu}$ for events passing Z-boson preselection and FSR search.	109
6.15	FSR photon transverse energy, energy, $ \eta $, φ , f_1 and $\Delta R_{\text{cluster},\mu}$ for events passing the FSR final selection.	110
6.16	Efficiency as a function of true FSR photon transverse energy, energy, $ \eta $, φ and $\Delta R_{\gamma,\mu}$	111
6.17	Comparison between Data and MC for reconstructed FSR photon E_T	116
6.18	Comparison between Data and MC for reconstructed FSR photon f_1	117

6.19	Comparison between Data and MC for reconstructed FSR photon $\Delta R_{\text{cluster},\mu}$	118
6.20	Control plots for the background normalization in a background-rich region defined by an $f_1 < 0.15$ cut inversion. The photon candidate transverse energy, energy, $ \eta $, φ and $\Delta R_{\text{cluster},\mu}$ for events passing the inverted cut are shown for data and MC. As an example, an uncertainty band of $\pm 20\%$ for the background is also shown. Based on these studies a 20% uncertainty on the background normalization has been considered leading to a 7.6% uncertainty contribution to the predicted $Z \rightarrow \mu\mu\gamma$ yields.	120
6.21	Z-boson invariant mass distribution for events passing the event selection, before and after the addition of the reconstructed candidate FSR photons.	121
6.22	Z invariant mass distribution for events passing the event selection, before the addition of the reconstructed FSR photons, with signal shown in blue and yellow.	123
6.23	Z invariant mass distribution for events passing the event selection, after the addition of the reconstructed FSR photons, with signal shown in blue and yellow.	124
6.24	Fraction of corrected $Z \rightarrow \mu\mu\gamma$ signal events with respect to the total inclusive $Z \rightarrow \mu\mu$ events.	125
6.25	$\Delta R_{\text{cluster},\mu}$ distribution between the cluster and the closest muon ($E_T > 1$ GeV) in linear scale (top) and log scale (bottom) before pile-up reweighting.	127
6.26	$\Delta R_{\text{cluster},\mu}$ distribution between the cluster and the closest muon for fixed number of pile-up vertices ($N_{pv} = 5$) in linear scale (top) and log scale (bottom).	129
6.27	$\Delta R_{\text{cluster},\mu}$ distribution between the cluster and the closest muon for fixed number of pile-up vertices ($N_{pv} = 7$) in linear scale (top) and log scale (bottom).	130
6.28	$\Delta R_{\text{cluster},\mu}$ distribution between the cluster and the closest muon ($E_T > 1$ GeV) in linear scale (top) and log scale (bottom) after pile-up reweighting.	131

6.29	$\Delta R_{\text{cluster},\mu}$ distribution between the cluster and the closest muon ($E_T > 3$ GeV) in linear scale (top) and log scale (bottom) after pile-up reweighting.	132
7.1	Higgs $\rightarrow 4\mu$ invariant mass distributions after addition of true FSR photons.	136
7.2	Higgs $\rightarrow 4\mu$ invariant mass distributions after addition of reconstructed FSR photons.	137
7.3	Higgs $\rightarrow 4\mu$ invariant mass distributions after addition of reconstructed FSR photons for the corrected events.	138
B.1	Z boson invariant mass for events for which at least one FSR photon was found, before and after the addition of the reconstructed photons (with $E_T > 4$ GeV), using 2011 data from period B to period K. . . .	148
B.2	Z boson invariant mass for events for which at least one FSR photon was found, before and after the addition of the reconstructed photons (with $E_T > 10$ GeV), using 2011 data from period B to period K. . .	149

List of Tables

2.1	Fermions of the Standard Model.	5
2.2	Gauge interactions in Standard Model.	5
3.1	$Z/\gamma^* \rightarrow ll$ and $Z \rightarrow ll$ cross sections in pb up to LO, NLO and NNLO in QCD corrections calculated from FEWZ using the MSTW2008NNLO PDF set. Note the difference between the notations Z/γ^* and Z , the former includes γ^* contribution while the latter does not.	25
3.2	Input parameters used for the cross section calculations.	26
3.3	Tunned comparison of LO and EW NLO predictions for $p\bar{p} \rightarrow Z/\gamma^* \rightarrow \mu^+\mu^-$ at LHC ($\sqrt{s} = 14$ TeV).	27
5.1	The two main families of muon collections and their corresponding algorithms.	67
5.2	Cluster size for different egamma particle types in the barrel and end-cap region of the EM calorimeter.	73
6.1	Summary of Monte Carlo samples and generators used in the simulation. The W and Z cross-sections are normalized to NNLO cross-sections as provided by the FEWZ program. The $t\bar{t}$ cross-section normalization is at an approximate NNLO cross-section using the CTEQ66 PDF set.	83

6.2	Fractions of $Z \rightarrow \mu\mu$ events with at least one radiated photon with respect to the inclusive $Z \rightarrow \mu\mu$ events at generator level. A 13% of the inclusive $Z \rightarrow \mu\mu$ events are expected to have at least one FSR photon with $E_{T,\gamma}$ greater than 1.3 GeV. For half of these events, the photons are radiated within a 0.15 cone around the emitting muon. Only 7% of the inclusive $Z \rightarrow \mu\mu$ events are expected to have at least one radiated photon with $E_{T,\gamma} > 1.3$ GeV and $\Delta R_{\gamma,\mu} < 0.15$. As shown in the last row, the probability for both muons to have radiated a photon with $E_{T,\gamma} > 1.3$ GeV and $\Delta R_{\gamma,\mu} < 0.15$, is at the 0.1% level. The statistic errors are negligible.	85
6.3	Summary of event preselection criteria.	86
6.4	FSR analysis cutflow.	87
6.5	Fractions of different background components after each step of FSR analysis cutflow.	91
6.6	Expected yield of $Z \rightarrow \mu\mu\gamma$ signal and background events (in pb) passing each step of the final selection.	94
6.7	Cut-flow table for MC signal $Z \rightarrow \mu\mu\gamma$ events. The predicted event numbers are not corrected for trigger efficiency, but they are reweighted to match the pile-up vertex distribution in data. The efficiencies have been investigated systematically by varying the corresponding cut values. The accuracy on efficiency is $\pm 1\%$ due to systematics (see Section 6.6 for more details). The statistic errors are negligible.	104
6.8	Summary of the muon trigger efficiencies and scale factor for EF_mu18_MG , with statistic errors. The statistic errors on ϵ_{MC} are negligible.	104
6.9	Numbers and fractions of Z events in Monte Carlo in which two muons go into each of the three possible combinations of barrel and endcap.	107
6.10	Event trigger efficiencies in data and MC for $Z \rightarrow \mu\mu$ events in which two muons go into each of the three possible combinations of barrel and endcap. The statistic errors on ϵ_{MC} are negligible.	107
6.11	Summary of the trigger efficiencies for data and MC, and scale factor. The statistic errors on ϵ_{MC} are negligible.	107

6.12	Cut-flow table for data and Monte Carlo corresponding to an integrated luminosity of 164 pb^{-1} . The Monte Carlo has been corrected for trigger efficiency and has been normalized to the full integrated luminosity. A $Z \rightarrow \mu\mu\gamma$ event will pass a particular cut only if at least one photon cluster is found that passes the cut. The statistic errors are negligible.	108
6.13	Summary of input quantities to the calculation of the $Z \rightarrow \mu\mu\gamma$ fiducial cross-section. N^{Signal} is the observed number of signal events after background subtraction, L_{int} is the integrated luminosity and C_{FSR} is an efficiency correction factor. The trigger efficiency scale factors used to correct the simulation for differences between data and MC are included in C_{FSR} . The statistic errors are negligible.	112
6.14	Systematic uncertainty on $Z \rightarrow \mu\mu\gamma$ yields due to the photon $E_{T,\gamma}$ cut.	115
6.15	Systematic uncertainty on $Z \rightarrow \mu\mu\gamma$ yields due to the photon $\Delta R_{\gamma,\mu}$ cut.	115
6.16	Systematic uncertainty on $Z \rightarrow \mu\mu\gamma$ yields due to the photon f_1 cut.	115
6.17	Systematic Uncertainties.	119
6.18	Effect of adding the FSR photon to the invariant $Z \rightarrow \mu\mu$ mass as a function of the mass. A significant fraction ($\simeq 20\%$) of the inclusive $Z \rightarrow \mu\mu$ events are corrected in the tail of the distribution. These events (signal to the 90% level) are moved to the bulk of the invariant mass distribution, as shown in the last two rows using Monte Carlo.	122
7.1	Monte Carlo samples used.	134
7.2	Number of events within $[-\sigma, +\sigma]$ around central Higgs mass.	139
7.3	Number of events within $[-2\sigma, +2\sigma]$ around central Higgs mass.	139
A.1	Specific purpose generators.	143
A.2	Parton level generators.	144
A.3	Full generators.	145

Chapter 1

Introduction

The production of electroweak (EW) gauge bosons provides a standard candle for hadronic high-energy colliders as the Tevatron and the Large Hadron Collider (LHC). It offers precise determinations of several Standard Model (SM) parameters, and places stringent constraints on many forms of new physics. At the LHC, an enormous number of W and Z bosons is collected. Good control of the radiative corrections becomes vital not only for the assessment of the overall experimental error of the physics measurements, but also for the shapes of the distributions [1].

The measurement of the QED Final State Photon Radiation (FSR) from Z and W boson leptonic decays is necessary for controlling QED radiative corrections in W/Z boson cross-section predictions. Experimental control of QED radiation from weak-boson lines is also important for reducing the systematic uncertainties in the measurement of the W mass and width. Currently in ATLAS, in the process of the muon pair production, the Z line shape is obtained from measuring the invariant mass distribution of the $\mu^+\mu^-$ pair, which is distorted due to the missing FSR [2].

A method for including the FSR photons in the reconstruction of Z bosons decaying into pairs of muons ($Z^1 \rightarrow \mu\mu\gamma$) is provided in this thesis. An algorithm for the reconstruction of FSR photons has been developed using a special clustering algorithm. The main application of FSR analysis is the improvement of the Z invariant mass. QED FSR photons emitted from the $Z \rightarrow \mu\mu$ lines can be reconstructed with the liquid argon (LAr) calorimeter of ATLAS: one searches for electromagnetic (EM) clusters within a narrow cone about the axis defined by the muon momentum direction at the interaction point (neutral line). The longitudinal segmentation of

¹In this thesis, Z means always Z/γ^* .

the LAr calorimeter can be exploited to reduce the background. A special clustering algorithm is employed in this analysis for the photon reconstruction because of its high efficiency in identifying low-energy EM deposition patterns in the LAr calorimeter. An advantage of this analysis is the ability to verify the signal purity by comparing the improvement of the $Z \rightarrow \mu\mu$ invariant mass resolution with the expectation from Monte Carlo (MC). The correction for QED FSR contributions leads to a significant improvement on the Z-boson invariant mass resolution and scale.

The method is generally available in identifying low-energy deposition patterns in the EM calorimeter. One important application is to validate the pile-up reweighting performance by checking the EM energy deposition around the Z-decay μ , which is based on the method of FSR reconstruction and the special clustering algorithm.

Furthermore, in the Standard Model Higgs boson search, the decay channel $\text{Higgs} \rightarrow ZZ(*) \rightarrow 4l (l = e, \mu)$ provides the cleanest experimental signature for the Higgs boson discovery, in the Higgs mass range between 130 GeV and 600 GeV [3]. However, in the high mass region large tails have been observed in the 4-lepton invariant mass. One of the most important contribution to these tails is the omission of FSR photons. The inner bremsstrahlung contribution is potentially larger in the electron channel, but the overall effect is in fact somewhat less than for the muon channel, since the nearby photons are automatically included in the electron cluster in most cases [4][5]. Currently in the Higgs mass reconstruction, only four leptons are considered as the final state of $\text{Higgs} \rightarrow ZZ(*) \rightarrow 4l$. The QED FSR photons from the Z leptonic decay can lead to a non-negligible FSR-induced distortion on the Higgs invariant mass. Also, in the high Higgs mass region, the outgoing radiated photon can carry an even larger energy since the Z's can be boosted. By reconstructing and adding back the FSR photons to the invariant mass of Higgs, the mass resolution and scale of the Higgs boson can be significantly improved.

In this thesis, Chapter 2 reviews the Standard Model. Chapter 3 introduces the Drell-Yan process. Chapter 4 presents an overview of the ATLAS detector and the ATLAS software. Chapter 5 discusses the event reconstruction in ATLAS, including the muon reconstruction and the electromagnetic cluster reconstruction. Chapter 6 presents the reconstruction performance studies of the $Z \rightarrow \mu\mu\gamma$ decay, by using the LAr calorimeter and a special clustering with the ATLAS detector in LHC proton-proton collisions at $\sqrt{s} = 7$ TeV. A measurement of the cross-section for $Z \rightarrow \mu\mu\gamma$ events with at least one FSR photon within fiducial region ($E_{T,\gamma} > 1.3$ GeV and $\Delta R_{\gamma,\mu} < 0.15$) is also presented in this chapter. Chapter 7 applies the FSR method to the $\text{Higgs} \rightarrow ZZ(*) \rightarrow 4\text{lepton}$ channel. The contribution of the FSR photons leads to a dramatic improvement in the energy resolution and scale of the Higgs mass, which is crucial to the Higgs search. Tables for various Monte Carlo generators are provided

in Appendix A. A dedicated tool to obtain FSR photons around a given muon is introduced in Appendix B.

Chapter 2

The Standard Model

2.1 Particles and Interactions

The Standard Model of elementary particle physics comprises the unified theory of the electroweak interaction and quantum chromodynamics. It is a quantum field theory based on the gauge symmetry $SU(3)_C \times SU(2)_L \times U(1)_Y$.

Present evidence indicates that matter is built from two types of fundamental fermions with half-integer spin, called quarks and leptons, which are structureless and pointlike [6]. They are grouped, according to their masses, into three “families”, or “generations”. From the measured width of the Z resonance, one can deduce that no further (fourth) massless neutrino exists. Thus, the existence of a fourth generation of fermions (at least one with a massless neutrino) can be excluded [7]. Table 2.1 presents an overview of all fermions in the Standard Model [8]. Each fermion has an associated antifermion. It has the same mass as the fermion, but opposite electric charge, colour and third component of weak isospin.

- Quarks carry fractional electric charges, of $+\frac{2}{3}|e|$ and $-\frac{1}{3}|e|$. They occur in six flavours, distinguished by the assignment of internal quantum numbers, and are labelled u, d, s, c, b, t . The u - and d - quarks are the lightest and have approximately the same mass (within 1 MeV or so). They are grouped as an isospin doublet ($I = \frac{1}{2}$, with the third component $I_3 = +\frac{1}{2}$ for u and $I_3 = -\frac{1}{2}$ for d). The s - quark is assigned an internal quantum number called strangeness, with value $S = -1$, the c -quark a charm quantum number $C = +1$, the b -quark a bottom quantum number $B = -1$, and the t -quark a

Leptons		Quarks	
Flavor	Elec. charge	Flavor	Elec. charge
ν_e	0	u	$\frac{2}{3}$
e^-	-1	d	$-\frac{1}{3}$
ν_μ	0	c	$\frac{2}{3}$
μ^-	-1	s	$-\frac{1}{3}$
ν_τ	0	t	$\frac{2}{3}$
τ^-	-1	b	$-\frac{1}{3}$

Table 2.1: Fermions of the Standard Model (taken from Ref. [6]).

top quantum number $T = +1$. Correspondingly, each antiquark is assigned an opposite charge, strangeness, etc.

- The leptons carry integral electric charges, 0 or $\pm|e|$. The neutral leptons are called neutrinos, and have very small rest mass. The leptons appear in doublets, the neutrinos being assigned a subscript corresponding to the charged member. A lepton number L_e, L_μ, L_τ of +1 is given to each type of lepton and -1 to each antilepton. Neutrinos are longitudinally spin-polarized with $J_z = -\frac{1}{2}$ (“left-handed”), where z is the direction of the velocity vector, while antineutrinos have $J_z = +\frac{1}{2}$ (“right-handed”).

In quantum field theory, all the forces of nature occur as a result of the exchange of specific quanta associated with the particular type of interaction. The conservation laws can be satisfied only if the quantum carriers live for a time limited by the Uncertainty Principle ($\Delta t \leq (\hbar/\Delta E)$), that is, they are “virtual” particles. The intermediate particles or force carriers, are gauge bosons with integer spin of $s = 1$. Their interaction with particles is a direct consequence of gauge symmetries. Table 2.2 lists the gauge bosons with their associated interactions [8].

Interaction	Charge	Exchange particle(s)	Mass(GeV)	Range
strong	colour	8 gluons(g)	0	$1 fm$
electromagnetic	electric charge	photon(γ)	0	∞
weak	weak charge	W^\pm, Z	$\approx 10^2$	$10^{-3} fm$

Table 2.2: Gauge interactions in Standard Model (taken from Ref. [6]).

The photon, γ , is the exchange particle in electromagnetic interactions. The range of the electromagnetic interaction is infinite since photons are massless. Pho-

tons couple to charged particles with a coupling constant of $\alpha = \frac{e^2}{4\pi}$ where e is the electromagnetic charge. At low energies, in the Thomson limit, α has the value of the fine structure constant $\approx \frac{1}{137}$. The field theory employed to compute the cross-sections for such electromagnetic processes is called quantum electrodynamics (QED).

The weak bosons, W^\pm and Z , mediate the weak force. The weak interactions take place between all quark and lepton constituents, changing quark and lepton “flavour”. This interaction is so feeble however that it is usually swamped by the much stronger electromagnetic and strong interactions, unless these are forbidden by conservation rules. The observable weak interactions therefore either involve neutrinos (which have no electric or strong charges) or quarks with a flavor change (forbidden for strong or electromagnetic interactions). Because of the large mass of the exchange bosons of the weak interaction, its range is limited to $10^{-3} fm$. The coupling constant of the weak bosons is $\alpha_W = \frac{g_W^2}{4\pi}$ which, at energies much lower than the mass of its intermediate particles, is $\approx \frac{1}{30}$. The electromagnetic interaction and the weak interaction can be interpreted as two aspects of a single interaction: the electroweak interaction. The corresponding charges are related by the Weinberg angle [7].

The gluons, g , carry the strong force and couple to the colour charge. Quarks are the only fermions which carry colour charge, and are therefore the only fermions interacting via the strong force. Gluons themselves also carry colour and therefore interact with each other. This effect leads to the principle of confinement. Gluons have zero rest mass. The effective range of the strong interaction is limited by the mutual interaction of the gluons. The energy of the colour field increases with increasing distance. At distances $\geq 1 fm$, it is sufficiently large to produce real quark-antiquark pairs. “Free” particles always have to be colour neutral. At low energies at about the mass of light hadrons the strong force has a large coupling constant given by $\alpha_S = \frac{g_S^2}{4\pi} \approx 1$ but a nearly vanishing value at large energies. The theory of the strong interaction is described by quantum chromodynamics (QCD) [1].

Different conservation laws correspond to the different interactions [7]:

- The following physical quantities are conserved in all three interactions: energy (E), momentum (p), angular momentum (L), charge (Q), colour, baryon number (B) and the three lepton numbers (L_e, L_μ, L_τ).
- The P and C parities are conserved in the strong and in the electromagnetic interaction; but not in the weak interaction. Parity violation is maximal in the charged current of the weak interaction. The charged current only couples to

left-handed fermions and right-handed antifermions. For the neutral current of the weak interaction, it is partly parity violating. It couples to left-handed and right-handed fermions and antifermions, but with different strengths. The well-known case is that the combined CP parity is not conserved.

- Quarks and leptons have their flavour transformed only in the charged currents of the weak interaction. Therefore, the quantum numbers determining the quark flavour (third component of isospin (I_3), strangeness (S), charm (C) etc.) are conserved in all other interactions.
- The magnitude of the isospin (I) is conserved in strong interactions.

In summary, experiments are in astoundingly good quantitative agreement with the assumptions of the standard model.

2.2 The Electroweak Theory

The unification of the electromagnetic and weak force was accomplished by GSW (S.L.Glashow [9], A.Salam [10] and S.Weinberg [11]). An important step for this procedure was that the weak neutral and charged currents taken together form the symmetry group $SU(2)_L \times U(1)_Y$. The subscript L indicates that the weak isospin current only couples to left-handed fermions and right-handed antifermions. It originates from the “vector minus axial” (V-A) nature of the charged currents [6]. A weak isospin singlet, was called weak hypercharge current. The hypercharge Y is defined by the Gell-Mann-Nishijima-Formula. Thus the symmetry group $SU(2)_L \times U(1)_Y$ contains the electromagnetic and weak interaction. The GSW-theory is very successful, as it relates the masses of the weak gauge bosons to the gauge couplings. Invariance under gauge transformations of the Lagrangian which describes particle states is considered a basic principle to describe also their interactions. A Lagrangian is a function that summarizes the dynamics of the system. Gauge transformations, also known as local transformations, are the ones under which parameters are space-time dependent. A Lagrangian density, \mathcal{L} , itself cannot be derived from underlying principles, but has to be found and validated using the basic principle of physics and nature: the principle of least action. It states, that the action S during transition of a physical system between two states has to be minimal. In case of quantum field

theories S is a functional of the Lagrangian density \mathcal{L} :

$$S = \int_{state_1}^{state_2} d^4x \mathcal{L}(\partial_\mu \psi(x), \partial_\mu \bar{\psi}(x), \psi(x), \bar{\psi}(x)), \quad (2.1)$$

With the Lagrangian of a relativistic massive fermion and the Euler-Lagrange formalism, the Dirac equation can be derived. It describes the propagation of a fermion through spacetime.

$$\mathcal{L} = \bar{\psi}(x)(i\partial_\mu \gamma^\mu - m)\psi(x), \quad (2.2)$$

$$\frac{\partial \mathcal{L}}{\partial \bar{\psi}(x)} - \partial_\mu \frac{\partial \mathcal{L}}{\partial (\partial_\mu \bar{\psi}(x))} = 0, \quad (2.3)$$

$$(i\partial_\mu \gamma^\mu - m)\psi(x) = 0, \quad (2.4)$$

where $\psi(x)$ is a Dirac spinor field. It has to be noted, that the field itself is not an observable, but only $|\psi(x)|^2$. Applying a global phase α at all spacetime points x , the gauge transformation on $\psi(x) \rightarrow e^{i\alpha}\psi(x)$ does not change the associated Lagrangian \mathcal{L} . However when using a gauge transformation, with $\alpha(x)$ varying at each point of spacetime $\psi(x) \rightarrow e^{i\alpha}\psi(x)$ does change the Lagrangian \mathcal{L} , and breaks gauge invariance. To make the Lagrangian invariant under gauge transformations a method called minimal coupling is applied. The derivative ∂_μ is replaced by the so called covariant derivative D_μ . This introduces a new field, in this case a vector field, $A_\mu(x)$:

$$\partial_\mu \rightarrow D_\mu = \partial_\mu - ieA_\mu(x). \quad (2.5)$$

The modified Lagrangian \mathcal{L}' is invariant under the gauge transformation, as terms of the covariant derivative, compensate the troublesome terms. The $A_\mu(x)$ field is interpreted as the field of the photon, γ . It must be massless because mass term, $\frac{1}{2}M_\gamma^2 A_\mu(x)A^\mu(x)$, would destroy the just restored local gauge symmetry. The QED Lagrangian for fermions and massless photons is thus given by:

$$\mathcal{L}_{QED} = \bar{\psi}(x)(i\partial_\mu \gamma^\mu - m)\psi(x) - \frac{1}{4}F_{\mu\nu}(x)F^{\mu\nu}(x) + eQ\bar{\psi}(x)\gamma^\mu A^\mu(x)\psi(x), \quad (2.6)$$

with $F_{\mu\nu}$ the ‘‘field strength tensor’’ defined as [12]

$$F_{\mu\nu}(x) = \partial_\mu A_\nu(x) - \partial_\nu A_\mu(x). \quad (2.7)$$

Fermion masses are added by hand to the Lagrangian \mathcal{L}_{QED} . The electroweak Lagrangian \mathcal{L}_{EW} must be extended by the gauge fields \vec{W}_μ and B_μ of the $SU(2)_L \times U(1)_Y$ group. It is rather troublesome that the requirement for local gauge invariance of \mathcal{L}_{EW} does also not allow any mass terms, neither for the \vec{W}_μ -field and B_μ -field nor the fermions, as the weak interaction couples differently to left and right chiral particles.

$$\mathcal{L}_{EW} = \bar{\chi}_L \gamma^\mu D_\mu \chi_L + \bar{\nu}_R \gamma^\mu D_\mu \nu_R + \bar{e}_R \gamma^\mu D_\mu e_R - \frac{1}{4} \vec{W}_{\mu\nu} \vec{W}^{\mu\nu} - \frac{1}{4} B_{\mu\nu} B^{\mu\nu}, \quad (2.8)$$

where

$$D_\mu = i\partial_\mu - g\frac{1}{2}\vec{\tau}\vec{W}_\mu - g'\frac{Y}{2}B_\mu, \quad (2.9)$$

$$\chi_L = \begin{pmatrix} e \\ \nu \end{pmatrix}_L \quad (2.10)$$

and

$$\vec{W}_{\mu\nu} = \partial_\mu \vec{W}_\nu - \partial_\nu \vec{W}_\mu - g\vec{W}_\mu \times \vec{W}_\nu, \quad (2.11)$$

$$B_{\mu\nu}(x) = \partial_\mu B_\nu - \partial_\nu B_\mu. \quad (2.12)$$

These gauge fields cannot be directly associated with a physical field or particle. The physical neutral current fields, A_μ and Z_μ , identified with the gauge bosons γ and Z^0 , are linear combinations of the third component of the \vec{W}_μ -field and the B_μ -field. This mixing of fields is given by the weak mixing angle θ_W :

$$\begin{pmatrix} A_\mu \\ Z_\mu \end{pmatrix} = \begin{pmatrix} \cos \theta_W & \sin \theta_W \\ -\sin \theta_W & \cos \theta_W \end{pmatrix} \cdot \begin{pmatrix} B_\mu \\ W_\mu^3 \end{pmatrix} \quad (2.13)$$

The weak mixing angle θ_W has an experimentally determined value of $\sin^2(\theta_W) \approx 0.23$. The physical W^\pm bosons are a linear combination of the remaining first and second component of the W_μ -field:

$$W^\pm = \frac{1}{\sqrt{2}}(W_\mu^1 \mp W_\mu^2). \quad (2.14)$$

The masses for the gauge bosons Z^0 and W^\pm , as well for fermions, should be zero according to the GSM-theory, in contradiction to experimental evidence. Therefore, a mechanism to reconcile theory and experiment had to be introduced.

2.3 The Higgs Mechanism

As described in Section 2.2 the requirement of gauge invariance forbids to have mass terms for gauge bosons and fermions in the Lagrange density although they indeed are massive. This issue is solved by the idea of Spontaneous Symmetry Breaking [13]. A good example can be given by looking at a point mass in a potential:

$$V(\vec{\varphi}) = \mu^2 \vec{\varphi} \cdot \vec{\varphi} + \lambda (\vec{\varphi} \cdot \vec{\varphi})^2, \quad (2.15)$$

which is symmetric under rotations and λ is assumed to be above zero (otherwise there would be no stable ground state). For $\mu^2 > 0$ the potential has a minimum at $\vec{\varphi} = 0$, thus the point mass will simply fall to this point. The situation is more interesting if $\mu^2 < 0$. For two dimensions the potential is shown in Figure 2.1. If the point mass sits at $\vec{\varphi} = 0$ the system is not in the ground state but the situation is completely symmetric. In order to reach the ground state, the symmetry has to be broken. This is exactly what spontaneous symmetry breaking means. The Lagrangian (here the potential) is symmetric (here under rotations around the z -axis) but the ground state (here the position of the point mass once it rolled down) is not.

In the Standard Model, it will be a non-Abelian gauge theory that is spontaneously broken. The Higgs doublet Lagrangian containing a “spontaneous symmetry breaking” potential is introduced:

$$\mathcal{L}_{Higgs} = (D_\mu \Phi)^\dagger (D^\mu \Phi) - V(\Phi), \quad (2.16)$$

with

$$V(\Phi) = \mu^2 \Phi^\dagger \cdot \Phi + \lambda (\Phi^\dagger \cdot \Phi)^2, \quad (2.17)$$

where D_μ is the same as in \mathcal{L}_{EW} . The Higgs potential, $V(\Phi)$, is relevant for mass generation when $\mu^2 < 0$ and $\lambda > 0$. Only then it acquires a minimum at $\langle \Phi^\dagger \cdot \Phi \rangle = -\frac{\mu^2}{2\lambda}$. The ground state can be chosen as

$$\Phi_0 = \frac{1}{\sqrt{2}} \begin{pmatrix} 0 \\ v \end{pmatrix}, \quad (2.18)$$

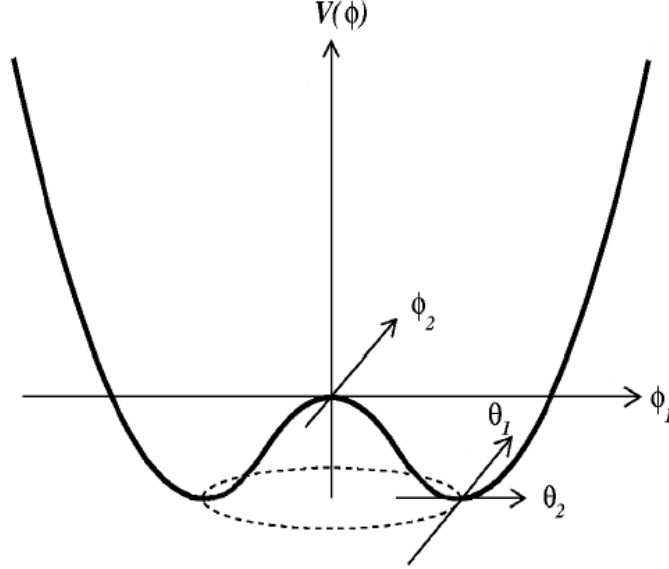


Figure 2.1: A potential that leads to spontaneous symmetry breaking.

resulting in a vacuum expectation value of v ($v^2 = -\frac{\mu^2}{\lambda}$). Expanding $\Phi(x)$ around the chosen minimum, Φ_0 , yields:

$$\Phi(x) = \frac{1}{\sqrt{2}} \begin{pmatrix} 0 \\ v + h(x) \end{pmatrix}. \quad (2.19)$$

The field $h(x)$ is the field of the Higgs boson. Interactions of particles with the Higgs field generate their masses. Substituting $\Phi(x)$ into the Lagrange density \mathcal{L}_{Higgs} and comparison with mass terms of the form $m^2 B_\mu B^\mu$ for bosons and of $m_f \bar{f} f$ for fermions leads to the following masses [6]:

$$m_{W^\pm} = \frac{vg}{2}, \quad (2.20)$$

$$m_Z = \frac{v}{2} \sqrt{g^2 + g'^2}, \quad (2.21)$$

$$m_H = v\sqrt{2\lambda}, \quad (2.22)$$

$$m_f = v \frac{\lambda_f}{\sqrt{2}}. \quad (2.23)$$

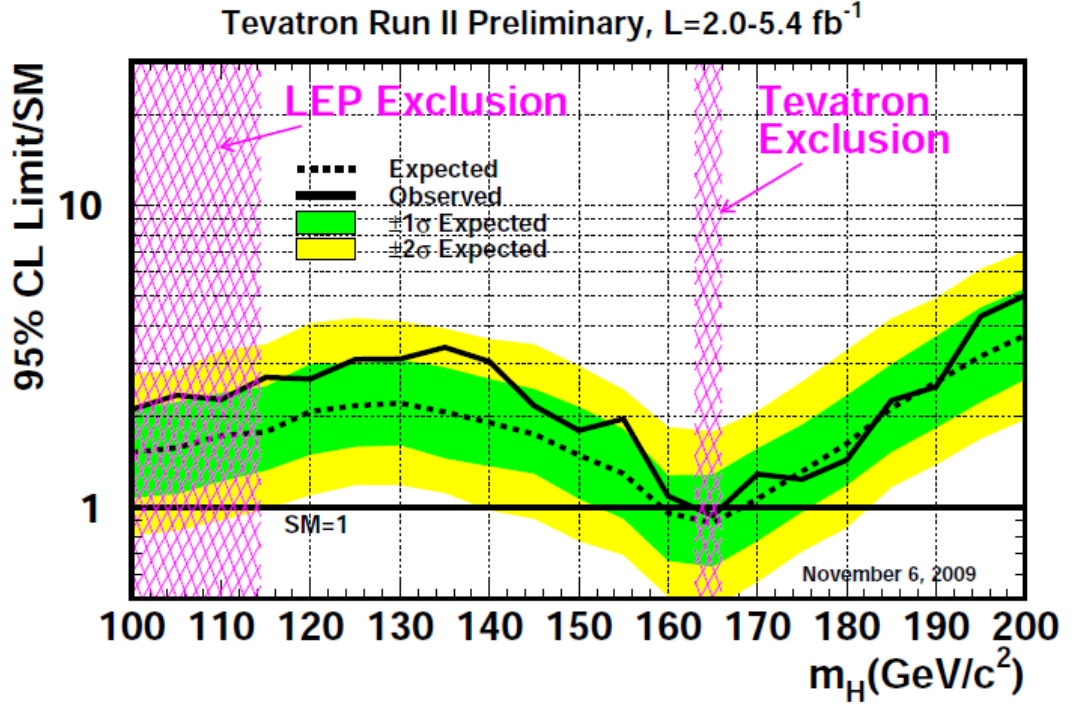


Figure 2.2: Exclusion regions for the mass of the Higgs, updated with results from the Tevatron (taken from Ref. [14]).

The Higgs boson is the last undiscovered particle of the Standard Model. The Higgs mass is a free parameter in the Standard Model. Theoretical upper bounds of its mass are given at around 1 TeV, where the scattering of longitudinally polarized W^\pm bosons would violate unitarity without another particle appearing in the interaction [15]. Direct searches at the CERN LEP e^+e^- collider excluded the production of a SM Higgs boson with mass below 114.4 GeV at the 95% confidence level (C.L.) [16][17]. The combined searches at the Fermilab Tevatron $p\bar{p}$ collider have excluded the production of a Higgs boson with mass between 156 GeV and 177 GeV at the 95% CL [14]. The observed and expected limits are shown in Figure 2.2. In 2011, a dataset of up to 4.9 fb^{-1} recorded has been used to search for the SM Higgs boson with the ATLAS experiment at the LHC. The experimental limits from ATLAS on SM Higgs production are shown in Figure 2.3. Higgs boson masses between 124 GeV

and 519 GeV are expected to be excluded at the 95% CL. The observed exclusion at the 95% CL ranges from 112.9 GeV to 115.5 GeV, 131 GeV to 238 GeV and 251 GeV to 466 GeV [18].

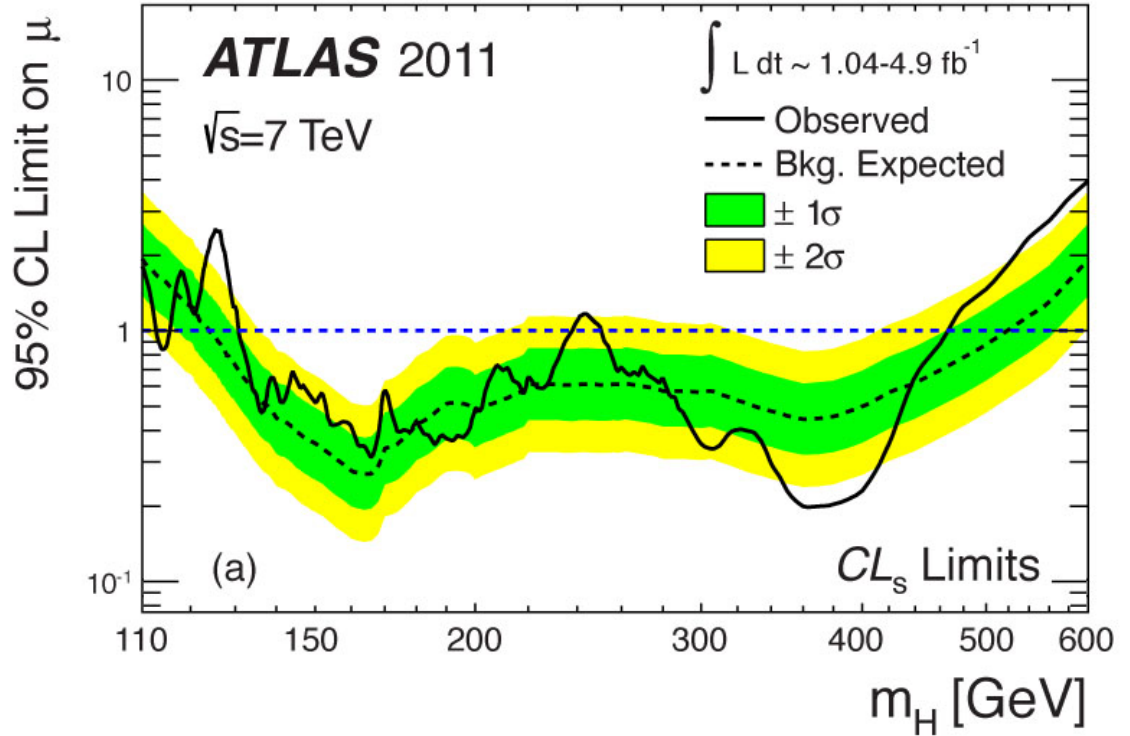


Figure 2.3: Experimental limits from ATLAS on Standard Model (SM) Higgs production in the mass range 110-600 GeV. The solid curve reflects the observed experimental limits, expressed in terms of the ratio (μ) of the observed cross-section to the cross-section predicted by the SM (vertical axis), for the production of Higgs for each possible mass value (horizontal axis). The region for which the solid curve dips below the horizontal line at the value of 1 is excluded with a 95% confidence level (CL). The dashed curve shows the expected limit in the absence of the Higgs boson, based on simulations. The green and yellow bands correspond (respectively) to 68%, and 95% confidence level regions from the expected limits (taken from Ref. [18]).

Chapter 3

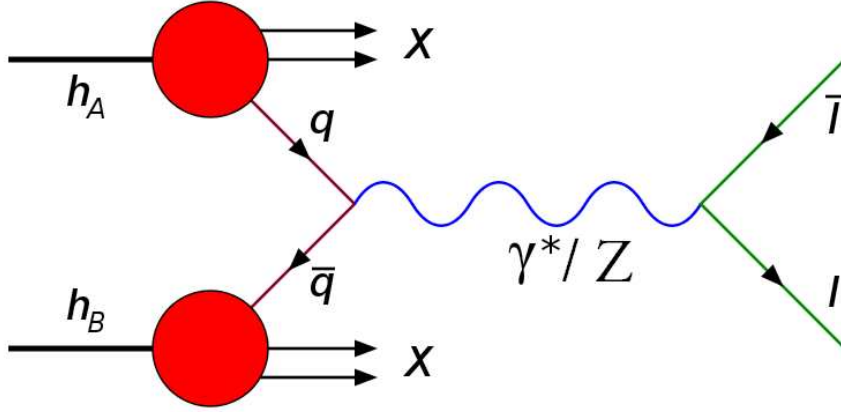
The Drell-Yan Process

Drell-Yan production [19] (Figure 3.1) of lepton pairs through electroweak (EW) gauge bosons at hadron colliders occupies a special place in elementary particle physics. Historically, the Drell-Yan mechanism was the first application of parton model ideas beyond deep inelastic scattering, and was later the route to the discovery of the W and Z bosons. Currently, it provides a standard candle for hadronic high-energy colliders such as the LHC, and offers an important testing ground for Quantum Chromodynamics (QCD) [1]. An overview of cross-sections of some benchmark processes at Tevatron and the LHC as a function of the centre-of-mass energy is shown in Figure 3.2 [20]. At LHC energies, the electroweak W and Z bosons will be produced in millions but their production rate will be swamped by that from QCD events.

3.1 The leading order Drell-Yan model

3.1.1 Parton Distribution Functions

The calculation of the production cross sections at hadron colliders for both interesting physics processes and their backgrounds relies upon a knowledge of the distribution of the momentum fraction of partons (quarks and gluons) in the proton in the relevant kinematic range. The Parton Distribution Functions (PDF) give the probability of finding a quark q_i of type i or a gluon g carrying a momentum fraction x (the Bjorken x) of the hadron, when it is probed with four-momentum-transfer-squared

Figure 3.1: Illustration of Drell-Yan process in case of γ^*/Z .

Q^2 [1]. PDFs are non-perturbative objects, thus they cannot be predicted by perturbative QCD. Their functional form as a function of Bjorken x , $f(x)$, for a particular squared momentum transfer $Q^2 \gg 1 \text{ GeV}^2$ is normally given by a parametrization. The parameters entering the functional form are determined from data (typically differential cross sections) obtained for bins of x and Q^2 . Given a measurement (e.g. deep-inelastic scattering data) of the PDF distributions $f(x)$ at one particular value of $Q^2 \gg 1 \text{ GeV}^2$, they can be extrapolated using perturbative QCD to any other Q^2 , provided that Q^2 is large enough so that non-perturbative physics has no impact. The standard procedure is to choose some input PDF parametrisation, normally at low Q^2 , and evolve it to larger Q^2 s applying the DGLAP QCD evolution equations which involve the branching processes $q \rightarrow qg$, $g \rightarrow gg$, $g \rightarrow q\bar{q}$ [21]. The predictions of measured quantities (e.g. structure functions) are obtained and then fitted to the measured datasets, thus constraining the parameters of the parametrisation. There are also constraints from sum rules, e.g. since a proton has two u_v and one d_v valence quarks, it must have:

$$\int_0^1 u_v(x) dx = 2 \quad (3.1)$$

and

$$\int_0^1 d_v(x) dx = 1. \quad (3.2)$$

There is also a momentum sum rule, integrating over all parton types:

$$\int_0^1 [xq(x) + x\bar{q}(x) + xg(x)]dx = 1. \quad (3.3)$$

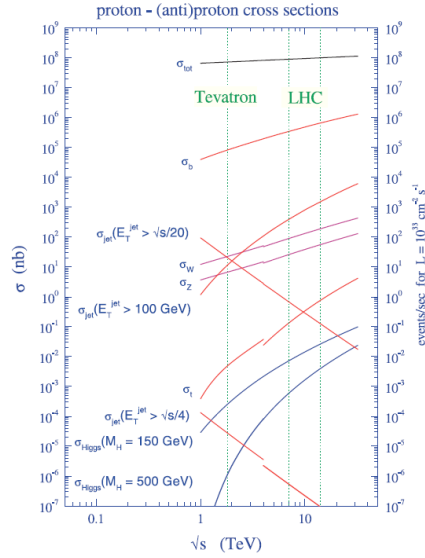


Figure 3.2: Standard Model cross-sections at the Tevatron and the LHC as function of the centre-of-mass energy (taken from Ref. [20]).

Fits to the available data leading to updates of the PDF sets have been performed and determined by various of groups. For example, to NLO QCD by the CTEQ [22][23] group, and to NNLO by the MSTW [24], ABKM [25], JR [26], HERAPDF [27][28] and NNPDF [29][30] groups. The CTEQ group extracts new parton distribution functions of proton by global analysis of hard scattering data using a general mass heavy flavour scheme. One example of CT10 PDF sets evaluated at $\mu(Q)=2$ GeV scale by the CTEQ group, is shown in Figure 3.3.

In the cross-section measurement, the uncertainties arising from PDFs are normally estimated using PDF eigenvector error sets following the calculation of a symmetric/asymmetric prescription (details can be found in Ref. [31]).

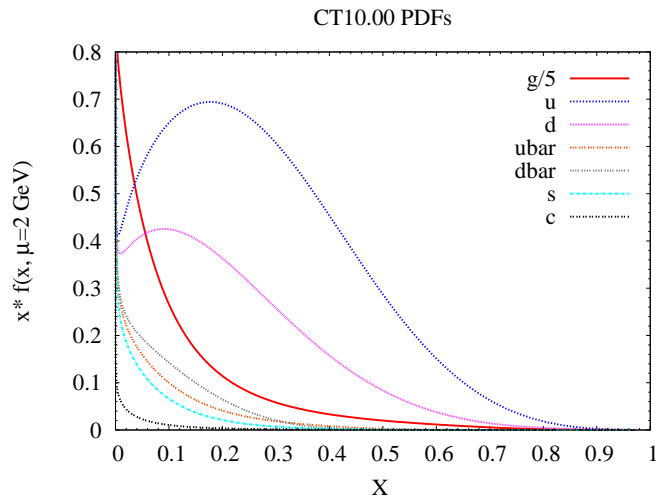


Figure 3.3: Parton distribution functions as determined for the CT10 PDF set evaluated at $\mu(Q)=2$ GeV (taken from Ref. [23]).

3.1.2 The dynamics of the Drell-Yan process

Drell and Yan (1970) proposed a simple process to account for the production of dilepton pairs in high energy hadron-hadron collisions [32][19]:

$$\text{hadron} + \text{hadron} \rightarrow l^+l^- + \text{anything}. \quad (3.4)$$

It is essential in this process that, a single antiquark from one hadron annihilates on a single quark from the other hadron to produce a virtual photon or Z boson, which then decays into a pair of oppositely-charged leptons. If the mass M of the dilepton is large compared to the nucleon mass, then the Heisenberg uncertainty principle tells us that the time of interaction is short on the nuclear scale. Thus there is no opportunity for the annihilating quark-antiquark pair to interact with other components of the parent hadrons. The other partons can be treated purely as spectators. Subsequently, on a time scale that is long compared to the annihilation, the spectators rearrange themselves into outgoing hadrons.

The dilepton kinematic variables τ and x_F are directly related to the Bjorken x values of the parent quark and antiquark. Suppose the active quark/antiquark in the beam particles has a Bjorken x of x_1/x_2 , which can be described by the following equations:

$$x_1 = \sqrt{\tau}e^y, x_2 = \sqrt{\tau}e^{-y}, \quad (3.5)$$

$$\tau = \frac{M^2}{s} = x_1 x_2, \quad (3.6)$$

$$x_F = x_1 - x_2. \quad (3.7)$$

The $s = 4E_p^2$ is the centre-of-momentum system (cms) energy squared. The rapidity y is another important variable, the original definition of which is:

$$y = \tanh^{-1}\beta \quad (3.8)$$

In relativity, rapidity y [1] is an alternative to the particle's velocity component along the beam axis, but transformed in such a way that while for a small values it is identical to the usual speed $\beta c = v$, at large values it does not "saturate" but keeps going (as $\beta \rightarrow 1.000$, $y \rightarrow \infty$). Unlike speeds at relativistic velocity, the values of rapidity are simply additive. Rapidity follows the law of addition of speeds: $y_{13} = y_{12} + y_{23}$. The difference in the rapidity of two particles is independent of Lorentz boosts along the beam axis. Although in general the three-dimensional rapidity can be used, in a hadron collider one axis has special significance. In hadron-hadron collisions, the beam-beam axis z is chosen as the axis to define a one-dimensional (longitudinal) rapidity, and measure transverse momenta p_T , and transverse energies E_T , with respect to this axis.

In elementary relativity, the law for addition of speeds is:

$$\beta_{13} = \frac{\beta_{12} + \beta_{23}}{1 + \beta_{12}\beta_{23}}, \quad (3.9)$$

which is identical to the formular when applying hyperbolic tangent function:

$$\tanh(A + B) = \frac{\tanh(A) + \tanh(B)}{1 + \tanh(A)\tanh(B)}. \quad (3.10)$$

so if:

$$\beta \equiv \tanh(y), \quad (3.11)$$

i.e.,

$$y = \tanh^{-1}\beta, \quad (3.12)$$

The solution is then:

$$y = \frac{1}{2} \ln \frac{1 + \beta}{1 - \beta}, \quad (3.13)$$

as $\beta = p/E$, the above can be rewritten:

$$y = \frac{1}{2} \ln \frac{E+p}{E-p}. \quad (3.14)$$

When the mass of the particle is small compared to p_T , the pseudorapidity η [1] is frequently used as a good approximation to y , defined as:

$$\eta = -\ln(\tan \frac{\theta}{2}), \quad (3.15)$$

where θ is the polar angle between the particle momentum p and the beam axis.

3.1.3 Cross-section formalism

The leading order process of the Drell-Yan model of lepton pair production for the neutral current reaction $pp \rightarrow (Z/\gamma)X \rightarrow l^+l^-X$, shown in Figure 3.1. The cross section consists of three terms: the pure photon exchange, the pure Z exchange and the interference term [33]. In the case of photon exchange, the annihilation of point fermions resembles the electron-positron annihilation to dileptons. Quantum electrodynamics yields the cross section [32]:

$$\sigma = 4\pi\alpha^2 e_q^2 / 3Q^2 \quad (3.16)$$

where α is the fine structure constant, e_q is the quark charge and Q^2 is the four momentum of the virtual photon. The factor Q^{-2} comes from the photon propagator term in the amplitude. Here Q^2 is just the dilepton mass squared M^2 . Therefore

$$\sigma = 4\pi\alpha^2 e_q^2 / 3M^2. \quad (3.17)$$

This expression has to be multiplied by the probability $q(x_1)dx_1$ that a quark in the beam carries a momentum fraction x_1 , and the probability $\bar{q}(x_2)dx_2$ that an antiquark in the beam carries a momentum fraction x_2 . Each quark flavour can contribute, so all flavors are summed over. Also, the quark and antiquark colour must match, which reduces the cross section by a factor of 3. All these ingredients are put together, leading to the differential cross section:

$$\frac{d^2\sigma}{dx_1 dx_2} = \frac{4\pi\alpha^2}{9M^2} \sum e_q^2 [q(x_1)\bar{q}(x_2) + \bar{q}(x_1)q(x_2)]. \quad (3.18)$$

Re-expressing this in terms of rapidity, the cross section for the pure photon exchange part is:

$$\frac{d^2\sigma}{dMdy} = \frac{8\pi\alpha^2}{9} \frac{1}{M^3} \sum e_q^2 x_1 x_2 [q(x_1)\bar{q}(x_2) + \bar{q}(x_1)q(x_2)]. \quad (3.19)$$

A general cross section formula, representing the contribution from photon and Z exchange as well as their interference, can be written as [33]:

$$\frac{d^2\sigma}{dMdy} = \frac{8\pi\alpha^2(M)}{9} MP(M)\Phi(x_1, x_2). \quad (3.20)$$

The propagator term P and the parton distribution term Φ are given for the pure photon part, the interference part and the pure Z part, respectively:

$$P_\gamma = \frac{1}{M^4}, \Phi_\gamma = \sum_q e_q^2 F_{q\bar{q}}, \quad (3.21)$$

$$P_{\gamma Z} = \frac{\nu_l(M^2 - M_Z^2)}{(4\sin^2\Theta\cos^2\Theta)M^2[(M^2 - M_Z^2)^2 + (\Gamma_Z M_Z)^2]}, \Phi_{\gamma Z} = \sum_q 2e_q\nu_q F_{q\bar{q}}, \quad (3.22)$$

$$P_Z = \frac{(\nu_l^2 + a_l^2)}{(4\sin^2\Theta\cos^2\Theta)^2[(M^2 - M_Z^2)^2 + (\Gamma_Z M_Z)^2]}, \Phi_Z = \sum_q (\nu_q^2 + a_q^2) F_{q\bar{q}}. \quad (3.23)$$

where

$$F_{q\bar{q}} = x_1 x_2 [q(x_1)\bar{q}(x_2) + \bar{q}(x_1)q(x_2)], \quad (3.24)$$

the polar-vector and axial-vector couplings are

$$\nu_f = I_3^f - e_f \sin^2\Theta, a_f = I_3^f [f = l, q], \cos\Theta = \frac{M_W}{M_Z}. \quad (3.25)$$

The leading order neutral current (NC) Drell-Yan cross section is shown in Figure 3.4 [33]. The top plot shows the cross section as a function of the mass of the e^+e^- pair integrated over the boson rapidity y . In the small M region the pure photon contribution determines the cross section. Around $M = 70$ GeV the photon

and Z contributions are equal. The resonance region is dominated by the Z part. At large M, the photon and Z unify. The relative fraction of the interference cross section to the total Born cross section is shown in the bottom plot. The interference contribution changes sign from positive to negative as the mass increases and passed M_Z .

3.2 High order QCD corrections

The above *naive* Drell-Yan model fails to predict real measurements because it neglects higher order QCD effects such as QCD radiation and parton-parton interactions. The emission of a hard gluon by a quark provides the immediate mechanism by which a quark can obtain a transverse momentum kick. Also, virtual gluons may be exchanged. All possible processes at all orders have to be considered into the calculation. However, it is not possible to perform a calculation of the Drell-Yan cross section at all orders of perturbation theory. Only an approximate prediction can be obtained by expanding the cross section in a perturbative power series in the coupling constant. Current theoretical calculations extend to next-to-leading order (NLO) and next-to-next-to leading order (NNLO) corrections in perturbative QCD.

3.2.1 Feynman diagrams

The NLO QCD correction Feynman diagrams for the Drell-Yan process are shown in Figure 3.5. Figure 3.5(a) is a vertex correction diagram, Figures 3.5(b) and (c) involve gluon emission, together called annihilation diagrams. Figures 3.5(d) and (e) show a quark from one hadron scattering off a gluon from the other hadron, known as Compton diagrams. The amplitudes for the annihilation and Compton diagrams are copies of the QED amplitudes with colour factors added. The annihilation diagrams (b) and (c) are infrared divergent and must be considered together with the virtual gluon diagram (a). This is similar to the divergence in the cross section in QED for small photon energies (soft photons). Cross sections for physically indistinguishable states are finite, because the divergences arising from one or more soft gluons in the final state cancel with divergences from having one or more soft gluons exchanged as in diagram (a). Moreover, the annihilation and Compton processes both present mass singularities due to collinear gluons. A single quark with energy E can be replaced by a quark plus collinear gluon with total energy E , and the numbers of such replacements are infinite. These mass singularities can be absorbed into structure

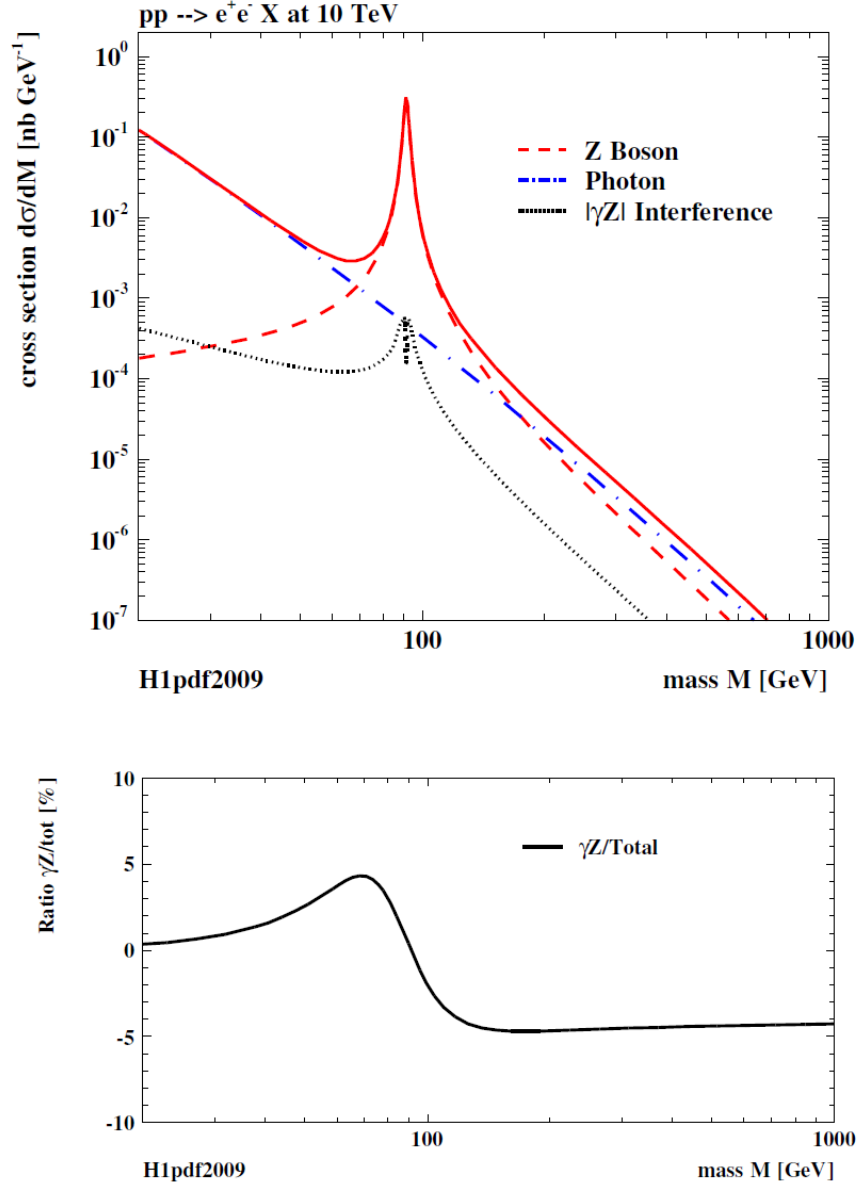


Figure 3.4: Neutral current Drell-Yan scattering cross section (top plot), as a function of the mass M of the e^+e^- pair integrated over the boson rapidity y . At small M the cross section is dominated by the pure photon contribution. The Z part determines the resonance region. The photon and Z unify at large M . The γZ interference contribution is shown in absolute value. The relative fraction of the interference cross section to the total Born cross section is shown in the bottom plot. The γZ interference changes sign at $M = M_Z$ (taken from Ref. [33]).

functions, as proposed by Politzer (1977) [34]. The idea was shown to work by Sachrajda (1978) [35] using the leading log approximation (LLA) [36][37].

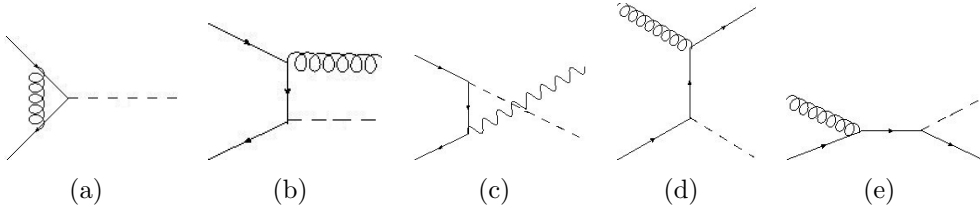


Figure 3.5: The Feynman diagram for the first-order Drell-Yan process in QCD: (a) the annihilation graph with the vertex correction; (b) and (c) are the annihilation digrams involving gluon emission in the final state; (d) and (e) are Compton diagrams (taken from Ref. [32]).

3.2.2 Theoretical calculations

The Z/γ^* and W^\pm production cross section at LHC have been estimated up to NNLO in QCD perturbative expansion. A variety of programs have implemented these calculations: e.g. up to NLO in MC@NLO [38] and MCFM [39], up to NNLO in FEWZ [40], ZWPROD [41], gg2WW [42] and gg2ZZ [43]. The FEWZ program includes leptonic decays of vector bosons with full spin correlations and finite width effects and Z/γ^* interference. It also allows selections based on final-state kinematics. The result of the $Z/\gamma^* \rightarrow ll$ and $Z \rightarrow ll$ cross sections with QCD corrections up to NNLO calculated by the FEWZ programs using the MSTW2008NNLO PDF, is listed in Table 3.1 [31]. The cross section at LO and NLO is also included. It is shown that the cross section increases by $\sim 24\%$ from LO to NLO and by $\sim 3\%$ from NLO to NNLO, suggesting that the series is converging.

The above calculations are performed using the G_μ electroweak parameter scheme and the values of the strong coupling constant α_s are taken from the PDF set used. The standard model input parameter values are summarized in Table 3.2. In the G_μ scheme, the Fermi constant G_μ and all particle masses define the basic input. The electromagnetic coupling constant and weak mixing angle are derived from the effective coupling $\alpha_{G_\mu} = \frac{\sqrt{2}G_\mu M_W^2}{\pi} (1 - \frac{M_W^2}{M_Z^2})$ and $\sin^2 \theta_W = 1 - \frac{M_W^2}{M_Z^2}$. Note that the standard model predictions for the total and partial widths of the W and Z vector bosons are required as inputs here, which also account for higher order electroweak and QCD corrections [44].

Process	M_{ll} [GeV]	QCD Order			K-factor	
		LO	NLO	NNLO	NLO/LO	NNLO/NLO
Z/γ^*	>60	778	962	989	1.24	1.029
	60-120	770	952	978	1.24	1.030
	66-116	758	938	964	1.24	1.029
	70-110	748	926	952	1.24	1.030
	80-100	710	879	904	1.24	1.029
Z	-	766	943	969	1.23	1.028

Table 3.1: $Z/\gamma^* \rightarrow ll$ and $Z \rightarrow ll$ cross sections in pb up to LO, NLO and NNLO in QCD corrections calculated from FEWZ using the MSTW2008NNLO PDF set. Note the difference between the notations Z/γ^* and Z , the former includes γ^* contribution while the latter does not (taken from Ref. [31]).

M_W	80.403 GeV	Γ_W	2.0910 GeV	$\Gamma(W \rightarrow l\nu)$	0.22629 GeV
M_Z	91.1876 GeV	Γ_Z	2.4952 GeV	$\Gamma(Z \rightarrow ll)$	0.08398 GeV
$1/\alpha_G$	132.34	$\sin^2 \theta_W$	0.22255	G_F	$1.16637 \times 10^{-5} \text{ GeV}^{-2}$
N_F	5	m_{ud}	0.32 GeV	m_s	0.50 GeV
m_c	1.29 GeV	m_b	4.2 GeV	m_t	172.5 GeV
V_{ud}	0.9738	V_{us}	0.2272	V_{ub}	0.0040
V_{cd}	0.2271	V_{cs}	0.9730	V_{cb}	0.0422
V_{td}	0.0081	V_{ts}	0.0416	V_{tb}	0.9991

Table 3.2: Input parameters used for the cross section calculations (taken from Ref. [31]).

The cross section predictions are usually dependent on the renormalisation (μ_R) and factorisation (μ_F) scales. The scale dependences are due to the missing higher order QCD corrections and can be reduced when higher order corrections are taken into account. The central value of a cross section is obtained by setting both scales to the natural energy scale of a process (e.g. $\mu_R = \mu_F = M_{W/Z}$ for the Drell-Yan production). The scale uncertainty is then estimated by varying both scales independently up-and-down around their central values, with the constraint $0.5 \leq \mu_R/\mu_F \leq 2$. The scale uncertainty is found to be $\sim \pm(2.5-3.5)\%$ at NLO and $\sim \pm 0.6\%$ at NNLO [31]. In addition to the scale uncertainty, the uncertainties arising from PDFs and the variation on α_s are also taken into account in the estimation of the cross section uncertainties.

3.3 High order electroweak corrections

3.3.1 Feynman diagrams

The DY process cross section has sizable electroweak (EW) radiative corrections [45]. The high order (HO) EW radiative corrections can be distinguished into pure weak (PW) and photonic corrections. The diagrams of weak $O(\alpha)$ corrections, e.g. the vertex and box corrections with light incoming quarks are shown in Figure 3.6. The photonic corrections consist of real and virtual corrections induced by the emission and exchange of additional photons. The virtual photonic $O(\alpha)$ corrections are composed of the one-loop photon exchange diagrams (shown in Figure 3.7(a)) and the corresponding counterterm contributions. The real photonic $O(\alpha)$ corrections consist of processes with single-photon emission $q\bar{q} \rightarrow \gamma^*/Z \rightarrow l^+l^- + \gamma$, delivering a correction to the LO process $q\bar{q} \rightarrow l^+l^-$. The diagrams are shown in Figure 3.7(b). Since only electrically neutral gauge bosons are involved in the NC Drell-Yan process, the gauge-invariant separation of the photonic and weak corrections is possible. This classification is discussed in Ref. [46]. The photonic corrections can be further classified into separately gauge-invariant subsets: initial-state radiation (ISR), final-state radiation (FSR) and initial-final state interference (INT) term.

The HO EW corrections to the DY single boson production are dominated by multiple photon emissions from the final state lepton. Photon radiation off the final-state charged lepton can considerably distort kinematic distributions, e.g. shift the invariant mass distribution of the dilepton pair. The emission of photons collinear to the outgoing charged lepton leads to corrections enhanced by mass singular logarithms of the form $\alpha \log(Q^2/m_l^2)$ with Q denoting the characteristic scale of the process. These mass singularities cancel if photons collinear to the lepton are treated fully inclusively, as guaranteed by the Kinoshita-Lee-Nauenberg (KLN) theorem [47][48][49]. However, in realistic experimental environments, a phase-space cut on the momentum applied on the outgoing lepton, can enhance the contributions of these logarithms, if, e.g. the momentum of the bare lepton is considered and no photon recombination is performed. The more inclusive treatment of the emitted photons results in a significant reduction of the final-state QED effects. Phenomenologically, the term of a bare lepton is more relevant for muon final states than electrons.

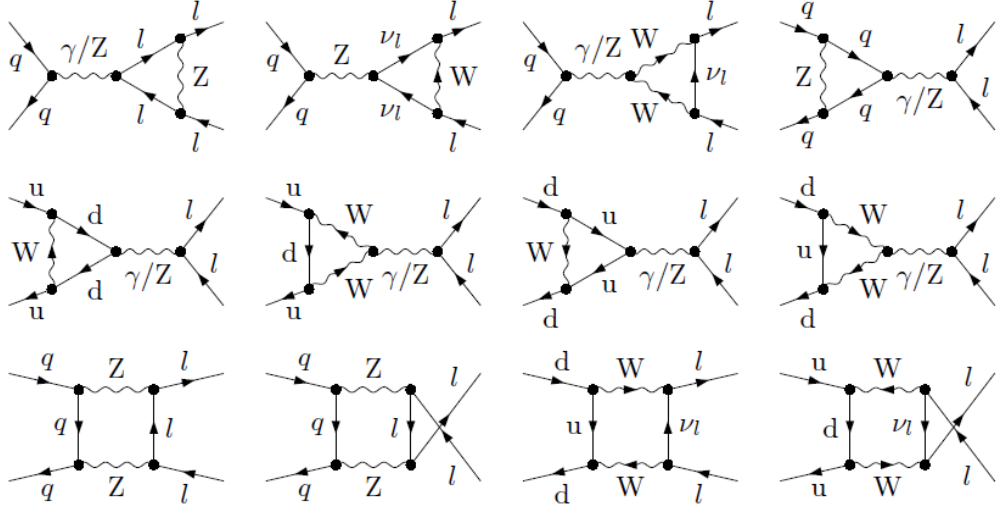
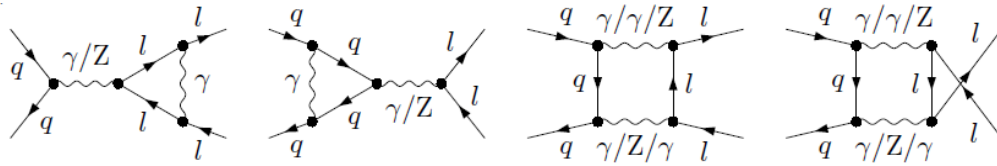
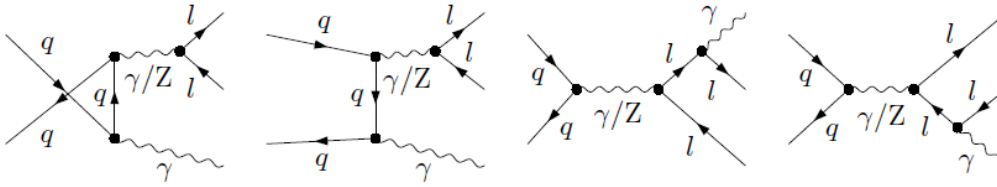


Figure 3.6: Vertex and box diagrams for weak $O(\alpha)$ corrections with light incoming quarks $q = u, d, c, s, b$ (taken from Ref. [45]).



(a) Vertex and box diagrams for photonic corrections.



(b) Diagrams for real-photon emission.

Figure 3.7: Diagrams for photonic $O(\alpha)$ corrections (taken from Ref. [45]).

3.3.2 Theoretical predictions

The electroweak radiative corrections have been studied in detail, see e.g. Ref. [50]. The reported results for the cross section of $p\bar{p} \rightarrow Z/\gamma^* \rightarrow \mu^+\mu^-$ at LO and EW NLO and the corresponding relative corrections ($\delta = d\sigma_{NLO}/d\sigma_{LO} - 1$) at the LHC ($\sqrt{s} = 14$ TeV) are provided in Table 3.3. The PDF set of MRST2004QED was used here. It was shown that the predictions of three different Monte Carlo programs (HORACE [51], SANC [52][53] and ZGRAD2 [54]) have a good agreement. The effect of the EW NLO corrections, differs for the three codes at most by two per mille and in general by few tenths of per mille.

	LO[μb]	NLO[μb]	δ [%]
HORACE	739.33(3)	762.20(3)	3.09(1)
SANC	739.3355(3)	762.645(3)	3.1527(4)
ZGRAD2	740(1)	764(1)	3.2(2)

Table 3.3: Tuned comparison of LO and EW NLO predictions for $p\bar{p} \rightarrow Z/\gamma^* \rightarrow \mu^+\mu^-$ at LHC ($\sqrt{s} = 14$ TeV) (taken from Ref. [50]).

The performance of different components in the electroweak corrections has been discussed in Ref. [45] for the NC Drell-Yan process. Figure 3.8 shows the relative NLO EW corrections (photonic and weak corrections), with respect to the dilepton invariant-mass distribution. For the experimental identification of the process, phase-space cuts are imposed for the calculation. As discussed, the cuts are not collinear safe, since photons within a small collinear cone around the leptons are not treated inclusively. In order to get closer to the experimental situation, the photon recombination procedure is applied. Therefore in Figure 3.8, for the photonic corrections, results are shown for both the bare muons ($\delta_{q\bar{q},phot}^{\mu^+\mu^-}$) and the ones recombined with photons ($\delta_{q\bar{q},phot}^{rec}$) when $\Delta R_{l\pm,\gamma} (= \sqrt{\Delta y^2 + \Delta\Phi^2}) \leq 0.1$. The M_{ll} distribution shows the famous large corrections from the final-state photon bremsstrahlung which significantly affect the shape of the resonance peak, due to the fact that events belonging to the Z pole are shifted to the low mass region. The corrections are smaller using the photon recombination procedure. The pure weak NLO corrections $\delta_{q\bar{q},weak}$ amount to few per cent in the resonance region and tend to be negative for higher mass, due to the EW Sudakov logarithms [55]. Figure 3.9 also shows the electroweak corrections beyond $O(\alpha)$ to the dilepton invariant-mass distribution. The effect of higher-order final-state radiation beyond $O(\alpha)$, $\delta_{multi-\gamma}^{\mu^+\mu^-}$, is generally not exceeding the 0.1% level. However, it becomes relevant for the mass distribution around the resonance, by reducing the bremsstrahlung effect. The universal weak corrections

beyond $O(\alpha)$, $\delta_{h.o.weak}$, are quite small over the whole mass range.

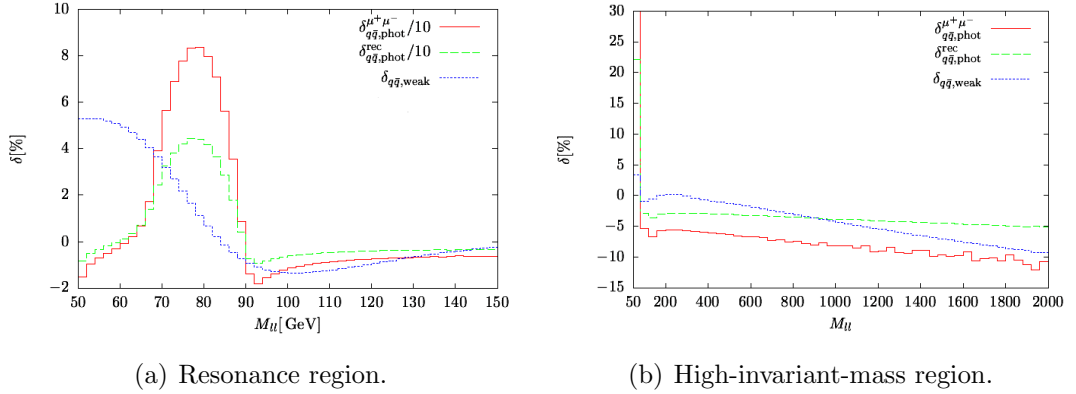


Figure 3.8: Dilepton invariant mass distribution and the relative EW NLO correction factors at the LHC in the resonance region and the high-invariant-mass region (taken from Ref. [45]).

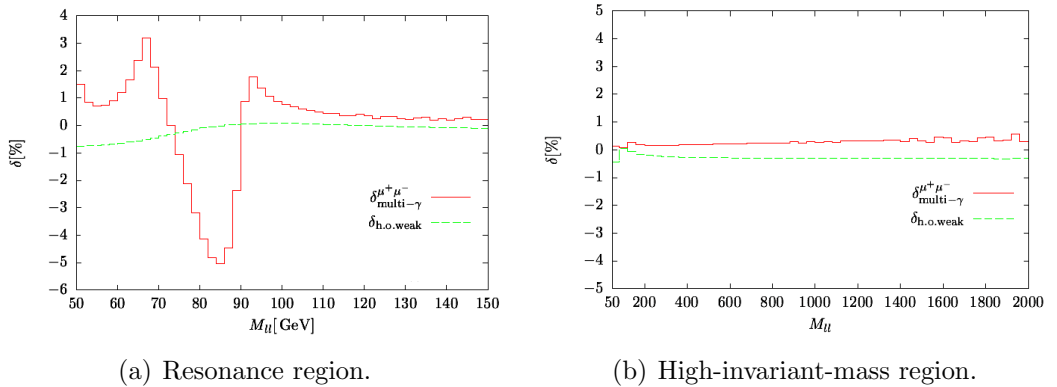


Figure 3.9: Dilepton invariant mass distribution and the relative EW correction factors beyond $O(\alpha)$ at the LHC in the resonance region and the high-invariant-mass region (taken from Ref. [45]).

For the Drell-Yan process, the pure weak corrections, as well as the interference effects between initial and final state radiation, have been recently calculated in G_μ scheme using the SANC program. The interference effects are below 0.1% and the pure weak effects may change the predicted cross section by $\sim 0.5\%$ [44].

3.4 Monte-Carlo Event Generation

In contemporary collider experiments, event generators are indispensable tools for the modelling of the complex physics processes that lead to the production of hundreds of particles per event. Generators are used to set detector requirements, to formulate analysis strategies, or to calculate acceptance corrections. They also illustrate uncertainties in the physics modelling. Generators model the physics of hard processes, initial- and final-state radiation, hadronization and decays, multiple interactions and beam remnants, and how these pieces come together. The detailed description of those processes are listed in this section. Additionally, an introduction to the various Monte-Carlo event generators in ATLAS is given at the end of the section.

3.4.1 Hard process

At sufficiently short distances, which can be probed at sufficiently large energies, the quarks and gluons (partons) can be regarded as free particles interacting with each other. In this regime the calculations of the scattering cross sections between quarks and gluons (partonic hard cross section) can be performed in perturbation theory, because the running coupling α_s is sufficiently small.

The cross section for a hard scattering process of hadrons A and B leading to the final state C can be given by [56]:

$$\sigma_{AB \rightarrow C} = \sum_{a,b} \int dx_a dx_b f_{a/A}(x_a, \mu^2) f_{b/B}(x_b, \mu^2) \hat{\sigma}_{ab \rightarrow C}. \quad (3.26)$$

Here $\hat{\sigma}$ denotes the cross section for the hard partonic process for a specific partonic initial state (ab). All parton combinations that can produce the final state C should be taken into account. For processes with many particles in the final state it would be further replaced by an integral over the allowed final-state phase space. The PDF $f_{a/A}(x_a, \mu^2)$ ($f_{b/B}(x_b, \mu^2)$) describes the probability of finding a parton a (b) with energy fraction x_a (x_b) in the beam hadron A (B), which is renormalised at scale μ^2 . The differential cross section $d\hat{\sigma}$ is given by [6]:

$$d\hat{\sigma} = \frac{|M|^2}{F} d\Phi, \quad (3.27)$$

where M is the parton-level matrix element or the probability amplitude of the transition between initial and final state. The factor F and $d\Phi$ are the Lorentz-invariant

flux and phase space factor, respectively. Various techniques exist to calculate the matrix-element at leading order. For $2 \rightarrow 2$ processes it is straightforward to draw all tree-level Feynman diagrams and apply the Feynman rules. The $2 \rightarrow 2$ QCD parton scattering processes are $qq' \rightarrow qq'$, $q\bar{q} \rightarrow q'\bar{q}'$, $q\bar{q} \rightarrow gg$, $qg \rightarrow qg$, $gg \rightarrow q\bar{q}$ and $gg \rightarrow gg$ [56].

According to the number of final-state objects, the hard processes can be: $2 \rightarrow 1$ processes, $2 \rightarrow 2$, $2 \rightarrow 3$, etc. From a programming point of view: the more particles in the final state, the more complicated the phase space and the whole generation procedure. Moreover, the hard process can be distinguished according to the physics scenario. For example: Hard QCD process (e.g. $qg \rightarrow qg$), W/Z production (e.g. $q\bar{q} \rightarrow \gamma^*/Z$), Deep Inelastic Scattering (e.g. $ql \rightarrow ql$), etc. One example of hadronic hard-scattering process is illustrated in Figure 3.1. The hard interaction of the two partons ($q\bar{q}$) gives the production of a vector boson (γ^*/Z), which decays into a di-lepton pair. The hadron remnants break up and lead to additional activity in the event, which is an important component of the Underlying Event (UE). UE is “everything except for the leading order process of interest”, including initial state radiation (ISR), final state radiation (FSR), beam remnants, multiple parton interactions (MPI), multiple proton-proton interactions (pile-up) and cavern background noise. Pile-up measures multiple proton-proton (more than one primary vertex) interactions within the same bunch crossings. UE is there even if there is only one primary vertex (one hard interaction of interest) and arises mainly from multiple parton interactions except the hard interaction of interest.

3.4.2 Initial- and final-state radiation

In processes that contain coloured and/or charged objects in the initial or final state, gluon and/or photon radiation may give large corrections to the overall topology of events. In this kind of corrections, a basic $2 \rightarrow 2$ process, can be transformed into $2 \rightarrow 3$, $2 \rightarrow 4$, and so on, final-state topologies. As the available energies are increased, hard emission of this kind is increasingly significant in determining the event structure [57].

There are two traditional approaches for the modelling of perturbative corrections: the matrix-element method and the parton-shower one [57]. The matrix-element method calculates the Feynman diagrams at a certain order, taking into account the exact kinematics, the full interference, and the helicity structure. However, this method becomes increasingly difficult in terms of higher order calculations, in particular for the loop diagrams. Also, the fact that the emission of multiple soft

gluons plays a significant role in the event structure building, sets a limit to the applicability of matrix elements. Since the available phase space for gluon emission increases with the available energy, the matrix-element method becomes less relevant for the full event structure for higher energies.

Higher order perturbative calculations predict infrared divergences for both real and virtual radiative contributions. According to the KLN-theorem [47][48][49], these divergences can mutually cancel for an inclusive cross section measurement. However, the divergences turn into a finite logarithmic contribution if the predictions are made exclusively at a certain resolution scale, e.g. the hadronisation scale. Such potentially large logarithms appear to each order in perturbation theory and they must be resummed to all orders. The resummation is done by the parton-shower approach. Given a parton that was produced at a scale t' , a new scale $t < t'$ is determined at which it should branch into two daughter partons and select the flavours and kinematics. The branchings are applied recursively to the daughter partons and only stopped at a cutoff scale in the order of the hadronisation scale, resulting in a parton branching cascade. The parton shower therefore takes charge of the evolution of partons from the scale of the hard scattering to the hadronisation scale [56].

The parton-shower approach is commonly used because of its simplicity and flexibility. Still, it has some shortcomings due to its approximate nature. The separation of initial and final state parton emission implies the neglect of interference terms between the two, and is not gauge invariant. The use of the leading logarithm approximation means that the emission of soft or collinear partons should be well described, while the emission of hard partons at large angles could be mistreated. Thus, the rate of well-separated multijet events, need not be well accounted for. The use of matrix-element is preferable for α_s determinations, angular distribution of jets, and other specialized studies.

3.4.3 Hadronisation and hadron decays

After the parton shower has terminated, a configuration of coloured partons at some low scale of the order of a few GeV emerges. Asymptotic freedom implies that the effective coupling becomes stronger at larger distances (equivalent to lower energies/momentum scales). QCD becomes strongly interacting and perturbation theory breaks down at the hadronisation scale. In this confinement regime, the coloured partons are transformed into the colourless hadrons, a process known as hadronization or fragmentation.

The best known hadronisation models are the Lund string model and the cluster-hadronisation model [56]. The Lund string model is the default for all PYTHIA applications [57][58]. It treats all but the highest-energy gluons as field lines, which are attracted to each other due to the gluon self-interaction and so form a narrow tube (string) of strong colour field. The model also predicts that in addition to the particle jets formed along the original paths of two separating quarks, there will be a spray of hadrons produced between the jets by the string itself. The cluster-hadronisation model is used in HERWIG [59][60]. In this model, quarks are combined with their nearest neighbours to form colour singlet clusters. The formed clusters are then fragmented into hadrons according to several prescriptions. If a cluster is too light to further decay, it is considered as the lightest single hadron of its flavour. If a cluster is massive enough, it decays isotropically into pairs of hadrons, following some rules that bring to the formation of an unbiased selection of decay products conserving flavour. A small fraction of the supermassive clusters are fragmented using an iterative fission model, until the masses of the products are below the fission threshold. This mechanism gives rise to clusters with the quantum numbers and provides a dynamic separation of the regimes of clusters and hadrons according to their masses and flavours.

Most of the particles produced by fragmentation are unstable and subsequently decay into the observable stable ones. The Monte Carlo therefore is required to include all particles with their proper mass distributions and decay properties. The normal treatment for the decay process is to choose the decay channel for individual particles according to their branching ratios.

3.4.4 Multiple parton interactions (MPI)

Due to the composite nature of hadrons, it is possible to have multiple parton hard scatterings, e.g. the hardest (primary) partonic interactions in hadronic collisions may be accompanied by the softer (secondary) ones among the beam remnants. The multiplicity of simultaneous partonic scatterings is naturally related to the scale. Large hadronic activity is observed in the soft regime, typically characterized by small transverse momenta (p_T) of the outgoing particles. In the case of relatively large p_T values, the observation of MPI will mostly focus on two simultaneous scatterings [61]. The original MPI model, first introduced in earlier versions of PYTHIA, featured p_T ordering, perturbative QCD cross sections dampened in the $p_T \rightarrow 0$ limit, and a variable impact parameter formalism. The above features remain in the latest PYTHIA 8 [58] and the newer model also introduced the p_T -ordered parton showers, sharing a common p_T evolution scale for the initial-/final- state radiation and MPI.

This is especially important for ISR and MPI, both of which directly compete for momentum from the beams. Additionally, HERWIG [59][60] itself implemented a simple colour reconnection model in order to complete the hadronization of events with MPI.

3.4.5 MC generators for ATLAS

Monte Carlo generators provide the four-vectors describing the results of LHC collisions. They are run from within Athena (ATLAS software framework) [62] and the generated event output is put into a transient store (named Storegate) in HepMC format [63]. A common interface, implemented via inheritance of a `GeneratorModule` class, guarantees common functionality for the basic generation steps. The generator information can be accessed and manipulated by the helper package like `TruthHelper` [64].

A long list of generators are used in Athena and they can be grouped into three categories. The first group of generators, the full generators, include parton shower and fragmentation. The ones belonging to this group are PYTHIA 6/8 [57][58], HERWIG(++) [59][60] and SHERPA [65]. The second group includes the specific purpose add-on packages to generators, e.g. PHOTOS [66], TAUOLA [67] and PHOJET [68]. The add-on packages retrieve the HepMC container from Storegate, modify the events and finally rewrite the HepMC events back into Storegate. The last group, the parton level generators, requires an interface to the full generator like PYTHIA and HERWIG to perform the parton shower and the fragmentation. Such generators are like MC@NLO [38], POWHEG [69] and ALPGEN [70]. More details on the above MC generators are listed in tables in Appendix A.

Simulation samples used in the study of this thesis are modelled using the PYTHIA generator. The package PHOTOS is interfaced to the standard QCD MC generators to simulate the effect of final state QED radiation. Therefore, some features about PYTHIA and PHOTOS are introduced.

PYTHIA

The PYTHIA MC generator is used as the main general-purpose event generator in ATLAS [57][58]. The default parton distribution in PYTHIA is CTEQ5L [23], but other PDFs found in the LHAPDF library [71] can easily be linked. It is possible to use separate PDF sets for the hard interaction, for the subsequent showers, and

for the multiple interactions. The initial- and final-state evolution and the multiple interactions are interleaved into one common decreasing p_T sequence since PYTHIA 6.3. Hadronisation is based solely on the Lund string fragmentation framework and particle data have been updated in agreement with the 2006 PDG tables [72].

The standard PYTHIA event generation machinery does not contain any full higher-order matrix elements. Starting from the hard interaction, initial- and final-state radiation corrections are normally added by making use of the parton-shower language. The only process for which PYTHIA offers a matrix-element option is $e^+e^- \rightarrow \gamma^*/Z^0 \rightarrow q\bar{q}$, where higher-order QCD corrections can be obtained either with parton-shower or with second-order matrix elements (available for $q\bar{q} + q\bar{q}g + q\bar{q}gg + q\bar{q}q'\bar{q}'$ production). Purely weak effects are not included in PYTHIA. There are several cases where higher-order matrix elements are included at the Born level. For instance, in the case of W production at a hadron collider, except the lowest order process $q\bar{q}' \rightarrow W$, the other two first-order processes $qg \rightarrow Wq'$ and $q\bar{q}' \rightarrow Wg$ are included. The $2 \rightarrow 2$ matrix elements are divergent when $p_T \rightarrow 0$ and should not be used down to the low p_T region. A correct treatment in this region would need to take into account loop corrections to cancel the singularities, which are not available in PYTHIA. Depending on the physics application, PYTHIA could be used differently. In an inclusive description, which is dominated by the small p_T region, the preferred solution is to combine the lowest-order matrix elements with parton showers. For the process where the large- p_T tail might be of interest, the shower approach may be inefficient. The matrix-element alternative allows reasonable cuts to be inserted from the beginning of the generation procedure and should give a more precise prediction of the high- p_T event rate than the approximate shower procedure. Therefore it is recommended to start from the $2 \rightarrow 2$ matrix elements and add showers, thus giving a decent description over the whole p_T range.

The MC generator parameter sets, so-called “tunes”, can provide an optimal description of the ATLAS data for the use in LHC physics studies. The tunes have been constructed for the PYTHIA 6 in the ATLAS 2011 MC simulation production campaign (MC11) [73]. The tunes are performed in four stages, using the MRST LO** PDF [74]:

- 1 Flavour parameters tuned to hadron multiplicities and their ratios, measured in e^+e^- collisions;
- 2 Final state radiation and hadronisation parameters, tuned to event shapes and jet rates measured in e^+e^- collisions;
- 3 Initial state shower parameters and primordial k_T , tuned to Tevatron and LHC

data;

- 4 Multiple-parton interactions, tuned to Tevatron and LHC data.

The parameters used for the tuning of PYTHIA 6 for MC11 can be found in Ref. [73]. Moreover, an extension of the tuning study for the PYTHIA family, including the C++ PYTHIA 8, is presented in Ref. [75]. The primary changes in PYTHIA 6 are driven by concerns with the parton shower configuration and by a desire to construct equivalent and systematic variation tunes for a variety of PDFs.

PHOTOS

As an “after-burner” algorithm, PHOTOS adds bremsstrahlung photons to already existing events, which is filled in by a host generator (with the QED FSR brems off) and transmitted by means of a standard HEPEVT event record (the information about four-vectors of particles taking part in the process and the topology of the process). PHOTOS intervenes at every event decay branching. With certain probability extra photons may be added and the kinematics of other particles can be adjusted. PHOTOS has a unique double iterative algorithm: an internal loop is over emitters; an external one is over consecutive emission. In the iterative algorithm for multiphoton emission, the number of photons to be generated is based on a Poissonian distribution. The QED ISR-FSR interference is implemented in PHOTOS as the a Carlo interference weight. Pure weak corrections are not included in the current PHOTOS interfaces [66].

Instead of the order-by-order perturbative calculations, the most popular method in QED to include the bremsstrahlung effects and improve the convergence of the perturbative expansion, is exponentiation. In the leading-log approximation, partially inclusive formulae exhibit factorization properties of QED. A matrix element formula for particle decay accompanied by bremsstrahlung photon emission can be factorized to Born-level terms times the bremsstrahlung factor. This approximation, taking into account both real and virtual corrections, converges to an exact expression in the soft-photon region of phase space. Within PHOTOS, the infrared divergences that originate from the emission of real and virtual photons may be regularised and cancelled out order-by-order: a technical parameter of the minimum photon energy is defined, and integration over the directions of photons with energies lower than the cut-off is performed. The collinear region of the phase space can be treated properly as well: the singularities are regulated by the masses of the charged particles. In the

exponentiated version of PHOTOS (multi-photon emission mode), the value of the infrared cut-off parameter E_γ^{min}/M can be lowered down to $\sim 10^{-7}$. The multi-photon emission mode is used in ATLAS.

PHOTOS can be used for simulation chains at LHC aiming at 0.2 % precision tag in single Z or W production and at their common studies [76] [77]. Tests have been performed with KKMC [78] to confirm the physics precision of FSR. KKMC is the program used at LEP for the precision measurements of Z . It is based on exclusive exponentiation and features second order matrix elements for FSR. Agreement better than 0.2 % in experimental cuts (ATLAS, CDF) between PHOTOS and KKMC was found. The recent comparisons performed between PHOTOS and SANC [52][53], with first order matrix element, decays of Z and W, also multi-photon emission, are still in progress.

The interface of PHOTOS to PYTHIA is available provided that the parameter of PARJ(90) is set as 20000 in the latter [79]. This parameter represents the threshold in GeV below which leptons do not radiate, thus preventing the lepton radiation in PYTHIA and reducing double counting. Since no lepton QED radiation is implemented in HERWIG, the inclusion of PHOTOS is simple and possibly also rather necessary. The standard switches and configuration parameters can be set in the PhotosCommand in the JobOption file [79]:

- photos pmode(Default=1): Radiation mode of photons;
- photos xphcut(Default=0.01): Infrared cutoff for photon radiation;
- photos alpha(<0 leave Default=0.00729735039): α_{QED} value used in PHOTOS;
- photos interf(Default=1): Photon interference weight switch;
- photos isec(Default=1): Double bremsstrahlung switch;
- photos itre(Default=1): Higher bremsstrahlung switch;
- photos iexp(Default=1): Exponential bremsstrahlung switch;
- photos iftop(Default=0): Switch for $gg(qq) \rightarrow t\bar{t}$ process radiation.

Notice that if the exponential mode (iexp=1) is set, the original xphcut value can be overruled by the default Infrared cutoff (10^{-7}) in the exponential mode.

Chapter 4

The ATLAS Experiment at the Large Hadron Collider

4.1 Large Hadron Collider

The Large Hadron Collider (LHC) [80], the world's largest particle accelerator, is located at the European Organization for Nuclear Research (CERN) near Geneva, Switzerland. It reuses the 27 km circumference tunnel that was built for the previous big accelerator, LEP [81]. The LHC is designed to accelerate two beams of particles of the same kind, either protons or lead ions, which will travel in the opposite directions and finally collide once they reach the desired energy. ALICE [82], ATLAS [83], CMS [84] and LHCb [85] are installed in four huge underground caverns built around the four collision points of the LHC beams.

The acceleration is achieved by a chain of accelerators, as illustrated in Figure 4.1. The brief story of a proton accelerated through the accelerator complex at CERN is as follows: protons are accelerated in a linear accelerator (LINAC) at the first step. Then they are injected into the Proton Synchrotron Booster (PSB) at an energy of 50 MeV. The booster accelerates them to 1.4 GeV. The beam is then fed to the Proton Synchrotron (PS) where it is accelerated to 25 GeV. Protons are then sent to the Super Proton Synchrotron (SPS) where they are accelerated to 450 GeV. They are finally transferred to the LHC (both in a clockwise and an anticlockwise direction, the filling time is 4'20" per LHC ring) where they are accelerated for 20 minutes to their nominal energy of 7 TeV. Beams will circulate for many hours inside the LHC beam pipes under normal operating conditions.

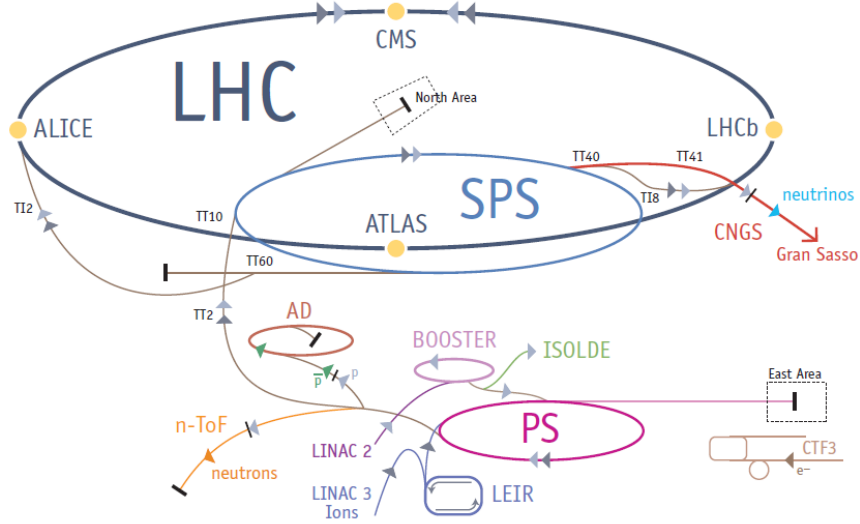


Figure 4.1: Schematic layout of the LHC injector chain.

LHC started its first proton-proton collision at $\sqrt{s} = 0.9$ TeV and later at $\sqrt{s} = 2.76$ TeV in late 2009. The first collision at $\sqrt{s} = 7$ TeV has been taken since March 2010, which led to about eight months of data taking before a few weeks of heavy ion collisions and the winter shutdown. Since March 2011, proton run has restarted at $\sqrt{s} = 7$ TeV till now, still with a few weeks of heavy ion collisions and the winter shutdown. The current LHC run is scheduled to continue till the end of 2012, which will provide the experiments enough data to fully explore the energy range accessible with 3.5 TeV per beam collisions for new physics before preparing the LHC for higher energy running. A long shutdown will then start in the year 2013 to prepare for an increase of the total energy towards the LHC design $\sqrt{s} = 14$ TeV.

The peak luminosity was $2.1 \times 10^{32} \text{ cm}^{-2}\text{s}^{-1}$ in 2010 and $3.65 \times 10^{33} \text{ cm}^{-2}\text{s}^{-1}$ in 2011. The recorded luminosity at $\sqrt{s} = 7$ TeV delivered to the ATLAS experiment was 45 pb^{-1} in 2010 and reached 5.25 fb^{-1} in 2011 [86]. Figure 4.2 shows the total integrated luminosity versus day delivered to (green), and recorded by ATLAS (yellow) during the stable beams for proton-proton collision at $\sqrt{s} = 7$ TeV. The delivered luminosity accounts for the luminosity delivered from the start of stable beams until the LHC requests ATLAS to turn the sensitive detector off to allow a beam dump or beam studies. The luminosity is determined from counting rates measured by the luminosity detectors.

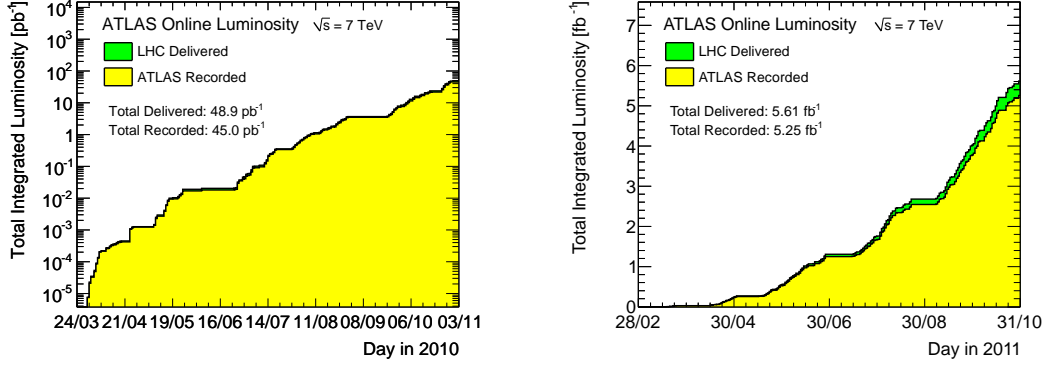


Figure 4.2: Cumulative luminosity versus day delivered to (green), and recorded by ATLAS (yellow) during stable beams for pp collisions at $\sqrt{s} = 7$ TeV in 2010(left) and 2011(right) (taken from Ref. [86]). The left plot is shown in logarithmic scale.

4.2 ATLAS Detector

ATLAS (A Toroidal LHC ApparatuS) is a general-purpose detector designed to cover the widest possible range of physics at the LHC, searching for new discoveries in the head-on collisions of protons of extraordinarily high energy. The main feature of the ATLAS detector is its enormous doughnut-shaped magnet system. This consists of eight 25 m long superconducting magnet coils, arranged to form a cylinder around the beam pipe through the centre of the detector. It is the largest-volume detector ever constructed, with 25 m height, 44 m length and weights 7000 tonnes (Figure 4.3).

The coordinate system of the ATLAS detector is defined in cartesian coordinates with the z axis running along the beam pipe, the x axis pointing to the outside of the LHC ring, and the y axis pointing up. The origin of the coordinate system is located at the centre of the detector. However, often spherical coordinates are used to describe the subdetector and physics processes. The azimuthal angle $\varphi = [0, 2\pi]$ is the angle formed with the $x - y$ plane. The polar angle $\theta = [0, \pi]$ is the angle formed with the z axis. θ is often replaced by the pseudorapidity η defined as $\eta = -\ln(\tan(\theta/2))$. This is equal to the rapidity y in the limit of massless objects (see Section 3). The difference in rapidity of two particles is invariant under Lorentz boost along the beam axis. In ATLAS the high p_T electrons, muons and light quark jets can be approximately considered as massless particles.

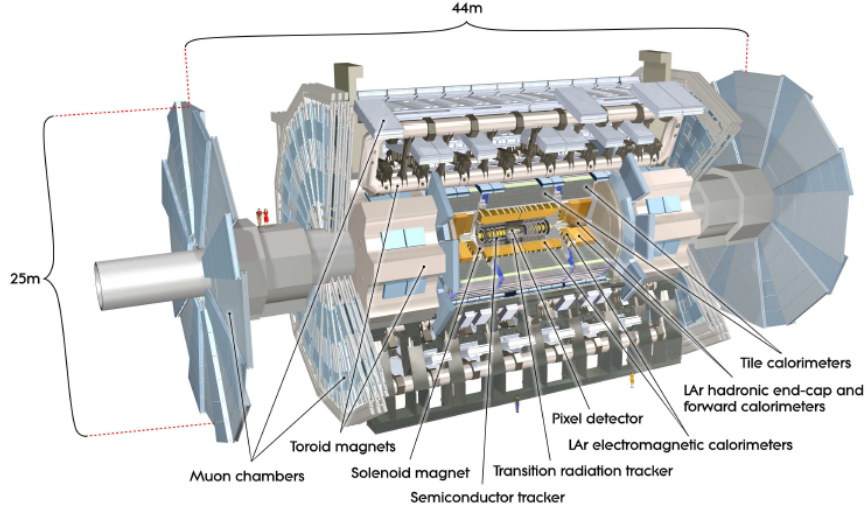


Figure 4.3: Cut-away view of the ATLAS detector (taken from Ref. [83]). The dimensions of the detector are 25 m in height and 44 m in length. The overall weight is approximately 7000 tonnes.

4.2.1 Inner Detector

At design luminosity thousands of particles will emerge from the collision point every 25 ns within $|\eta| < 2.5$, creating a large track density in the detector. To achieve the high-precision measurements required by the physics processes, it is necessary to have a fine granularity. The inner detector is therefore composed of three subsystems, Pixel, SemiConductor Tracker (SCT) and Transition Radiation Tracker (TRT), to offer these features. The charge, momentum, track direction and impact parameter (shortest distance to the z axis) are measured in the inner detector. It can also identify the origin of the particle (vertexing), and determine if the track originated from the interaction point or at some distance from this (secondary vertex), as is the case for B-mesons and converted photons. The plan view of a quarter-section of the ATLAS inner detector is given in Figure 4.4, showing each of the major detector elements with its active dimensions and envelopes. It is immersed in a 2 T magnetic field, extending 7 m in length and 1.15 m in radius, covering pseudorapidities up to $|\eta| < 2.5$.

Pixel Detector

The pixel detector is located closest to the beam pipe. It consists of three cylindrical barrel layers and three discs in each endcap, covering a range in pseudorapidity of $|\eta| < 2.5$. A charged particle traversing the detector produces electron/hole pairs in the semiconductor sensors. The free charge is collected applying a bias voltage. If the collected charge is above 0.5 fC (≈ 3000 electrons), the readout electronics write out both the pixel address and the time over threshold (ToT). Later, the ToT is used to recover the amount of charge that was deposited in the sensor, resulting in a measurable current. The intrinsic accuracies are of $10 \mu\text{m} \times 115 \mu\text{m}$ in the $(R\phi) \times z$ direction for barrel and $10 \mu\text{m} \times 115 \mu\text{m}$ in the $(R\phi) \times R$ direction for end-cap disk. Altogether the pixel detector has approximately 80.4 million readout channels.

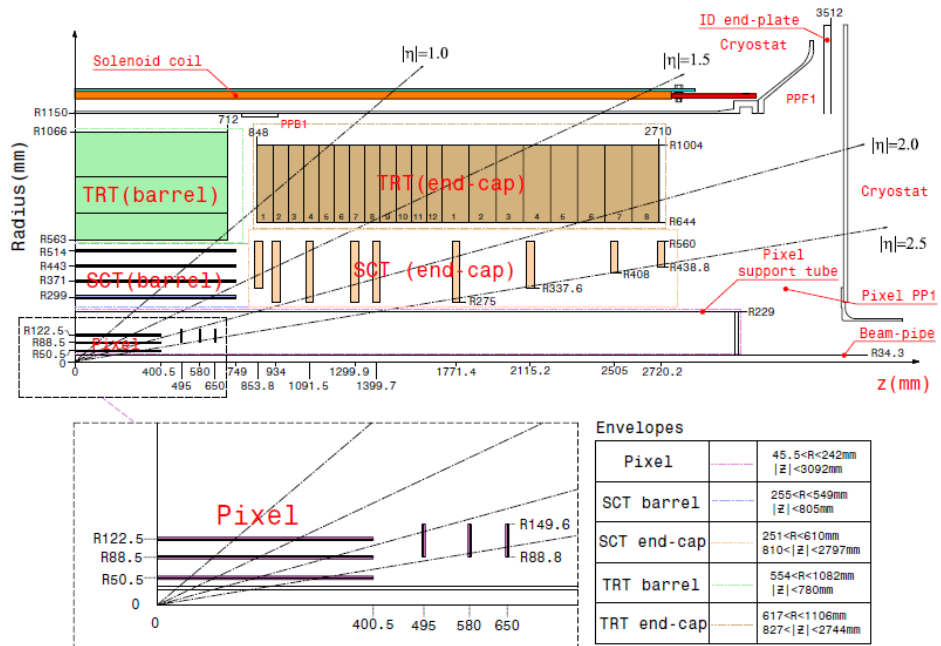


Figure 4.4: Plan view of a quarter-section of the ATLAS inner detector showing each of the major detector elements with its active dimensions and envelopes (taken from Ref. [83]).

SCT Detector

The SCT detector surrounds the pixel detector. It consists of one cylindrical barrel and two endcaps. The SCT measurements are very important for the final tracking resolution, impact parameter calculation and the positioning of the z -coordinate of the vertex. Its main purpose is the momentum and impact parameter measurement of charged particles as well as vertex position determination. Good pattern recognition is also needed. Precise points in $R\varphi$ - and z - direction are provided by the silicon microstrip detectors, using small angle stereo layers to supply the z measurement. All modules are built on four single-sided p-on-n semiconducting silicon detectors. Those follow the same working principle like the pixels. Here, the p-layer is segmented into strips whereas each strip is read out by an individual channel resulting in a spatial information. It provides a spatial resolution of $17\ \mu\text{m} \times 580\ \mu\text{m}$ in $(R\varphi) \times z$ direction for barrel and $17\ \mu\text{m} \times 580\ \mu\text{m}$ in $(R\varphi) \times R$ direction for end-cap disk. In total the SCT offers about 6.3 million readout channels.

TRT Detector

To measure tracks within $|\eta| < 2.0$, the TRT was installed as the outermost layer of the inner detector. It provides $R\varphi$ - information only, with an intrinsic accuracy of $130\ \mu\text{m}$ per straw. It is central to the track momentum estimation. Additionally, the transition radiation properties of the TRT material allow electron identification. The TRT modules are made of polyimide drift tubes called straws. The straw tube wall is made of multi-layer films with a thickness of $35\ \mu\text{m}$ bonded together back-to-back. The design guarantees that the straws have good electrical and mechanical properties. The tubes are filled with a non-flammable xenon-based gas mixture of 70% Xe, 27% CO₂ and 3% O₂ [87]. When a charged particle crosses the straw tube, the gas is ionised and the charge produced is collected in the anode. Measuring the time it takes to collect the charge, the distance of the track to the anode can be estimated. This distance is known as the drift radius. The total number of TRT readout channels is approximately 351,000.

Tracks with a transverse momentum above 0.5 GeV typically pass through at least 36 straws, except in the barrel-endcap transition where a minimum of 22 straws are crossed. The layers of straws are interleaved with polypropylene radiators which emit transition radiation photons when charged particles traverse them. The electrons produce significantly more photons than pions. The mixture of gas filling the straws is sensitive to these transition photons, which can be used to identify tracks as electrons. Efficiencies up to 90% with a pion rejection of 100:1 can be achieved for energies

above 1 GeV. Due to the length of the straws, the mean hit occupancy is much higher than for the SCT or pixel detectors. This makes pattern recognition in the TRT challenging.

4.2.2 Calorimeters

The calorimetric system is located between the inner detector and the muon spectrometer, covering the pseudorapidity range $|\eta| < 4.9$. Over the η region matched to the inner detector, the fine granularity of the EM calorimeter is ideally suited for precision measurements of electrons and photons. The coarser granularity of the rest of the calorimeter is sufficient to satisfy the physics requirements for jet reconstruction and missing transverse energy measurements.

The calorimeters require good electromagnetic and hadronic shower containment. The technology is to force the incoming particle to interact with the nuclei in the media producing showers of particles by using dense material. The showers are initiated in the absorber material and extend into the active material where the energy of the shower produced is measured. The total signal collected is used to recover the energy of the incoming particle. There are two different kinds of active materials used in ATLAS, liquid argon (LAr) and tiles of scintillating plastic. LAr is a radiation hard material which can provide an intrinsic linear behaviour, stability of the response in time and radiation tolerance at an affordable price. LAr detectors are used in the electromagnetic (EM) calorimeters, the Hadronic Calorimeter End-caps (HEC) and the Forward Calorimeter (FCal). Plastic scintillators are used in the hadronic barrel Tile Calorimeter (Tile). The calorimeters use different absorbing materials such as lead, iron, copper or tungsten.

An additional function of the calorimeters is to limit the amount of punch-through particles escaping to the muon spectrometer (MS). Hence, calorimeter depth is an important design consideration. The total thickness of the EM calorimeter exceeds 22 radiation lengths (X_0) in the barrel and 24 X_0 in the end-caps. The hadronic part comprises 9.7 interaction lengths (λ) in the barrel and 10 λ in the end-caps. The total thickness, including 1.3 λ from the outer support, is 11 λ at $\eta = 0$ and has been shown both by measurements and simulations to be sufficient to reduce punch-through into the MS well below the irreducible level of prompt muons or the ones from pion and kaon decays. Together with the large η -coverage, this thickness also ensures a good missing transverse energy measurements. The material budget of the calorimeters as a function of pseudo-rapidity is presented in Figure 4.5 [83].

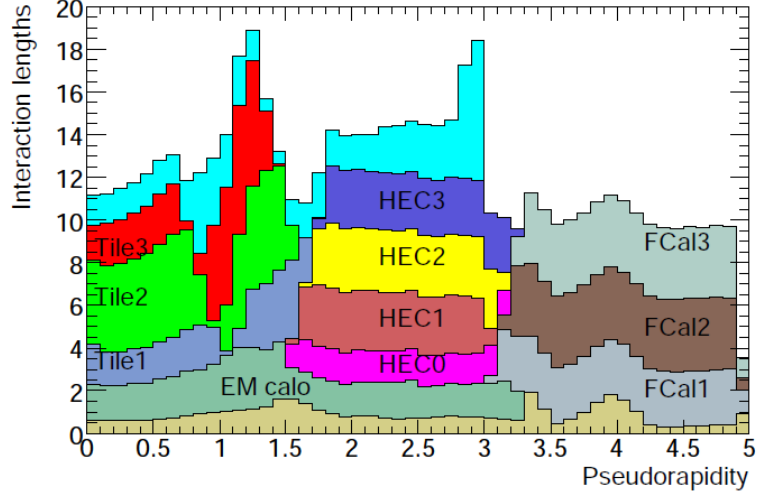


Figure 4.5: Cumulative amount of material, in units of interaction length, as a function of $|\eta|$, in front of the electromagnetic calorimeters, in the electromagnetic calorimeters, in each hadronic layer, and the total amount at the end of the active calorimetry (taken from Ref. [83]).

LAr Electromagnetic Calorimeter

The EM calorimeter is divided into a barrel, situated within $|\eta| < 1.475$, and two end-caps found within $1.375 < |\eta| < 3.2$. The barrel shares the cryostat with the central solenoid, eliminating two vacuum walls. The end-caps are hosted in their own cryostats. The granularity of the EM calorimeter is especially fine in the region closest to the inner detector, making it possible to distinguish between showers originating near to each other. The barrel and end-cap modules are divided into three longitudinal compartments also called samplings. The first sampling has the finest granularity which allows precise cell clustering. The second sampling is thicker and is where the electrons and photons deposit the largest amount of energy. The last sampling is used to recover high energetic showers that extend beyond the second sampling, which allows to discriminate between electromagnetic and hadronic showers. In the central region of $|\eta| < 1.8$, a presampler is located. The energy measured in the presampler is used to correct for the energy lost by electrons upstream of the calorimeter. A sketch of a barrel module of the EM calorimeter is shown in Figure 4.6 [83]. The different layers are clearly visible with the ganging of electrodes in φ . The granularity in η and φ of the cells of each of the three layers and of the trigger towers is also shown. The EM calorimeters use lead plates as absorbers, sandwiched between two stainless

displays the measured energy distribution for clusters of $\Delta\eta \times \Delta\varphi = 3 \times 3$ cells in the range $0.3 < |\eta| < 0.4$ in the LAr calorimeter.

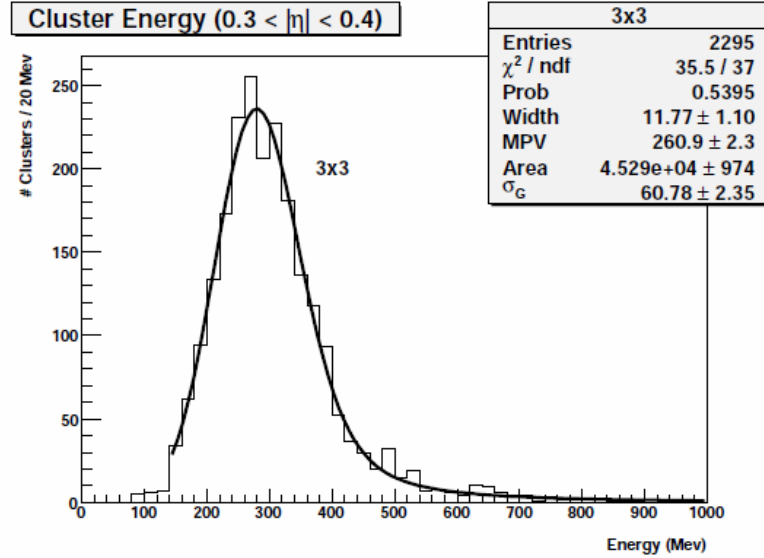


Figure 4.7: Measured 3×3 cluster energy distributions in the range $0.3 < |\eta| < 0.4$ in the LAr EM calorimeter, using cosmic muons (taken from Ref. [88]).

Hadronic Calorimeters

The hadronic calorimeter is built around the EM calorimeter. It is designed to measure the energy deposited by jets of particles formed by the hadronisation of gluons and quarks. Since hadrons are much heavier than electrons, hadronic showers are much longer and wider than their EM counterparts. Therefore the hadronic calorimeter requires a higher density and an absorber material with higher Z . The material thickness of hadronic calorimeter is enough to stop almost all kinds of particles originating in the proton collisions, except the muons and the weakly interacting neutrinos. However, the hadronic interaction of high energetic particles in the calorimeter absorbers, produce a large number of slow neutrons and low energy photons that form a dense cavern background in the muon detector.

Tile The tile calorimeter is placed directly outside the EM calorimeter envelope. It consists of a central barrel covering up to $|\eta| < 1.0$ and two extended barrels on

each side covering the range $0.8 < |\eta| < 1.7$. It is a sampling calorimeter using steel as absorber and scintillator tiles as active medium. Steel has a shorter interaction length than lead and is therefore more suitable for a hadronic calorimeter. A hadron entering the Tile calorimeter interacts inelastically with the steel plates, producing secondary particles resulting in a hadronic cascade (hadronic shower). Those excite the scintillator tiles, the two sides of which are connected to wavelength-shifting fibres. Wavelength-shifting fibres collect the scintillation light produced in the scintillators and bring it to photo-multipliers (PMT's). The orientation of the scintillator tiles radially and normal to the beam line, in combination with wavelength-shifting fibre readout on the tile edges, allows for almost seamless azimuthal calorimeter coverage.

LAr Hadronic End-cap Calorimeter (HEC) The hadronic end-cap calorimeter, consists of two independent wheels per end-cap, located behind the end-cap EM calorimeter and sharing the same LAr cryostats. To reduce the drop in material density at the transition between the end-cap and the forward calorimeter, the HEC extends out to $|\eta| = 3.2$, thereby overlapping with the forward calorimeter (see below). Similarly, the HEC η range also slightly overlaps with that of the tile calorimeter by extending to $|\eta| = 1.5$. To reach the required λ , copper is used as absorber, which has a shorter λ than steel. The wheels closest to the interaction point are built from 15 mm parallel copper plates, while those further away use 50 mm copper plates. The copper plates are interleaved with 8.5 mm LAr gaps, providing the active medium for the HEC.

LAr Forward Calorimeter (FCal) The task of the forward calorimeter is mainly to complete the 4π sphere coverage as hermetically as possible. This is necessary for a good missing energy measurement. It is integrated into the end-cap cryostats, as this provides clear benefits in terms of uniformity of the calorimetric coverage as well as reduced radiation background levels in the muon spectrometer. The FCal consists of three modules: the first, made of copper, is optimised for electromagnetic measurements, while the other two, made of tungsten, measure predominantly the energy of hadronic interactions. Each section is built by a metal matrix with regular spaced longitudinal channels filled with the electrode structure consisting of concentric rods and tubes. The LAr filled in the gap between the rods and the tubes is the sensitive medium.

4.2.3 Muon Spectrometer

The outermost part of the ATLAS detector is the muon spectrometer. It is designed to detect the charged particles exiting the calorimeter. When charged particles reach the muon system their trajectories are deflected by the magnetic field created by the superconducting toroid magnets. Thus, their momentum can be measured. In the barrel region ($|\eta| < 1.4$), the trajectories are measured in three cylindrical layers of chambers arranged parallel to the beam pipe. In the endcap ($1.6 < |\eta| < 2.7$), the chambers are aligned in planes perpendicular to the beam axis. In the barrel, the deflection is caused by the large toroid coils, which generates a magnetic toroid field with a strength of 0.5 T. In the endcap region the tracks are bent by the field generated in the endcap magnets, with a magnetic field of 1 T in the forward directions. In the transition region ($1.4 < |\eta| < 1.6$), magnetic deflection is provided by a combination of barrel and end-cap fields. This magnet configuration provides a field which is mostly orthogonal to the muon trajectories, while minimising the degradation of resolution due to multiple scattering. Figure 4.8 gives cross-sections of the muon system in the planes transverse to, and containing, the beam axis [83]. A precision measurement is provided by Monitored Drift Tubes (MDTs) and Cathode Strip Chambers (CSCs). The trigger system is composed of Resistive Plate Chambers (RPCs) in the barrel region and Thin Gap Chambers (TGCs) in the end-cap regions.

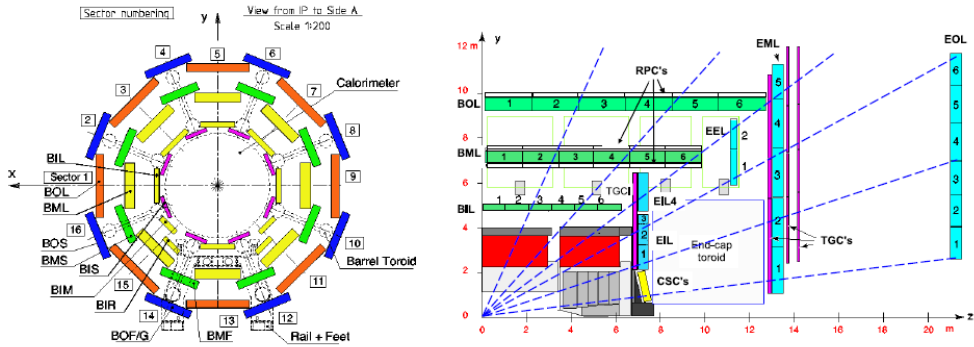


Figure 4.8: Left: Cross-section of the barrel muon system perpendicular to the beam axis (non-bending plane), showing three concentric cylindrical layers of eight large and eight small chambers. Right: Cross-section of the muon system in a plane containing the beam axis (bending plane). Infinite-momentum muons would propagate along straight trajectories which are illustrated by the dashed lines and typically traverse three muon stations (taken from Ref. [83]).

MDTs The MDTs provide precision measurements over most of the pseudorapidity range $|\eta| < 2.7$ except for the inner most endcap wheel where they only cover up to $|\eta| < 2.0$. MDTs consist of aluminium tubes of 30 mm diameter, which contain a central wire working as an anode. The tubes are filled with a gas mixture of 97% *Ar* and 3% *CO*₂ at a pressure of 3 bar. A muon crossing the tube will cause the ionisation of the gas producing a net charge that will drift towards the anode. The distance between the traversing muon and the anode is measured using the drift time spent for the collected charge to reach the anode. The drift time can be resolved in a high-precision space measurement of the track crossing the tube, taking the trigger signal of the RPCs or TGCs into account. The average spatial resolution is about 80 μm per tube, or 35 μm for the entire chamber.

CSCs The forward region ($2.0 < |\eta| < 2.7$), where the particle flux is more intense, is covered with the cathode strip chambers. The CSCs are multiwire proportional chambers with both cathodes segmented, one with the strips parallel to the wires and the other perpendicular providing two coordinate measurements. There are eight small and eight large chambers in each inner end-cap wheel, with a width of 1.519 mm and 1.602 mm respectively. Each chamber contains four CSC planes resulting in four independent measurements in η and φ along each track. The spatial resolution of the CSCs is 60 μm in the bending plane and 5 μm perpendicular to the bending plane. Multi-track ambiguities are reduced by correlating the amount of charge collected in the two planes of orthogonal strips.

RPCs The RPCs provide a fast trigger to deliver track information within a few tens of nanoseconds in the barrel region ($|\eta| < 1.05$). The RPC modules consist of a gas-filled volume between high-resistive phenolic-melaminic plates, the plate spacing is 2 mm. A charged particle crossing the gas volume creates a charge avalanche due to ionization, the electric signal is read out via capacitive coupling by metallic strips mounted on the outer faces of the resistive plates.

TGCs The TGCs are used to provide a fast trigger and an azimuthal coordinate measurement to complement the MDTs in the end-cap region, covering a range of $1.05 < |\eta| < 2.4$. They are multi-wire proportional chambers with a wire-to-cathode distance of 1.4 mm and a wire-to-wire distance of 1.8 mm, filled with a mixture of *CO*₂ (55%) and *n* - *C*₅*H*₁₂ (45%). They can be used as bunch-crossing trigger, since the signal arrives within 25 ns after the particle crossed the chamber with a probability of 99%.

4.2.4 Forward Detectors

Three smaller detector systems, depicted in Figure 4.9 [83], dedicated to the coverage of the very forward region are installed to the main ATLAS detector systems. LUCID (Luminosity measurement using Cerenkov Integrating Detector), situated at ± 17 m from the interaction point, is the only detector for online relative luminosity measurement for ATLAS. It detects inelastic p-p scattering in the forward direction, based on the principle that the number of interactions in a bunch-crossing is proportional to the number of particles detected in the forward region covered by it. ALFA (Absolute Luminosity For ATLAS), located at ± 240 m, determines the absolute luminosity by elastic p-p scattering at small angles. ZDC (Zero Degree Calorimeter), located at ± 140 m, determines the centrality of the heavy-ion collisions.

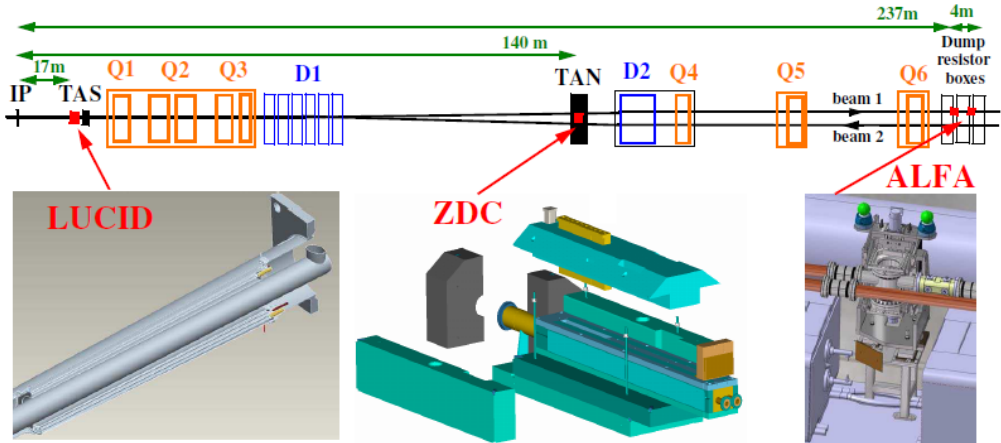


Figure 4.9: Placement of the forward detectors along the beam-line around the ATLAS interaction point (IP) (taken from Ref. [83]).

4.2.5 Magnet System

The ATLAS magnetic system consists of one superconducting solenoid and three superconducting toroids (one barrel and two end-caps). The entire system is 22 m in diameter and 26 m in length, being capable of storing a total amount of energy of 1.6 GJ. The solenoid magnet which surrounds the inner detector is responsible for the bending force inside the inner tracker system. It provides a 2 T axial magnetic field and was designed to keep the amount of material before the calorimeters as low

as possible. The toriod produces a toroidal magnetic field of approximately 0.5 T and 1 T for the muon detectors in the central and end-cap regions, respectively. It consists of eight coils encased in stainless steel vacuum vessels. Figure 4.10 shows the general layout with the complete magnet system including the tile calorimeter steel.

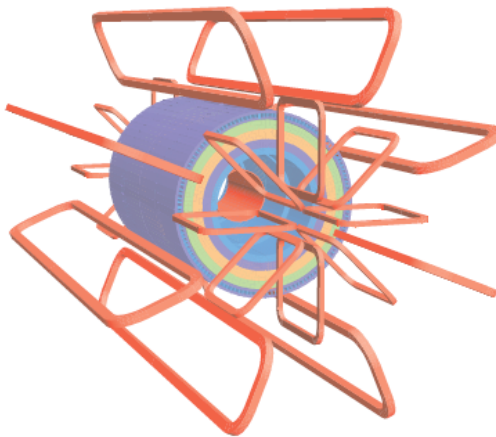


Figure 4.10: Geometry of magnet windings and tile calorimeter steel (taken from Ref. [83]).

4.2.6 Trigger and Data Acquisition

One of the main challenges of the LHC experiments is to record interesting events given the huge amount of data produced and the high collision rate. At LHC center-of-mass energy, a bunch crossing rate of 40 MHz produces 10^9 inelastic events at the design luminosity, while the data recording, based on the available technology and resources, is limited to about 200 Hz. To reduce the amount of data, a three-level trigger system has been installed in ATLAS: Level-1 (L1), Level-2 (L2) and the event filter. L1 is fully hardware based, while the other two are software based. Each trigger refines the decision made by the previous stage and requires additional criteria. L2 and the event filter together form the High-Level Trigger (HLT). An overview of the data flow is shown in Figure 4.11 [83].

The L1 trigger is based on the reduced granularity information from the muon spectrometer (RPC and TGC) and the calorimeters. The trigger chambers are used to identify high transverse momentum muons. The selection for calorimeter objects is based on “trigger tower” information, which have a typical size of $\Delta\eta \times \Delta\varphi = 0.1 \times$

In parallel to the trigger, two independent, complementary and interacting systems are responsible for the data taking and the control of the experiment infrastructure: the data acquisition (DAQ) and the detector control system (DCS). After an event is accepted by the L1 trigger, the data from the pipelines are transferred off the detector to the Readout Drivers. Digitised signals are formatted as raw data prior to being transferred to the DAQ. The first stage of the DAQ, the readout system, receives and temporarily stores the data in local buffers. It is subsequently solicited by the L2 trigger for the event data associated to ROI's. The events selected by the L2 trigger are then transferred to the event-building system and subsequently to the event filter for final selection. Events passing the event filter are moved to permanent storage at the CERN computer centre. The DAQ also provides for the configuration, control and monitoring of the hardware and software elements of the detectors. On the other hand, the DCS ensures coherent and safe operation of ATLAS. It handles the control of the detector equipment and related infrastructure, monitoring the operational parameters such as temperature and power-supply voltages. Both systems are capable of taking corrective actions and additionally provide a human interface for the full control of ATLAS and its sub-detectors.

4.3 ATLAS Offline Software

4.3.1 The Athena Framework

The Athena framework is an enhanced version of the Gaudi framework [89] that was originally developed by the LHCb experiment [85], but is now a common ATLAS-LHCb project and is in use by several other experiments including GLAST [90] and HARP [91]. Athena and Gaudi are concrete realizations of a component-based architecture which was designed for a wide range of physics data-processing applications. The component-based feature allows flexibility in developing both a range of shared components and, where appropriate, components that are specific to the particular experiment and better meet its particular requirements. The major components that have been identified within the architecture are shown in Figure 4.12 [92]. All levels of processing of ATLAS data, from high-level trigger to event simulation, reconstruction and analysis, take place within the Athena framework.

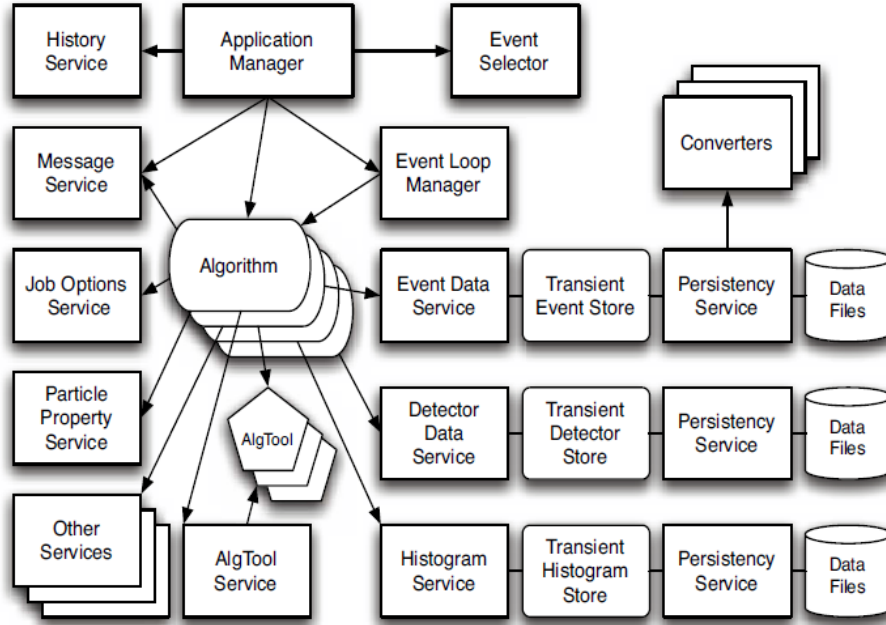


Figure 4.12: Athena Component Model (taken from Ref. [92]).

4.3.2 The Simulation Data Flow

Figure 4.13 shows a simplified view of the processing stages in the simulation data flow [92]. Input for simulation comes from event generators after a particle filtering stage. The detailed description of the event generator can be found in Chapter 3.

Data objects representing Monte Carlo truth information from the generators are read by simulation. The input of simulation is a list of the four momenta of final-state particles. The response of the ATLAS detector is simulated by G4Atlas [93], which provides both a framework and the necessary functionality for running detector simulation in particle physics and other applications. The functionalities provided include optimized solutions for geometry description and navigation through the geometry, the propagation of particles through detectors, the description of materials, the modelling of physics processes (e.g. a huge effort has been invested in recent years into the development and improvement of hadronic-physics models) and visualization. The *hits* (which may carry information like position, energy deposit, identifier of the active element, etc.) are written out by G4Atlas as a record of the real interactions of particles in the detector.

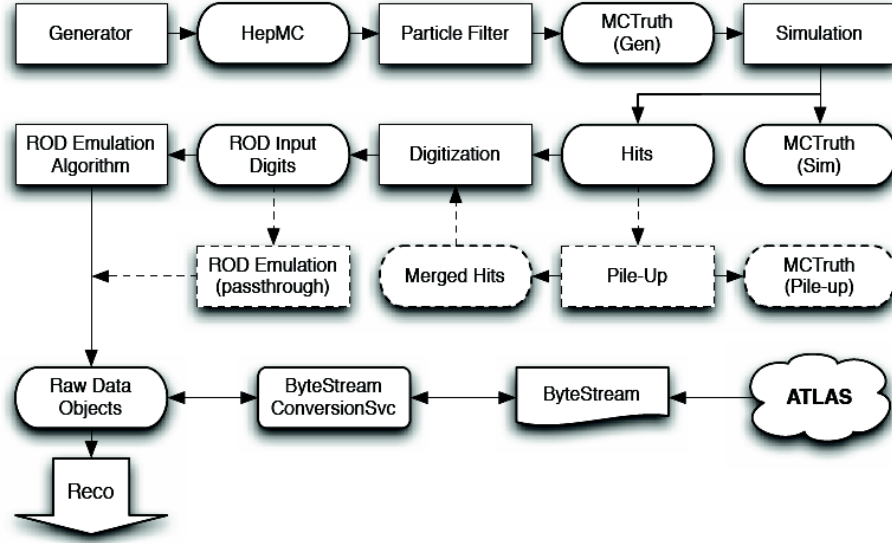


Figure 4.13: The simulation data flow (taken from Ref. [92]). Rectangles represent processing stages and rounded rectangles represent objects within the event data model. Pile-up and ROD emulation are optional processing stages.

Pile-up [94] occurs when the readout of a particle detector includes information from more than one primary proton-proton interaction. At the LHC design luminosity, these multiple interactions causes a major issue for ATLAS detector because the LHC beams will produce an average of 23 interactions each time they cross and the ATLAS detector is sensitive to tracks from more than one bunch crossing (the beams cross every 25 ns). The number of interactions that will occur when the beams cross follows a Poisson distribution. In addition to the *hits* of the physics event that triggers the detector readout, *hits* caused by many other interactions are recorded in the readout. Moreover, long living particles, known as cavern background, are observed in the muon system. To take in to account of the above effects, special minimum-bias files are produced, including the cavern background on top of the normal pile-up event.

The *hits* produced either directly by G4Atlas, or from the merging of pile-up events, need to be translated into the output actually produced by the ATLAS detectors. This stage is digitization. The propagation of charges (as in the tracking detectors and the liquid argon calorimeter) or light (as in tile calorimeter) into the active media has to be considered as well as the response of the readout electronics. Unlike the previous steps in the simulation chain, this is a very detector-specific task, and the expertise of people building and testing each of the sub-detectors is essential.

The final output of the digitization step are Raw Data Objects (RDOs) that should resemble the real detector data.

The RDOs service as the input to the reconstruction pipeline. The role of reconstruction is to derive from the stored raw data the relatively few particle parameters and auxiliary information necessary for physics analysis: photons, electrons, muons, tau-leptons, jets, missing transverse energy, primary vertex. Information from all detectors is combined so that the four-momentum reconstruction is optimal for the full momentum range, full rapidity range and any luminosity, and so that particles are identified with the least background, with the understanding that the optimum between efficiency and background rejection can be analysis-dependent. Event reconstruction including muon and EM clustering is given in Chapter 5. A novel algorithm developed for the FSR (Final State Radiation) photon reconstruction is given in Chapter 6.

Chapter 5

Event Reconstruction

This thesis aims to present a measurement of QED final state radiation in $Z \rightarrow \mu\mu$ decays in 7 TeV proton-proton collisions, which relies on reconstruction and identification of muons and photons. The strategy of the muon reconstruction and the electromagnetic (EM) cluster reconstruction in ATLAS is provided in this chapter.

5.1 Muon Reconstruction

Muons can penetrate through the calorimeters and reach the outermost muon spectrometer of ATLAS. The reconstruction and identification of muons is central for most ATLAS physics analyses. In accordance with the ATLAS general trigger scheme, there are three distinct levels of the muon trigger system. The muon spectrometer is designed to achieve good reconstruction efficiency and momentum resolution for muons, with energies ranging from a few GeV up to 1 TeV. The development of dedicated software ensures the high quality of muon identification. This section introduces the three levels of the muon trigger system, presents the different strategies of muon reconstruction and identification in ATLAS.

5.1.1 Muon Trigger

The Muon Trigger Vertical Slice is the full integrated chain of Trigger running with muon spectrometer data as input. The muon trigger in ATLAS includes three steps:

LVL1 Simulation, Multiple LVL2 selection algorithms and the TrigMoore EF selection algorithm, shown in Figure 5.1. The first is fully hardware based, while the remaining two are software based. Each stage is seeded by the previous one and all three levels are chained together [95][96].

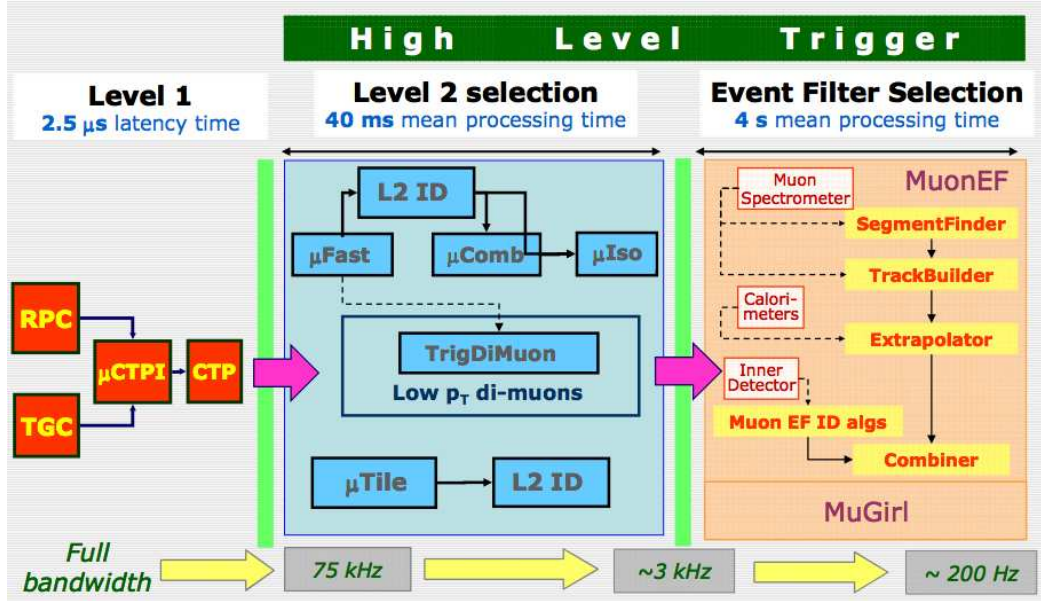


Figure 5.1: Muon ‘Vertical’ Slice diagram (taken from Ref. [96]).

The LVL1 trigger makes an initial selection, based on the information from Resistive Plate Chambers (RPC) in the barrel ($|\eta| < 1.05$) and Thin Gap Chamber (TGC) in the endcap ($1.05 < |\eta| < 2.4$). The patterns of hit strips (and wire groups from the TGCs) in the muon trigger chambers are received as input signal to the muon trigger system. The trigger algorithms then search for hit coincidences in different RPC or TGC detector layers within a region of interest (ROI), the size of which depends on the programmable p_T thresholds. To reduce the background, a valid trigger is generated only if the coincidences are satisfied for both η and φ projections. The information from all the sectors is combined in the Muon to Central Trigger Processor Interface (MuCTPI), including the position and p_T range of the track candidates. The MuCTPI calculates total multiplicity values of L1 muon candidates in six different p_T regions. Each L1 item corresponds to a required p_T threshold, the value of which is labeled in the threshold name (i.e MU0, MU10).

Muon High Level Trigger (HLT) takes charge of L2 and EF algorithms. It starts from the ROI defined by the L1 candidate and adds trigger decisions step by step,

each selection refining the previous one. Four algorithms are currently available for the muon L2 system:

- *MuFast* runs on full granularity data within the LVL1 ROIs. The momentum and track parameters are refined by fast fitting algorithm and Look-up-tables (LUTs) using MDT drift times.
- *MuComb* combines the reconstructed tracks in the inner detector with the tracks defined by muFast by a track combination algorithm. It provides further refinement in the measurement of the properties of the muon, rejecting background muons from K/π decays.
- *MuIsol* discriminates isolated and non-isolated muon candidates by checking energy depositions in the electromagnetic and hadronic calorimeters. The algorithm takes muons from muFast or muComb and defines two different concentric cones: an internal cone with energy deposited mostly by the muon itself, and an external cone with energy from detector noise, pile-up and jets.
- *MuTile* finds low p_T muons depositing energy in the Tile calorimeter, as a strategy for tagging muons. The algorithm starts from the outermost to the innermost calorimeter layers, searching a deposited energy compatible with a muon. A tagged muon is defined when muon compatible cells are found following a η projective pattern in all the three TileCal layers.

At the EF level the full event data are accessible. Currently, two main EF trigger algorithms exist in the trigger menu.

- *TrigMuonEF* refines the muons defined by L2 with wrappers of muon offline reconstruction tools starting from the muon spectrometer.
- *TrigMuGirl* reconstructs and tags muons starting from the inner detector.

5.1.2 Muon Reconstruction

Different strategies, corresponding to different methods to combine data from each subdetector, have been implemented to reconstruct and identify muon candidates:

- *Standalone Reconstruction Algorithms* find the tracks in the muon spectrometer and extrapolate them back to the interaction point.

- *Combined Reconstruction Algorithms* match the standalone muon candidates to the nearby inner detector tracks, combining the two independent subdetector tracks into a global one.
- *Segment Tagging Algorithms* extrapolate the inner detector tracks to the muon spectrometer and search for segments reconstructed in MS station.
- *Calorimeter Tagging Algorithms* extrapolate inner detector tracks through the calorimeters and scan for the energy deposition pattern associated to a minimum ionizing particle (MIP) in the calorimeter cells.

Currently in ATLAS, more than one algorithm is provided for each of these strategies. Two main families used in the physics analysis are StacoMuonCollection [97] and MuidMuonCollection [98] (Table 5.1), each containing the muons found by three different algorithms: standalone, combined and segment tagging algorithms. Another separate family is CaloMuonCollection, based on the calorimeter tagging algorithms.

	StacoMuonCollection	MuidMuonCollection
Standalone algorithms	Muonboy	MOORE/Muid Standalone
Combined algorithms	STACO	Muid Combined
Tagging algorithms	MuTag	MuGirl/MuTagIMO

Table 5.1: The two main families of muon collections and their corresponding algorithms.

Standalone Muon Reconstruction

The standalone reconstruction algorithms aim to determine the momentum and trajectories of the muons passing through the spectrometer. The track reconstruction is more challenging in the muon spectrometer than in the inner detector. Firstly, the inert material in the toroids and support system needs to be well estimated. Secondly, the large distances in between the three MS stations can lead to a large extrapolation errors. Thirdly, the large inhomogeneity of the toroidal magnetic field makes the fitting procedure difficult especially near the coils.

In the *STACO* algorithm family, the standalone reconstruction is done by *Muonboy*. The strategy of the pattern recognition is performed in several steps. *Muonboy* starts building regions of activity (ROA) of $\Delta\eta \times \Delta\varphi = 0.4 \times 0.4$ according

to the trigger signals in the RPCs and TGCs. The regions are simple cones pointing towards the interaction point and are centered where at least one RPC/TGC hit exists in both coordinates. The drift circles constructed in the drift tubes (MDT) are defined as signal. The arrival time of the signal can be interpreted as a drift-radius. Tangents are constructed on the drift circles, linking two hits into a track segment. All the muon chambers intersecting with the ROAs are taken in the segment building. The two-coordinate (η, φ) pairs of the generated track segments are pointed back towards the interaction vertex to reject fakes. The selected track candidates are then extrapolated through the whole muon spectrometer to match the remaining recorded hits, taking into account multiple scattering and energy loss. *Muonboy* uses its own energy loss and multiple scattering parametrisation.

In the Muid algorithm family, *MOORE* takes charge of the standalone track reconstruction. Unlike *Muonboy*, it starts with the CSC segment making. The hits in the CSC are produced by applying the appropriate clustering methods to the digitised measurements. The charge deposition on the strips of each chamber is taken to build the cluster. Separated η and φ clusters from each of the four layers are fitted and combined, producing two-dimensional segments pointing a direction in space. Those 2D segments are then combined into full 3D segments. The η hits in the MDTs are associated to the segments by a χ^2 minimisation procedure. The hits found in the trigger stations are combined into segments as well. Afterwards, a segment selection is applied to remove ambiguities (i.e hits shared by more than one segment). The track candidates are built segment by segment using a global χ^2 fit. Once the tracks are obtained, *MuidStandalone* extrapolates the *MOORE* track to the perigee and uses a vertex constraint to determine the track parameters at the vertex. *Muid* has its own parametrisation of the energy loss using a set of scattering planes in the calorimeters. If it is a well isolated track with measured energy larger than the most probable value (MPV) of the parametrisation, *Muid* uses the energy measured in the calorimeters [99].

The performance of the standalone algorithms is mainly affected by the detector coverage. There is a significant efficiency loss at the gaps in the muon spectrometer ($|\eta| < 0.1$, $1.2 < |\eta| < 1.7$) as shown in Figure 4.8.

Combined Muon Reconstruction

Both combined muon reconstruction algorithms, *STACO* and *MuidCombined*, combine an inner detector track with a muon spectrometer track.

The principle of the *STACO* algorithm is to perform a statistical combination of two independent track parameter vectors by means of their covariance matrices. The combined track parameter vector T is defined as:

$$T = (C_{ID}^{-1} + C_{MS}^{-1})^{-1}(C_{ID}^{-1}T_{ID} + C_{MS}^{-1}T_{MS}) \quad (5.1)$$

where C_{ID} and C_{MS} are the covariance matrices of the inner detector and muon spectrometer, and T_{ID} and T_{MS} are the parameter vectors of the inner detector and muon spectrometer, respectively. The corresponding χ^2_{match} is defined as the difference between both track parameter vectors weighted by their combined covariance matrix:

$$\chi^2_{match} = (T_{MS} - T_{ID})^T(C_{ID} + C_{MS})^{-1}(T_{MS} - T_{ID}) \quad (5.2)$$

In the first step, the tracks from both track containers are filtered on the basis of the quality criteria. Then the algorithm searches for pairs of ID and MS tracks requiring a crude η and φ matching and a χ^2 matching. A set of other cuts could be applied, i.e. the probability of the hypothesis that a given pair of tracks have the same charge, a comparison of the matching χ^2 at beam and at the entrance of the Muon Spectrometer, etc. The surviving pairs with the lowest matching χ^2 are kept as the origin of muon candidates. Then, the corresponding tracks are removed from the input track containers. The procedure is looped until no more combinations are available.

The *MuidCombined* algorithm starts with the inner detector tracks, iteratively adding hits from the muon spectrometer tracks. The *MOORE* tracks are extrapolated back to the interaction point. The multiple scattering, the energy loss in the calorimeter layer and the bending effect of the magnetic field are taken into account. Five additional parameters, two scatters (with η and φ information) and an energy loss parameter are provided to describe the interaction with the calorimeters. The ID and MS tracks are matched using a χ^2 with five degrees of freedom. The track combination is accepted only if the χ^2 is below a given value. Tracks can be refitted when no match is found.

Tagged Muon Reconstruction

The muon tagging algorithms identify muons by associating an inner detector track with a segment in the muon spectrometer on the basis of a “good” matching.

MuTag performs a χ^2 match of the MS segment and the ID track. It aims to complement the *STACO* muon collection, only considering inner detector tracks

and muon spectrometer track segments that were not used by *Muonboy* or *STACO*. The main motivation is to increase the efficiency of muon identification at low pt and in some crack regions. The low pt muons emerge from the calorimeters with very low momenta, leading to a very chaotic and hardly reconstructed trajectory in the muon spectrometer. Their passages can only be identified before they are significantly bent by the toroidal field. *MuTag* therefore extrapolates the ID track to match a track segment in the innermost muon stations and some middle regions where there is a station overlap. On the other hand, in some regions the muon spectrometer is poorly equipped, i.e. the region around $|\eta| \sim 1.1$ where some chambers are missing or the $|\eta| \sim 0$ region due to passage of services. In these regions, it is hard or even impossible to reconstruct a muon track. In this case the tagging algorithm can help as well.

MuGirl applies an artificial neural network to define a discriminant. It performs a search for segments and tracks in the muon spectrometer using an inner detector track as seed. If the full track refit is successful a Combined Muon is made. If the track refit is not successful a Tagged Muon is made. Additionally, *MuGirl* allows more weight to be added to tracks that also get tagged by the calorimeter based identification algorithms. *MuTagIMO* identifies muons by associating an inner detector track to Inner-Middle-Outer Moore segments. It performs a loose matching on the η and φ of the track and segment. The algorithm is originally developed using ATLAS cosmic ray muon data.

5.2 EM Cluster Reconstruction

When an electron/photon penetrates the ATLAS LAr electromagnetic calorimeter, most of the energy is deposited near the shower axis, developing a compact electromagnetic (EM) shower. To reconstruct the energy of the electron/photon, the energies deposited in the calorimeter cells are added together. This collection of cells is defined as a “cluster”. In ATLAS, there are two standard clustering algorithms, the topological clustering algorithm and the sliding-window clustering algorithm.

The author of this thesis has developed a special clustering algorithm, which combines the creation of fixed-size clusters with the excellent capability of the topological cell clustering in identifying low-energy deposition patterns in the EM calorimeter. The original idea and the development of this new strategy as well as the further applications using this new method are discussed in the Chapters 6. In this section, the two standard clustering algorithms are introduced and the EM calibrations are discussed.

5.2.1 Topological clustering

The idea of the topological clustering [100][101] is to accumulate cells in clusters according to their neighbor relations. The resulting clusters have a non-fixed size and a variable number of cells. The cells can be searched in the same layer of the calorimeter (all2D), in the same calorimeter (all3D) or across all calorimeters (super3D). The cell selection is based on three σ_{noise} dependent thresholds, defined as:

- Seed Threshold: The $|energy|/\sigma$ of the seeded cells are required to be above a large (seed) threshold.
- Neighbor Threshold: The $|energy|/\sigma$ of the neighboring cells around the seeds are required to be above a medium (neighbor) threshold.
- Cell Thresholds: The $|energy|/\sigma$ of the rest of the adjacent cells are required to be above a low threshold.

The σ_{noise} is defined by default to be the quadratic sum of the electronics noise and the pile-up noise. Topological clusters start from the seeded cells, grow by iteratively adding neighboring cells, and finish by including all the adjacent cells passing the Cell Thresholds.

Typically in ATLAS, especially in the endcap and forward regions, clusters could spread into a large area if sufficient energy is present between particles. In the case of overlapping showers, individual particles/clusters may be separable if they are far apart enough to form local maxima in the calorimeter. The local maximum cells must satisfy three requirements: (i) $E > 500$ MeV; (ii) energy greater than that of any neighboring cell; (iii) number of neighboring cells above a threshold (4 by default). More than one local maximum in one cluster drives the demand for a cluster splitter. Cells at the boundary of two split clusters can be shared and stored into a shared cell list. The shared cells are later assigned to the two adjoining clusters with the weights, with a rough estimate of the probability ratio for a given cell belonging to either cluster.

The topological clustering is efficient at suppressing noise in the clusters with large numbers of cells, and is excellent in identifying low-energy deposition patterns in the calorimeter. It is used for the forward ($|\eta| > 2.5$) electron reconstruction, and more widely used for the jet and missing transverse energy reconstruction.

5.2.2 Sliding-Window clustering

The sliding-window clustering [100][102] is responsible for the building of fixed size clusters. In ATLAS, two types of sliding-window clusters are built: electromagnetic one, for the electron and photon (“egamma”) identification; and combined one, with information from EM and hadronic calorimeter for the jet finding. The description of the egamma sliding-window clusters is presented here. The algorithm proceeds in three steps: tower building, pre-cluster (seed) finding, and cluster filling.

Tower Building: The $\eta - \varphi$ space of the EM calorimeter is divided into a grid of $N_\eta \times N_\varphi (= 200 \times 256)$ elements, each with a size of $\Delta\eta \times \Delta\varphi (= 0.025 \times 0.025)$. For each element, the energy of all cells through the longitudinal layers is summed as the “tower” energy. Towers are stored for the later cluster building.

Pre-Cluster (Seed) Finding: A fixed size window $N_\eta^{window} \times N_\varphi^{window} (= 5 \times 5)$, in units of tower size, is slid to each node of the tower grid. The transverse energy for each window is defined as the sum of the transverse energy of the towers inside the window. A pre-cluster is formed for a window with a transverse energy above a threshold $E_T^{thresh} (= 3\text{GeV})$. The window size and the E_T^{thresh} are optimised to obtain the highest pre-cluster search efficiency and the lowest background noise. The position of the pre-cluster is calculated as the barycenters of the energy-weighted η and φ of all cells within another fixed size window around the center of the sliding-window. To be less sensitive to noise, the window for the position calculation usually has a smaller size $N_\eta^{pos} \times N_\varphi^{pos} (= 3 \times 3)$. In case of duplicate pre-clusters, if two pre-clusters have a distance smaller than a threshold distance $\Delta\eta_{dupl} \times \Delta\varphi_{dupl} (= 2 \times 2)$, the one with the largest E_T is kept, and the other is removed.

EM Cluster Filling: Final EM cluster filling is applied with a rectangle of size $N_\eta^{cluster} \times N_\varphi^{cluster}$ centered on a layer-dependent seed position. The process is performed step by step: first on the middle layer, later on the strip, finally on the pre-sample and the back. The barycenter position of the pre-cluster is used as the seed position for the middle layer. The barycenter position of the middle layer is later served as the seed position for the strips. Finally, the presample and the back layers are processed, using respectively the barycenters of the strip and the middle layer as the seed position. The choice of the window size is a compromise between electronic noise and shower energy containment. The typical sizes used by the egamma cluster collections are 3×5 , 3×7 and 5×5 , listed in Table 5.2.

Particle Type	Barrel	Endcap
Electron	3×7	5×5
Converted photon	3×7	5×5
Unconverted photon	3×5	5×5

Table 5.2: Cluster size for different egamma particle types in the barrel and endcap region of the EM calorimeter (taken from Ref. [100]).

In the barrel region, electrons have wider showers than photons because electrons interact more with upstream material. Also, the magnetic field curves the trajectory of the charged particle in the φ direction, which requires an increased φ size for electrons in order to contain most of the energy. Converted photons have a similar behavior due to the pair production. In the endcap region, the effect of the magnetic field is smaller, thus the cluster size is the same for all egamma particles.

The sliding-window clustering is an efficient tool for precisely reconstructing electromagnetic showers. The fact that the cluster size is fixed allows for a very precise cluster energy calibration.

5.2.3 EM Calibration

The calibration of electrons and photons can be divided into three steps: electronic calibration, Monte-Carlo based calibration, and in-situ calibration [103][104].

Electronic calibration

The raw signal extracted from each cell in ADC counts is converted into a deposited energy using the electronic calibration of the EM calorimeter. The cell energy is reconstructed from the measured cell signal using:

$$E_{cell}^{vis} = \frac{1}{f_{I/E}} F_{gain} \sum_{sample=1,N} OF_{sample,gain} (S_{sample} - P_{gain}), \quad (5.3)$$

where S_{sample} is the signal measured in ADC counts in N time slices, P_{gain} is the pedestal for each gain and $OF_{sample,gain}$ are the optimal filtering (OF) coefficients derived from the shape of the physics pulse and the noise. The function F_{gain} converts

for each gain ADC counts to currents in μA . The factor $f_{I/E}$ takes into account the conversion from the measured current to the energy. Details on the calibration of electronics can be found in Ref. [105].

Monte-Carlo based calibration

Electrons/photons deposit their energy in the EM calorimeter through electromagnetic interactions. Most of the energy is deposited in the presampler and the three compartments of the calorimeter. However, a fraction of energy is absorbed in the upstream material, i.e. the material before the cryostat, the cryostat, and the inactive material between the presampler and the strips. Also, a small amount of energy escapes due to the longitudinal and lateral leakage of the shower outside the cluster (Figure 5.2). To recover the energy loss and achieve good energy resolution and linearity, two Monte-Carlo based calibration methods are used in the current ATLAS reconstruction: the “longitudinal weight method” with energy independent longitudinal weights, and the “calibration hits method” using energy dependent weights. The special EM clustering used in the analysis of this thesis (see Chapter 6) is calibrated using the “longitudinal weight method”.

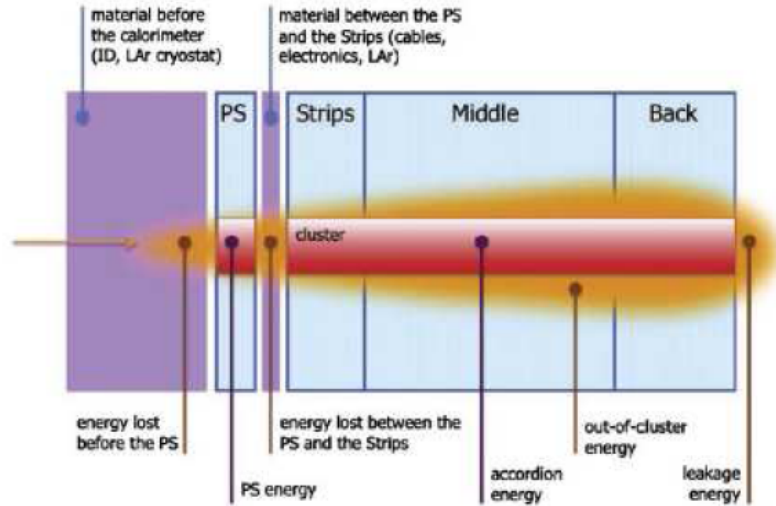


Figure 5.2: Schematic view of an electromagnetic shower developing in the ATLAS LAr calorimeter (taken from Ref. [106]).

The longitudinal weights method has been tested with data in an ATLAS combined test beam for electrons with energy above 10 GeV [107]. The idea is to extract the longitudinal weights for electrons/photons that minimize the energy resolution.

The reconstructed energy is calculated as a linearly weighted sum of the layer responses:

$$E = s(b + W_0 E_{PS} + E_1 + E_2 + W_3 E_3) \quad (5.4)$$

where E_{PS} and $E_{1,2,3}$ are the cluster energies in the presampler and the three layers of the EM calorimeter. The offset term b corrects for upstream energy losses for which the corresponding electrons do not reach the presampler. The parameters s , b , W_0 and W_3 are calculated by minimizing $\chi^2 = (E_{true} - E_{rec})^2 / \sigma^2(E_{true})$ using Monte Carlo, where $\sigma(E_{true})$ is the parametrisation of the expected calorimeter energy resolution and E_{true} is the true energy of the particle at generator level in the Monte Carlo.

A dedicated set of coefficients has been extracted using low energy photons coming only from π^0 's in the minimum-bias simulation sample with a binning of 0.025 along $|\eta|$ (assuming φ symmetry) [108]. Only photons in the core of the π^0 mass distribution are used in each η bin. The computed weighteds is shown in Figure 5.3 as a function of $|\eta|$:

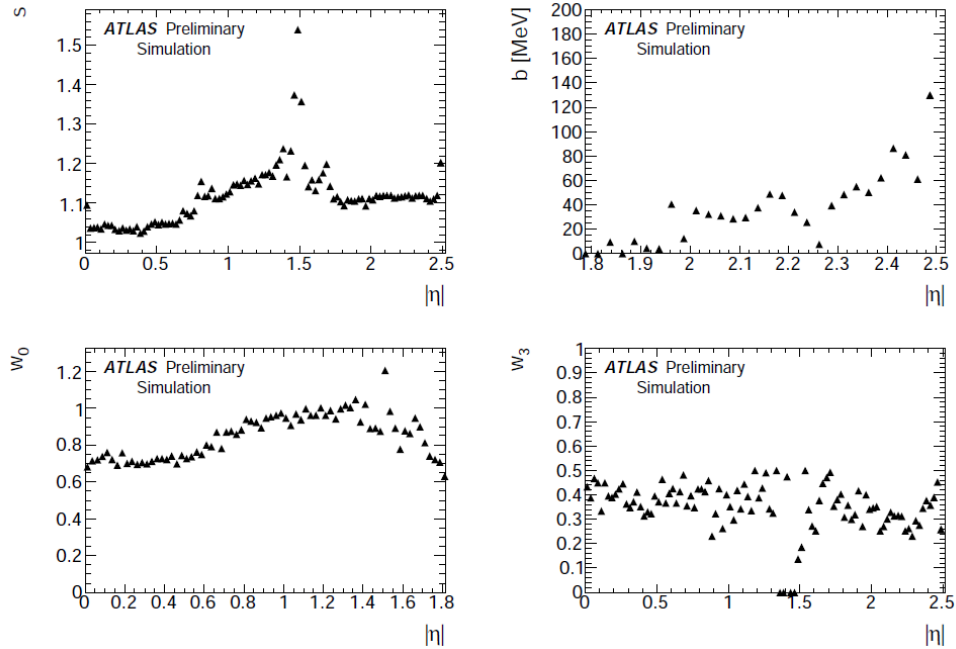


Figure 5.3: The longitudinal weights s , b , W_0 and W_3 as a function of $|\eta|$ (taken from Ref. [108]).

- The scale parameter s varies by 10% along $|\eta|$ and increases with the amount of upstream material in the barrel region.
- The offset parameter b corrects for upstream energy loss for electrons/photons that have not reached the presampler. It is found to be negligible for $|\eta| < 1.8$. For larger $|\eta|$, where there is no presampler, the energy loss in front of calorimeter is corrected on average by this coefficient.
- The W_0 coefficient varies between 0.7 and 1 for $|\eta| < 1.8$. For $|\eta| > 1.8$ where there is no presampler, it is set to 0.
- The W_3 coefficient takes into account the longitudinal leakage. The values are flat in $|\eta|$ and are lower than 1 due to the fact that the significant noise contribution to the back layer.

The energy uniformity for photons coming from π^0 decays using the minimum-bias simulation sample, after dedicated selections, is shown in Figure 5.4 before and after calibration. The response after calibration improves from 10% (before) to 2% and is flat within a few percent along $|\eta|$.

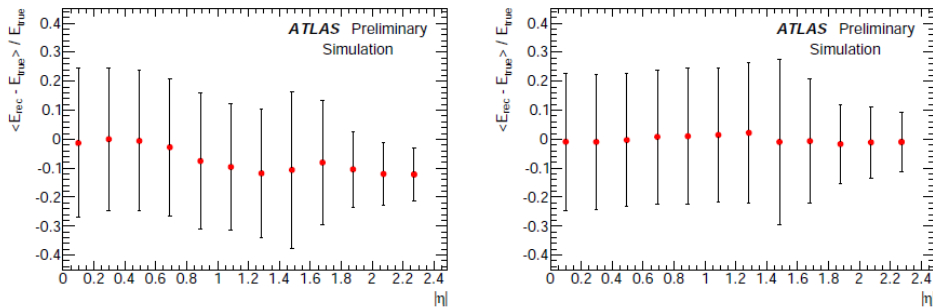


Figure 5.4: Mean fractional-energy deviation from truth (points) and energy resolution (error bars) as a function of $|\eta|$ before (left) and after (right) calibration (taken from Ref. [108]).

In-situ calibration

The recorded ATLAS physics events can be used to determine the absolute energy scale and intercalibrate the different regions of calorimeters. Before the first collisions, the electromagnetic calorimeter energy scale has been derived from test beam results

with an uncertainty of 3% in the central region ($|\eta| < 2.47$) and 5% in the forward region ($2.5 < |\eta| < 4.9$). The uncertainty is mainly due to the imperfect knowledge of the temperature of the LAr during the test beam campaigns. The first test of energy scale, using $\pi^0 \rightarrow \gamma\gamma$ and $\eta \rightarrow \gamma\gamma$ events, has found that the response uniformity along η is of the order of 2% from the ratio of data to MC [108].

The precise knowledge of the Z invariant mass from LEP can be used to measure the electron energy scale with a better accuracy. The J/ψ invariant mass allows the validation of the linearity of the EM calorimeter since the electron energy spectrum is much lower than for the Z case. Another strategy is to investigate the ratio E/p for electrons, e.g. the ratio of the energy measured by the EM calorimeter and the momentum measured by the inner detector. The in-situ calibration can also be used to intercalibrate the different regions of the calorimeters, e.g. using electron pairs from Z boson decays. The first electron in-situ calibration, based on $Z \rightarrow ee$ events from data collected in the year 2010, has found that the energy scale corrections are within $\pm 1\%$ in the barrel and within $\pm 5\%$ in the forward regions. The method was validated using other physics events, $J/\psi \rightarrow ee$ and $W \rightarrow e\nu$, leading to an uncertainty on the scale varying from -1.5% to 2% depending on η [103][104].

Chapter 6

Reconstruction of QED final state radiation photons in $Z \rightarrow \mu\mu$ decays in 7 TeV pp collisions

6.1 Introduction

The measurement of the QED Final State Photon Radiation (FSR) from Z and W boson leptonic decays is necessary for controlling QED radiative corrections in W/Z boson cross-section predictions down to relatively very low photon energy. Experimental control of QED radiation in W boson production and decay is also important for reducing the systematic uncertainties in the measurement of the W mass and width. Notably, reconstruction of FSR photons in Higgs $\rightarrow ZZ$ and Z' decays may increase the discovery potential of these searches.

In the process of muon pair production, the shape of the Z resonance peak obtained from measuring the invariant mass distribution of the $\mu^+\mu^-$ pair is significantly affected by the final state radiation, due to the fact that events belonging to the Z pole are shifted to the low mass region [45]. The FSR-induced distortion effects can be sizeable depending on the definition of the line shape [2]. In the case of resonant pair production, distortion effects can be enhanced; in the search for a Higgs $\rightarrow ZZ$ at high masses (>180 GeV) long tails in the 4-lepton invariant mass can be observed for muons in the final state. The deterioration of the 4-lepton resolution leads to a reduced sensitivity to the Higgs signal.

Instead of treating the FSR effect as a radiative correction, one actually wants to reconstruct and measure those missing FSR photons, especially for the Z resonance region, and improve the Z invariant mass reconstruction by including them in the calculations. In ATLAS, QED FSR photons emitted from the $Z \rightarrow \mu\mu$ lines can be reconstructed with the LAr calorimeter: one searches for EM clusters within a narrow cone about the axis defined by the muon momentum direction at the interaction point (neutral line). The longitudinal segmentation of the LAr calorimeter, which is unique to ATLAS, can be exploited to reduce fake photon clusters produced by muon energy loss in the calorimeter. This is achieved by using as a discriminant the fraction f_1 of the cluster energy in the front segment of the calorimeter (the strips). Low energy photons ($E < 5$ GeV) leave most of their energy in the strips and they cannot penetrate deep in the calorimeter. On the other hand, muons lose energy uniformly while propagating in the calorimeter; since the strip segment of the calorimeter consists about 1/6 of the total calorimetric length, muons produce clusters with small f_1 . An advantage of this analysis is the possibility of verifying the FSR signal purity by comparing the $Z \rightarrow \mu\mu\gamma$ invariant mass in the data with that from Monte Carlo simulation (MC).

This chapter presents reconstruction performance studies of the $Z \rightarrow \mu\mu\gamma$ decay, a measurement of the $Z \rightarrow \mu\mu\gamma$ yield as a function of energy, transverse energy and pseudorapidity, as well as studies of the improvement of the reconstructed Z invariant mass. The analysis is based on an integrated luminosity of 164 pb^{-1} . Section 6.2 presents the data and MC samples used. Section 6.3 describes the event selection. The performance of the FSR photon reconstruction and the special topo-seeded clustering used in the analysis are discussed in Section 6.4. The final yields of $Z \rightarrow \mu\mu\gamma$ events and the measurement of $Z \rightarrow \mu\mu\gamma$ fiducial cross-section are presented in Section 6.5. In Section 6.6 the systematic uncertainties are discussed. The improvements of the Z-boson mass resolution and scale are presented in Section 6.7. Finally, a study of the ATLAS pile-up simulation performance using photon candidates from data reconstructed with the special topo-seeded clustering can be found in Section 6.8.

6.2 Data and Monte Carlo Samples

In this section the data and MC samples used in the analysis are summarized. The generator level FSR photon kinematic distributions are presented.

6.2.1 Data Samples

The analysis is based on part of the proton-proton collision data at $\sqrt{s} = 7$ TeV collected in 2011, within data-taking periods B2 and D1-D7. A Good Run List (GRL) criterion is applied to select luminosity blocks that satisfy the ATLAS data quality criteria. The Data Quality shifters are required to certify that data are usable for analysis, based on a comparison of monitoring histograms produced with data to standard reference histograms [109]. Application of basic beam, detector, and data-quality requirements results in a total integrated luminosity of 164 pb^{-1} .

6.2.2 Simulated Event Samples

The Monte Carlo samples for signal and background are generated at $\sqrt{s} = 7$ TeV with the PYTHIA [57] and POWHEG [69] event generators. The dedicated photon radiation package PHOTOS [66] is used as a PYTHIA generator afterburner to simulate the effects of QED radiative corrections in decays of resonances. Passage of particles through the ATLAS detector is modelled using GEANT4 [110]. The MRSTLO* [111] parton distribution functions are used for the PYTHIA samples. The effect of multiple pp interactions per bunch crossing (“pile-up”) is modelled by overlaying simulated minimum bias events over the original hard-scattering event. MC events are then reweighted to make sure the reconstructed primary vertex distribution agrees with the data.

Table 6.1 summarizes the simulated event samples used in this analysis and their properties. The W and Z cross-sections are normalized to NNLO cross-sections as provided by the FEWZ [40] program. The associated uncertainties have been derived from the choice of PDF, from factorization and renormalization scale dependence and from the strong coupling constant α_s [112]. An uncertainty of $(+7, -10)\%$ is taken for the $t\bar{t}$ cross-section, calculated at $m_t = 172.5 \text{ GeV}$ [113].

6.2.3 Photon Final State Radiation at generator level

The simulation of the effects of QED radiative corrections in Z decays is performed using PHOTOS [66] which is used as a PYTHIA [57] Monte Carlo generator afterburner. PHOTOS is executed in the exponentiated mode, leading to the multi-photon emission, taking into account γ^* interference in the $Z \rightarrow \mu\mu$ decay. PHOTOS restricts the minimal E_γ^{min}/M ratio (M being the mass of the decaying particle, E_γ^{min} the

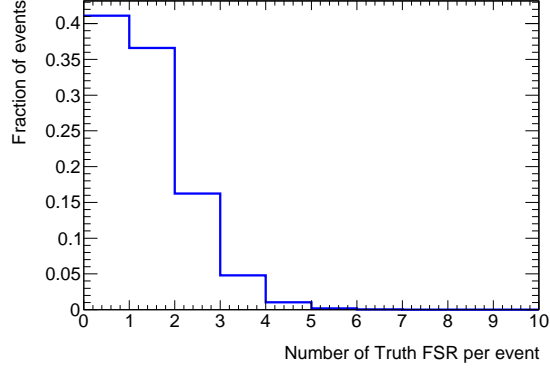
Physics Process	Dataset	Generator	$\sigma \cdot \text{BR}[\text{nb}]$	
$Z \rightarrow \mu\mu (m_{\mu\mu} > 60\text{GeV})$	106047	PYTHIA	0.99 ± 0.05	NNLO
$Z \rightarrow \tau\tau (m_{\tau\tau} > 60\text{GeV})$	106022	PYTHIA	0.99 ± 0.05	NNLO
$W \rightarrow \mu\nu$	106044	PYTHIA	10.46 ± 0.52	NNLO
$t\bar{t} (m_t = 172.5\text{GeV})$	105861	POWHEG,PYTHIA	$0.165^{+0.011}_{-0.016}$	$\approx \text{NNLO}$

Table 6.1: Summary of Monte Carlo samples and generators used in the simulation. The W and Z cross-sections are normalized to NNLO cross-sections as provided by the FEWZ [40] program. The $t\bar{t}$ cross-section normalization is at an approximate NNLO cross-section using the CTEQ66 PDF set.

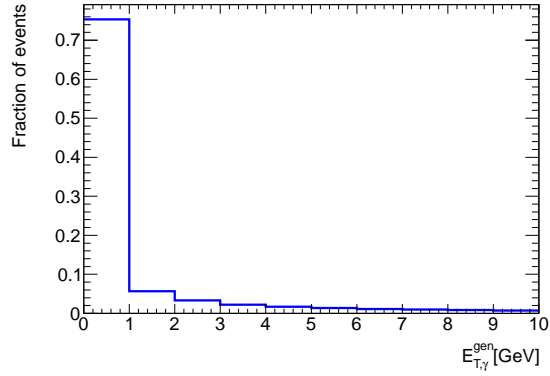
minimal energy of the generated photons). The value of the infrared cut-off parameter E_γ^{min}/M is set to $\sim 10^{-7}$ in the CMS frame (center-of-mass system: an inertial frame in which the center of mass is at rest.) of the decaying Z boson. Using this simulation the generator level predicted fraction of $Z \rightarrow \mu\mu$ events with zero, one or more FSR photons at generator level is obtained. This is shown in Figure 6.1(a). The predicted fraction of events as a function of the leading FSR photon transverse energy and the fraction of events as a function of $\Delta R (= \sqrt{\Delta\eta^2 + \Delta\phi^2})$ between the leading FSR photon and the radiating muon at generator level, are shown in Figures 6.1(b) and 6.1(c).

Table 6.2 summarizes the fractions of FSR events with respect to the inclusive $Z \rightarrow \mu\mu$ events at generator level. A 13% of the inclusive $Z \rightarrow \mu\mu$ events are expected to have at least one FSR photon with $E_{T,\gamma}$ greater than 1.3 GeV. For half of these events, the photons are radiated within a 0.15 cone around the closest muon. Only 7% of the inclusive $Z \rightarrow \mu\mu$ events are expected to have at least one radiated photon with $E_{T,\gamma} > 1.3$ GeV and $\Delta R_{\gamma,\mu} < 0.15$. As shown in the last row of Table 6.2, the probability for both muons to have an accompanying photon with $E_{T,\gamma} > 1.3$ GeV and $\Delta R_{\gamma,\mu} < 0.15$, is at the 0.1% level.

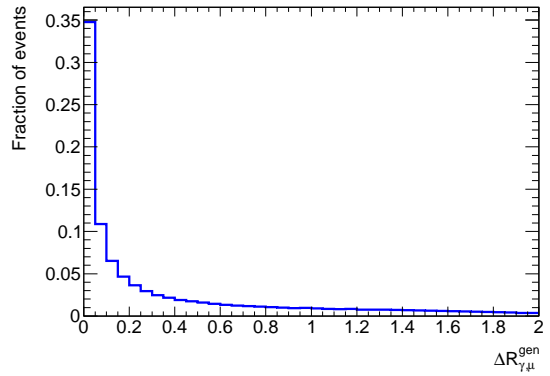
The aim of this analysis is to reconstruct and measure the yield of $Z \rightarrow \mu\mu\gamma$ events with at least one hard FSR photon ($E_T > 1.3$ GeV) radiated collinearly to the emitting muon ($\Delta R < 0.15$). At reconstruction level the ΔR is defined as the radius of the cone around the muon neutral line.



(a)



(b)



(c)

Figure 6.1: (a) Fraction of $Z \rightarrow \mu\mu$ events with zero, one or more FSR photons, (b) fraction of events as a function of the leading FSR photon transverse energy and (c) fraction of events as a function of $\Delta R(=\sqrt{\Delta\eta^2 + \Delta\varphi^2})$ between the leading FSR photon and the radiating muon at generator level. Note that in the generator PHOTOS the value of the infrared cut-off parameter E_γ^{min}/M is set to $\sim 10^{-7}$ in the CMS frame of the decaying Z boson.

Events at Generator-Level	N_{events}	Rel. Fraction[%]	Abs. Fraction[%]
$Z \rightarrow \mu\mu$	500437	100.00	100.00
$Z \rightarrow \mu\mu\gamma$	294678	58.88	58.88
$Z \rightarrow \mu\mu\gamma$: at least one γ with $E_{T,\gamma} > 1.3$ GeV	66376	22.52	13.26
$Z \rightarrow \mu\mu\gamma$: at least one γ with $E_{T,\gamma} > 1.3$ GeV, $\Delta R_{\gamma,\mu} < 0.15$	34739	52.34	6.94
$Z \rightarrow \mu\mu\gamma$: both μ have γ with $E_{T,\gamma} > 1.3$ GeV, $\Delta R_{\gamma,\mu} < 0.15$	619	1.78	0.12

Table 6.2: Fractions of $Z \rightarrow \mu\mu$ events with at least one radiated photon with respect to the inclusive $Z \rightarrow \mu\mu$ events at generator level. A 13% of the inclusive $Z \rightarrow \mu\mu$ events are expected to have at least one FSR photon with $E_{T,\gamma}$ greater than 1.3 GeV. For half of these events, the photons are radiated within a 0.15 cone around the emitting muon. Only 7% of the inclusive $Z \rightarrow \mu\mu$ events are expected to have at least one radiated photon with $E_{T,\gamma} > 1.3$ GeV and $\Delta R_{\gamma,\mu} < 0.15$. As shown in the last row, the probability for both muons to have radiated a photon with $E_{T,\gamma} > 1.3$ GeV and $\Delta R_{\gamma,\mu} < 0.15$, is at the 0.1% level. The statistic errors are negligible.

6.3 Event Selection

The goal of the event selection is to obtain a high purity, high efficiency sample of $Z \rightarrow \mu\mu\gamma$ events. The selection consists of (i) a preselection of $Z \rightarrow \mu\mu$ candidate events, and (ii) a final selection where at least one candidate radiated photon is reconstructed.

6.3.1 Preselection: $Z \rightarrow \mu\mu$ candidates

The preselection relies on an efficient $Z \rightarrow \mu\mu$ event selection, summarized in Table 6.3. The procedure is identical to the ATLAS Standard Model W/Z selection. Events are triggered with a single muon trigger with an Event Filter (EF) threshold of transverse momentum $p_T=18$ GeV, using the *TrigMuGirl* algorithm [114]. Events passing the trigger should have at least one reconstructed primary vertex with at least three ID tracks. Muon objects are required to be inner detector and muon spectrometer combined muons. To ensure the best reconstruction of the associated inner detector (ID) tracks, additional quality criteria are applied to the ID tracks based on

the Muon Combined Performance (MCP) Working Group [115]:

- at least one pixel b-layer hit on the muon track with the exception of extrapolated muon tracks traversing an uninstrumented or dead areas of the b-layer.
- sum of pixel hits and crossed dead pixel sensors > 1 .
- sum of SCT hits and crossed dead SCT sensors ≥ 6 .
- sum of pixel holes and SCT holes < 2 .
- the TRT hit requirements: (i) when $|\eta| < 1.9$: Hits+Outliers > 5 and Outliers/(Hits+Outliers) < 0.9 ; (ii) when $|\eta| \geq 1.9$: if (Hits+Outliers) > 5 , Outliers/(Hits+Outliers) < 0.9 .

Furthermore, to suppress the cosmic background, the Z coordinate of the muon's maximum approach to the beam axis is required to be compatible with the corresponding coordinate of the primary vertex within 10 mm ($|z_0 - z_{vtx}| < 10$ mm).

Events passing the above selections are then required to have a pair of oppositely charged muons, both with p_T greater than 20 GeV and $|\eta| < 2.4$. Z decay muons will in general be isolated, while muons from many of the background process are non-isolated. Thus, a track-based isolation criterion is required: the p_T of ID tracks are summed within a cone $\Delta R < 0.2$ around the muon and a cut on the normalized sum p_T inside the cone is applied as $\sum p_T^{ID}/p_T < 0.1$. Finally, the dimuon invariant mass must be in the range of 66-116 GeV.

Cut Name	Cut Value
Trigger	EF_mu18_MG
Primary vertex	$N_{vtx} \geq 1$ with $N_{tracks} \geq 3$
Muon selection	Combined muons MCP quality cuts $ z_0 - z_{vtx} < 10$ mm
Dimuon cut	$p_T > 20$ GeV, $ \eta < 2.4$
Charge	$q1 \times q2 < 0$
ID isolation	$\sum p_T^{ID}/p_T < 0.1$
Z Invariant Mass	$66 < M_{\mu\mu} < 116$ GeV

Table 6.3: Summary of event preselection criteria.

6.3.2 Final selection: $Z \rightarrow \mu\mu\gamma$ candidates

Events passing preselection contain two high energy muons which serve as candidate sources of photon radiation. For each candidate event, an initial search for electromagnetic (EM) clusters is performed within a chosen cone $\Delta R = \sqrt{\Delta\eta^2 + \Delta\varphi^2} < 0.3$ about the axis defined by the muon momentum direction at the interaction point (neutral line). In this analysis a special clustering is employed for the photon reconstruction because of its high efficiency in identifying low-energy EM deposition patterns in the EM calorimeter. A search for a cluster seed cell is performed using the so-called ATLAS electromagnetic topological clusters (EM topo-seeded clustering). After a seed cell is found, a fixed-size cluster is built around this seed. A more detailed description of this EM topo-seeded clustering can be found in Section 6.4.

Since up to this point the low energy EM clusters found have no additional selection criteria, a significant background contribution is expected. Three main selection cuts are applied directly to these reconstructed FSR photon candidates with the goal of reducing the background for a high efficiency. These cuts are listed in Table 6.4. A reconstructed FSR photon is required to have a minimum transverse energy of 1.3 GeV. Two additional cuts $f_1 = E_{\text{strips}}/E_{\text{cluster}} > 0.15$ and $\Delta R_{\text{cluster},\mu} < 0.15$ are applied to further reduce the background. As already discussed in the introduction, the longitudinal shower shape discriminant $f_1 = E_{\text{strips}}/E_{\text{cluster}}$, is the fraction of energy reconstructed in the first sampling of the EM calorimeter (strips) with respect to the total energy of the cluster. A $Z \rightarrow \mu\mu\gamma$ event will pass the final selection if at least one cluster is found that satisfies the requirements of Table 6.4. If more than one clusters are found in a cone around a muon, then only the leading cluster in E_T is kept. In this chapter when referring to the energy, transverse energy and pseudorapidity of a candidate FSR photon in a $Z \rightarrow \mu\mu\gamma$ event, it is always referring to the leading cluster in E_T in this event.

Analysis Step	Analysis cutflow
Loose FSR Selection	$Z \rightarrow \mu\mu\gamma$ events with at least one γ with $\Delta R_{\text{cluster},\mu} < 0.3$
Analysis cut1	$E_T > 1.3$ GeV
Analysis cut2	$f_1 > 0.15$
Analysis cut3	$\Delta R_{\text{cluster},\mu} < 0.15$

Table 6.4: FSR analysis cutflow.

The actual values of the cuts chosen in Table 6.4, were determined using optimization studies based on Monte Carlo. For these studies a dedicated MC truth

classification is required. An FSR photon signal $Z \rightarrow \mu\mu\gamma$ event is defined as follows:

- The event should have at least one generated FSR photon within the fiducial region $E_{T,\gamma} > 1.3$ GeV and $\Delta R_{\gamma,\mu} < 0.15$, at the generator (truth) level.
- The reconstructed photon cluster should be matched with a true FSR photon from the Z decay within a 0.2 cone.

In ATLAS the EM object (electron and photon) truth classification is done by the MCTruthClassifier algorithm. In the case of EM clusters, the algorithm starts from the reconstructed cluster position in an attempt to match the cluster with real particles at the generator level. In this analysis the reconstructed clusters are classified as signal (FSR photons from Z decays), hadronic background (clusters originating from hadrons like pions, kaons etc) and μ background (clusters originating from muon ionization in the EM LAr calorimeter).

The specific selection of the cut values used in this analysis was optimized using the distributions of f_1 and $\Delta R_{\text{cluster},\mu}$ for signal and backgrounds. The distributions of these variables from MC are shown in Figure 6.2. Black histograms correspond to signal. The backgrounds are presented in filled coloured histograms (μ background in blue and hadronic background in green). The f_1 plot is shown after the $E_T > 1.3$ GeV cut, and the $\Delta R_{\text{cluster},\mu}$ plot is shown after the $E_T > 1.3$ GeV and $f_1 > 0.15$ cuts. The longitudinal shower shape cut $f_1 > 0.15$ is applied mainly to remove the muon ionization background and the tight cone cut $\Delta R_{\text{cluster},\mu} < 0.15$ is applied to further reduce the hadronic background. In Figure 6.3, the $\Delta R_{\text{cluster},\mu}$ distribution is shown after the $E_T > 1.3$ GeV cut, and the f_1 plot is shown after the $E_T > 1.3$ GeV and $\Delta R_{\text{cluster},\mu} < 0.15$ cuts. A large amount of hadronic background is removed by the tight cone cut. The muon induced background is expected to be reduced by the f_1 cut. The fractions of the different background components after each step of the analysis cutflow are listed in Table 6.5.

The 2D correlation plots of these variables (f_1 and $\Delta R_{\text{cluster},\mu}$) after an $E_T > 1.3$ GeV cut, are shown in Figure 6.4. The FSR Signal is shown in Figure 6.4(a). The “ μ background” (clusters generated by muon ionization in the calorimeter) is shown in blue in Figure 6.4(b), and the “hadronic background” in green in Figure 6.4(c). The same 2D representation for signal and all background components is shown in Figure 6.4(d). The FSR signal has larger f_1 because low energy photons leave a large fraction of their energy in the strip section of the LAr calorimeter. Clusters originating from hadrons (“hadronic background”) are concentrated at large ΔR . The “ μ background” is fully contained in $\Delta R_{\text{cluster},\mu} \simeq 0.15$. This has to do with the

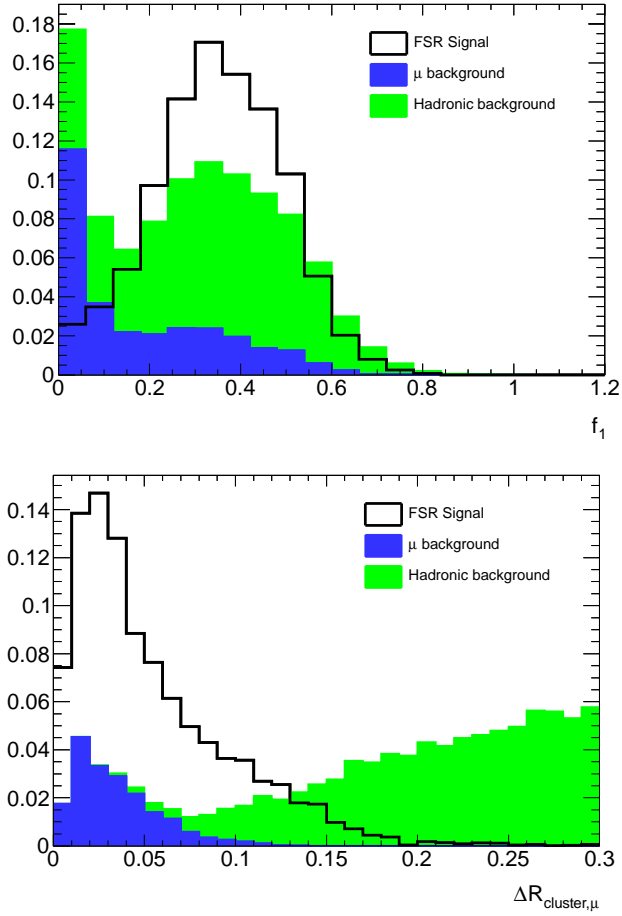


Figure 6.2: Distributions of f_1 and $\Delta R_{\text{cluster},\mu}$ discriminants from $Z \rightarrow \mu\mu$ Monte Carlo: the f_1 distribution (top) is shown after an $E_T > 1.3$ GeV cut. The $\Delta R_{\text{cluster},\mu}$ distribution (bottom) is shown after the $E_T > 1.3$ GeV and $f_1 > 0.15$ cuts. Black histograms correspond to signal. The backgrounds are shown in coloured filled histograms (μ background in blue and hadronic background in green).

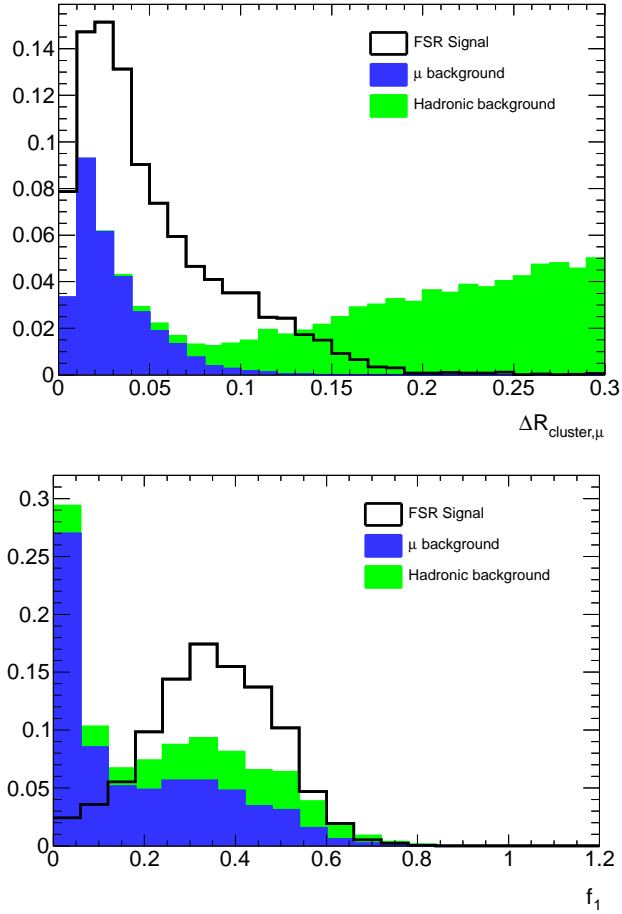


Figure 6.3: Distributions of f_1 and $\Delta R_{\text{cluster},\mu}$ discriminants from $Z \rightarrow \mu\mu$ Monte Carlo: the $\Delta R_{\text{cluster},\mu}$ distribution (top) is shown after an $E_T > 1.3$ GeV cut. The f_1 distribution (bottom) is shown after the $E_T > 1.3$ GeV and $\Delta R_{\text{cluster},\mu} < 0.15$ cuts. Black histograms correspond to signal. The backgrounds are shown in coloured filled histograms (μ background in blue and hadronic background in green).

size of EM clusters used in this analysis. The cluster size is 3×5 corresponding to $\Delta\eta \times \Delta\varphi = 0.075 \times 0.125$, leading to $\Delta R_{\text{cluster},\mu} \simeq 0.146$.

Analysis cutflow	Fraction of μ bkg [%]	Fraction of hadronic bkg [%]
$E_T > 1.3$ GeV	30.55	69.45
$f_1 > 0.15$	19.17	80.83
$\Delta R_{\text{cluster},\mu} < 0.15$	56.47	43.53

Table 6.5: Fractions of different background components after each step of FSR analysis cutflow.

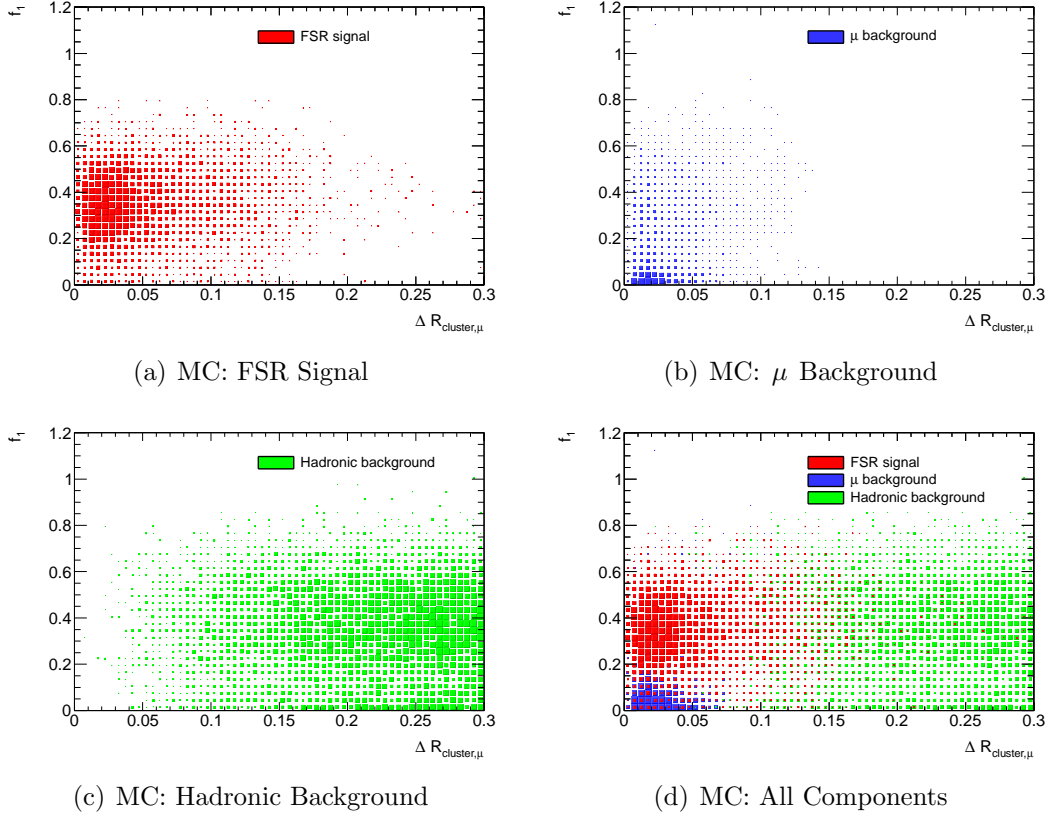


Figure 6.4: 2D correlation plots of discriminants f_1 and $\Delta R_{\text{cluster},\mu}$ after an $E_T > 1.3$ GeV cut from $Z \rightarrow \mu\mu$ Monte Carlo. The FSR signal $Z \rightarrow \mu\mu\gamma$ is shown in (a). The μ background (clusters produced by muon ionization in the LAr calorimeter) is shown in (b) and the hadronic background (clusters generated by hadrons) in (c). The same distributions for the signal and the two background components is shown in (d).

The dominant background contribution in this analysis originates from the $Z \rightarrow \mu\mu$ events themselves. One component comes from the muon energy loss in the LAr calorimeter (the “ μ background”), and the other component is the “hadronic background” originating from hadronic decays (mainly $\pi^0 \rightarrow \gamma\gamma$ decays). Note that events defined as signal and “ μ background”, may still have significant contamination from hadronic background. An example is the presence of pile-up in high luminosity runs. Smaller background contributions come from $Z \rightarrow \tau\tau$, $W \rightarrow \mu\nu$ and QCD events. These are highly suppressed after the $Z \rightarrow \mu\mu$ preselection.

One independent way to study the fraction of fake photon clusters after the full event selection, is to use MC $Z \rightarrow \mu\mu$ events without any FSR photon radiation. Such a study is summarized in Figure 6.5. The fake fraction is defined as the ratio of the events passing the full event selection divided by all $Z \rightarrow \mu\mu$ events without FSR radiation. The fraction of fakes is significant only in the range $3 > E_T > 1.3$ GeV, but it is still below 0.5%. It is interesting to note the minimum of the fake fraction at a $\Delta R_{\text{cluster},\mu} \simeq 0.1$ consistent with what is already seen in Figure 6.2. This minimum is produced by the fast fall of the muon energy loss fakes and the increasing hadronic fakes with increasing $\Delta R_{\text{cluster},\mu}$.

In summary, the expected yield of $Z \rightarrow \mu\mu\gamma$ events from Monte Carlo, after each selection cut ($E_T > 1.3$ GeV, $f_1 > 0.15$, $\Delta R_{\text{cluster},\mu} < 0.15$) is shown in Table 6.6. For an integrated luminosity of 164 pb^{-1} , 4287 $Z \rightarrow \mu\mu\gamma$ candidate events are expected to pass the final analysis cuts (this number is given before any correction for trigger efficiency effects).

Yields [pb]	FSR selection	Analysis cut1	Analysis cut2	Analysis cut3
MC signal ($Z \rightarrow \mu\mu\gamma$)	19.36	18.24	16.70	16.20
MC bkg total	326.17	42.50	29.19	9.94
MC bkg ($Z \rightarrow \mu\mu$)	325.92	42.44	29.14	9.89
MC bkg ($W \rightarrow \mu\nu, Z \rightarrow \tau\tau, \text{QCD}$)	0.25	0.06	0.05	0.04

Table 6.6: Expected yield of $Z \rightarrow \mu\mu\gamma$ signal and background events (in pb) passing each step of the final selection.

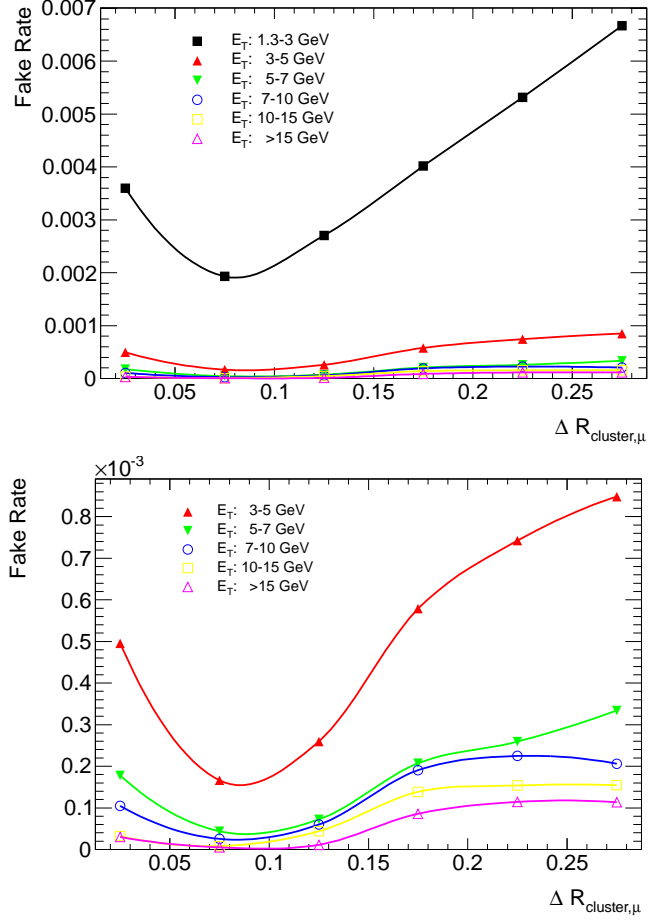


Figure 6.5: Fraction of $Z \rightarrow \mu\mu$ events with a fake photon as a function of $\Delta R_{\text{cluster},\mu}$. These events are obtained from $Z \rightarrow \mu\mu$ Monte Carlo events without any QED FSR radiation. The fake fraction is defined as the ratio of the events passing the full event selection divided by all $Z \rightarrow \mu\mu$ events without FSR radiation. The top figure shows the fake fraction for $E_T > 1.3$ GeV region. The bottom figure focuses in the $E_T > 3$ GeV region. The statistic errors are negligible.

6.4 FSR Photon Reconstruction Performance

In this section the special clustering (EM topo-seeded clustering) used in this analysis is presented. This special clustering allows reconstruction of EM clusters at energies below 4 GeV, the range where the standard ATLAS cluster reconstruction is inefficient. The obtained clusters, although already calibrated, need to be corrected for the presence of the muon energy loss. The performance of this correction in terms of photon cluster energy linearity and uniformity, is discussed in this section.

6.4.1 Special low energy clustering: EM topo-seeded clustering

The standard clustering algorithms in ATLAS are the sliding-window clustering and the topological clustering. The sliding-window clustering [100] provides fixed size clusters, which allows for a very precise cluster energy calibration. It is the standard cluster algorithm for the electron/photon reconstruction in ATLAS. However, the pre-cluster has a E_T^{thresh} threshold of 3 GeV, thus the standard egamma clustering cannot reconstruct electron/photon clusters with lower energies ($\lesssim 3$ GeV). The topological clustering [100] provides a non-fixed size cluster with a varying number of cells. The number of cells depends mostly on the energy of the incoming particle: more energetic particles produce larger showers and thus larger clusters. The non-fixed size makes the topological clusters more difficult to calibrate and intrinsically non-linear. However, the topological clustering is capable of finding very low energy clusters in the ATLAS LAr EM calorimeter, reaching energies as low as 500 MeV.

This very low energy reach of the topological clustering (EMTopo430) led to the idea, dating back to 2009, to use it in the first ATLAS collision data as a cluster-seed cell finder. Then a fixed cluster could be built around the found seed. This fixed cluster could be calibrated using the existing standard ATLAS reconstruction and calibration for fixed clusters. The original idea was to use these clusters for π^0 and J/ψ reconstruction, and for correcting the long tails of the $Z \rightarrow \mu\mu$ and the Higgs $\rightarrow 4l$ invariant masses. The choice of the fixed size window was 3×5 cells ($\Delta\eta \times \Delta\varphi = 0.075 \times 0.125$). The first public use of the EM topo-seeded clustering was in the reconstruction of $\pi^0 \rightarrow \gamma\gamma$ with the first collision data in ATLAS [108]. These fixed-size EM topo-seeded clusters are now part of the ATLAS offline with a dedicated calibration using $\pi^0 \rightarrow \gamma\gamma$ events and the longitudinal weight method (see Section 5.2 and Ref. [116]).

The E_T distributions of the reconstructed FSR photons after the final selec-

tion, using EM topo-seeded clustering and the standard sliding-window clustering, are shown in Figure 6.6 for data versus MC, and for MC Signal only. The MC is normalized to the luminosity of the data. As shown in Figure 6.6, the clustering used in this work extends the photon acceptance to lower E_T . Noting the logarithmic scale in Figure 6.6 one can appreciate a significant gain in the reconstruction efficiency of low energy photon clusters.

6.4.2 Photon Cluster Energy Calibration

The 3×5 fixed-size clusters used in this analysis, have been calibrated at the cluster level. The goal of the energy calibration is to obtain optimum linearity, uniformity and resolution. As already mentioned, a problem for the FSR photon candidates is that they may overlap with the high energy muon from the Z-boson decay, which can lead to an over-estimate of the reconstructed photon energy. For this reason, an extra correction of the photon cluster energy must be performed. In this section the correction procedure is presented.

High energy muons going through the LAr EM calorimeter lose energy via ionization. The energy which a muon deposits in the calorimeter follows a Landau distribution. This has been tested with cosmic muons in ATLAS and with halo muons in a combined test beam before the start of the LHC. The most probable energy value (MPV) of the muon Landau distribution for a 3×3 cluster made up by cells in the middle section of the LAr calorimeter in the range $0.3 < |\eta| < 0.4$ was measured to be $\simeq 260$ MeV [88]. Although a detailed treatment of this energy deposition in the photon cluster would require finding the cells traversed by the muon and performing a parametrization of the muon energy loss, for this analysis it was deemed sufficient to apply a constant energy subtraction of 300 MeV for a 3×5 cluster. This flat energy correction is applied only when the extrapolated muon traverses the 3×5 cluster.

In this section the performance of this correction is studied using Monte Carlo $Z \rightarrow \mu\mu\gamma$ events. The calibrated FSR photon cluster energy resolution before any correction for muon energy loss in the same cluster, is shown in Figures 6.7 and 6.9. The energy resolution is defined in % as follows:

$$\frac{E_{Recon,\gamma} - E_{True,\gamma}}{E_{True,\gamma}}. \quad (6.1)$$

From Figure 6.7 is apparent that the FSR photon cluster energy at low energies is overcorrected due to the overlapping muon from the Z decay. The energy resolution for the same photons is shown in Figures 6.8 and 6.10 after subtraction of a fixed

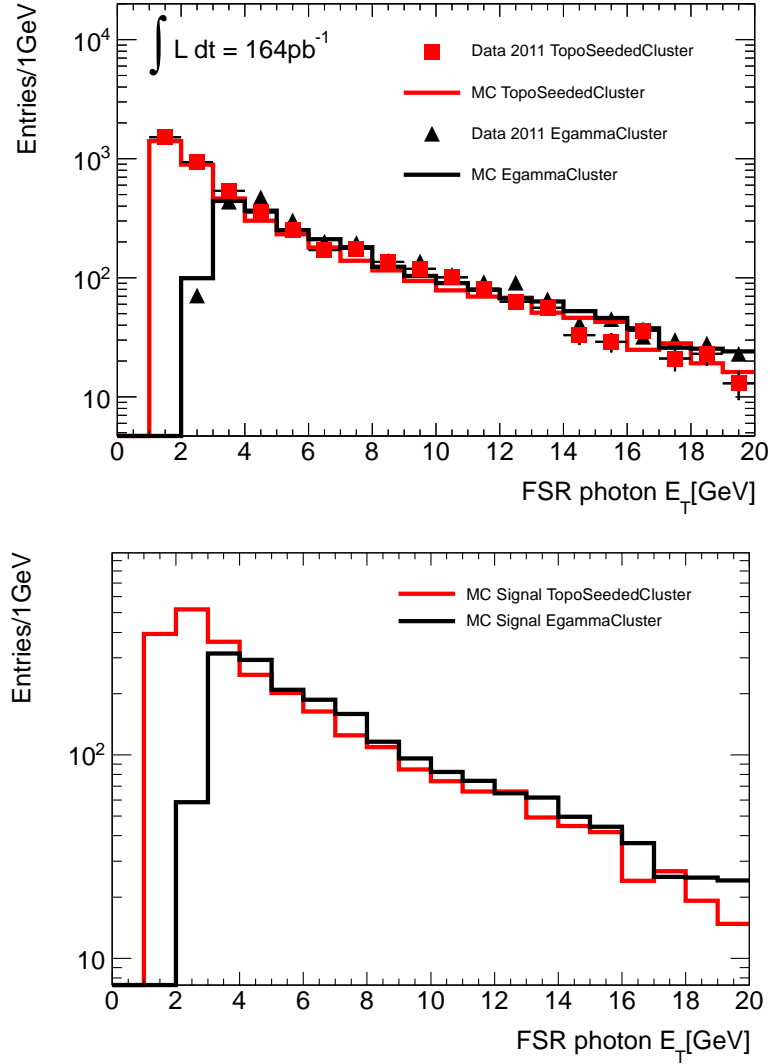


Figure 6.6: Top (Data vs MC): reconstructed EM topo-seeded 3×5 photon cluster E_T compared to the standard sliding-window cluster E_T after final selection for data and $Z \rightarrow \mu\mu\gamma$ MC. The MC is normalized to the data luminosity. The EM topo-seeded clustering used in this work extends the photon acceptance to lower E_T . Bottom (MC-only): E_T distributions for reconstructed photon clusters matched to true FSR photons for the two different clusterings.

energy of 300 MeV. At the lowest energy bin the distributions look asymmetric due to the presence of a high energy tail. These large high energy tails are mainly caused by the almost energy independent muon energy loss in the LAr calorimeter. Since only an average energy correction is applied to the cluster energy, the high energy tail is more visible in the low energy bins (e.g. Figure 6.7(a) to be compared with Figure 6.7(d)). At higher cluster energies ($E > 5$ GeV) a low energy tail is observed in the resolution plots. These low energy tails appear at higher energies because of the increased numbers of clusters reconstructed in regions of higher pseudorapidity hence reconstructed in the crack region and regions of higher material upstream the calorimeter (e.g. Figure 6.9(c)).

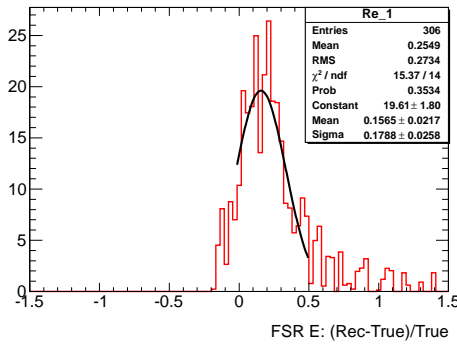
To extract the energy linearity and uniformity, a Gaussian fit is applied to each histogram produced by Eq. 6.1 around the peak region. The photon energy uniformity and linearity are shown in Figure 6.11 before correction and in Figure 6.12 after correction. It can be seen that the linearity is significantly improved at low energies where the presence of an overlapping muon is biasing the FSR photon energy. According to Figures 6.11 and 6.12, the improvement goes from a 16% non-linearity to better than 2% around the 1.3 – 2 GeV region.

6.5 Measurements of the $Z \rightarrow \mu\mu\gamma$ yields and the fiducial cross-section

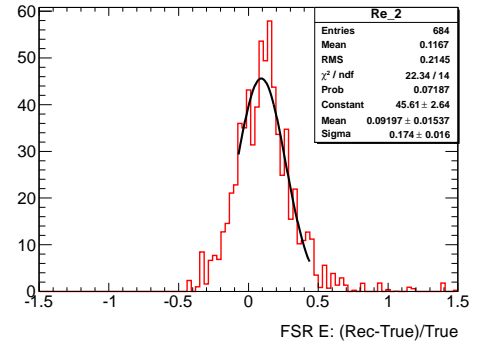
The event selection discussed in Section 6.3 leads to a final sample of $Z \rightarrow \mu\mu\gamma$ candidates with at least one photon within the fiducial region $E_T > 1.3$ GeV and $\Delta R_{\gamma,\mu} < 0.15$. In this section the final yields of $Z \rightarrow \mu\mu\gamma$ events as a function of energy, transverse energy, $|\eta|$, φ , f_1 and $\Delta R_{\text{cluster},\mu}$ is presented. These yields are compared with the corresponding Monte Carlo predictions. In these comparisons the signal purity and the background composition are identified using Monte Carlo. Finally, the cross-section for the $Z \rightarrow \mu\mu\gamma$ events with at least one γ within the photon fiducial region $E_T > 1.3$ GeV and $\Delta R_{\gamma,\mu} < 0.15$ is measured.

The MC cutflow table for signal $Z \rightarrow \mu\mu\gamma$ events is given in Table 6.7. The relative efficiencies for each step are also provided. The predicted event numbers are not corrected for trigger efficiency, but they are reweighted to match the pile-up vertex distribution in data.

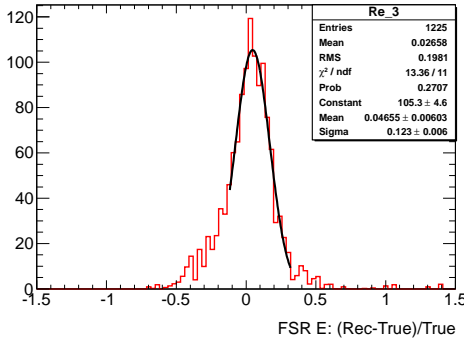
Reconstruction of QED final state radiation photons in $Z \rightarrow \mu\mu$ decays in 7 TeV pp collisions
 6.5. Measurements of the $Z \rightarrow \mu\mu\gamma$ yields and the fiducial cross-section



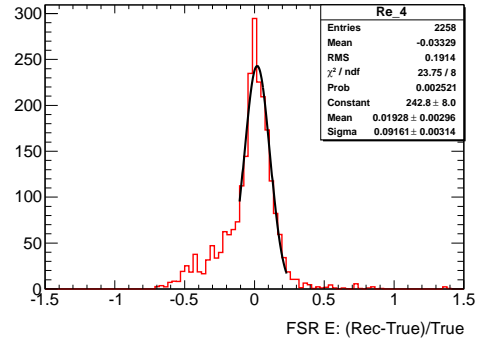
(a) Energy bin : 1.3 – 2 GeV



(b) Energy bin : 2 – 3 GeV



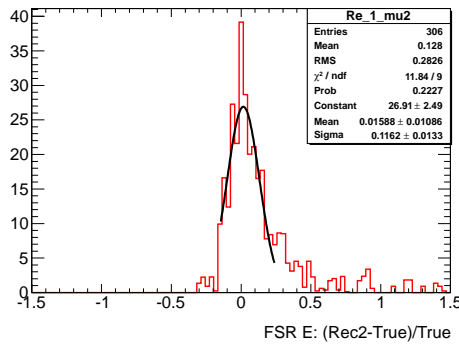
(c) Energy bin : 3 – 5 GeV



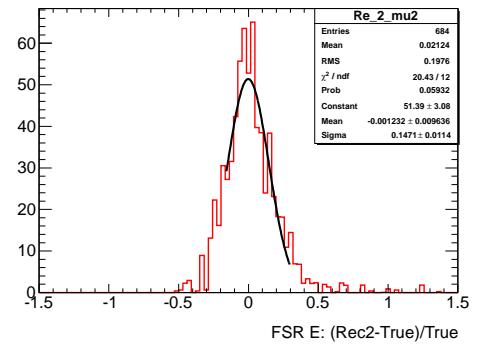
(d) Energy bin : 5 – 10 GeV

Figure 6.7: Calibrated photon energy resolution in bins of energy before applying a cluster energy correction.

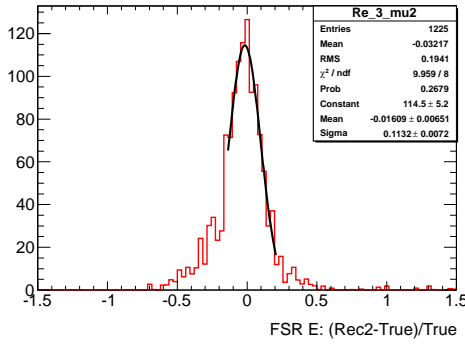
Reconstruction of QED final state radiation photons in $Z \rightarrow \mu\mu$ decays in 7 TeV pp
 6.5. Measurements of the $Z \rightarrow \mu\mu\gamma$ yields and the fiducial cross-section collisions



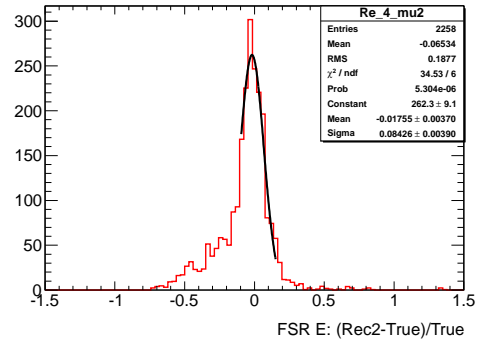
(a) Energy bin : 1.3 – 2 GeV



(b) Energy bin : 2 – 3 GeV



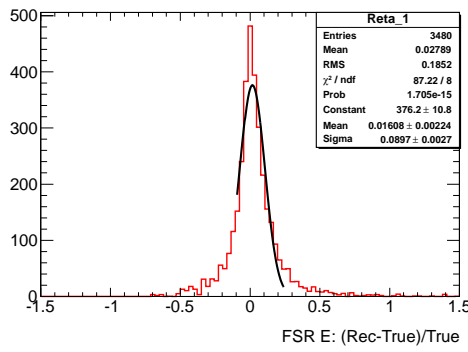
(c) Energy bin : 3 – 5 GeV



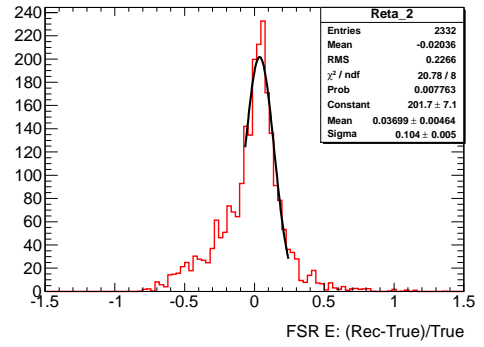
(d) Energy bin : 5 – 10 GeV

Figure 6.8: Calibrated photon energy resolution in bins of energy after application of a correction for the overlapping muon energy (see text).

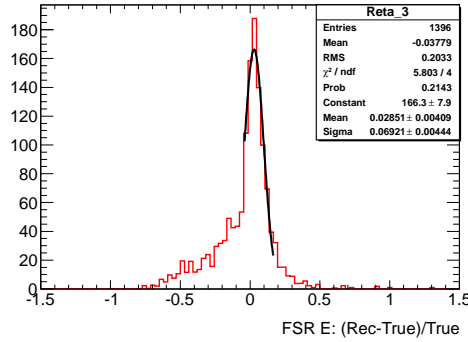
Reconstruction of QED final state radiation photons in $Z \rightarrow \mu\mu$ decays in 7 TeV pp
 6.5. Measurements of the $Z \rightarrow \mu\mu\gamma$ yields and the fiducial cross-section collisions



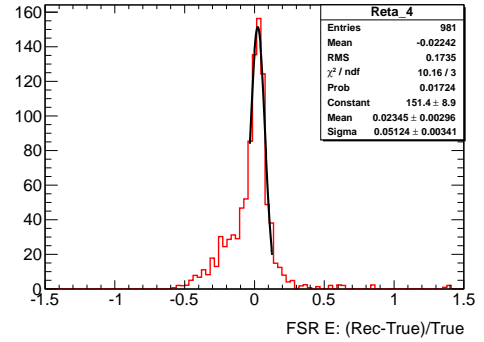
(a) Eta bin : 0 – 0.8



(b) Eta bin : 0.8 – 1.5



(c) Eta bin : 1.5 – 2.0



(d) Eta bin : 2.0 – 2.5

Figure 6.9: Calibrated photon energy resolution in bins of eta before applying a cluster energy correction.

Reconstruction of QED final state radiation photons in $Z \rightarrow \mu\mu$ decays in 7 TeV pp
 6.5. Measurements of the $Z \rightarrow \mu\mu\gamma$ yields and the fiducial cross-section collisions

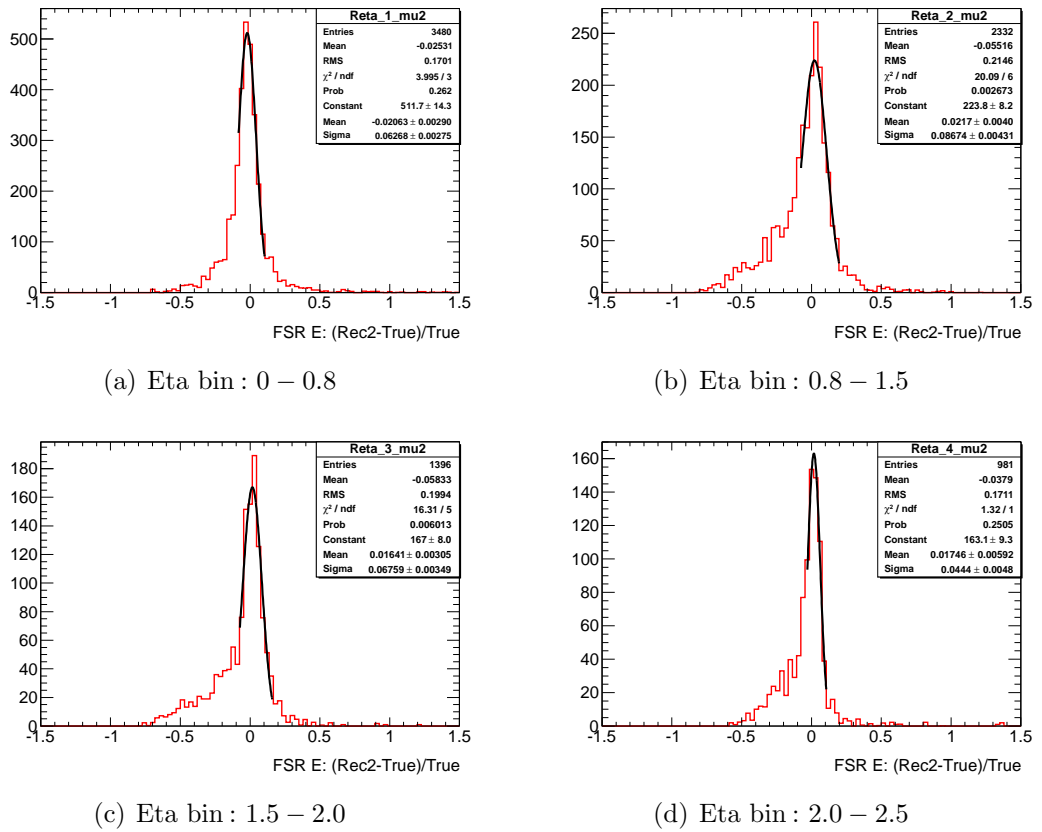


Figure 6.10: Calibrated photon energy resolution in bins of eta after application of a correction for the overlapping muon energy (see text).

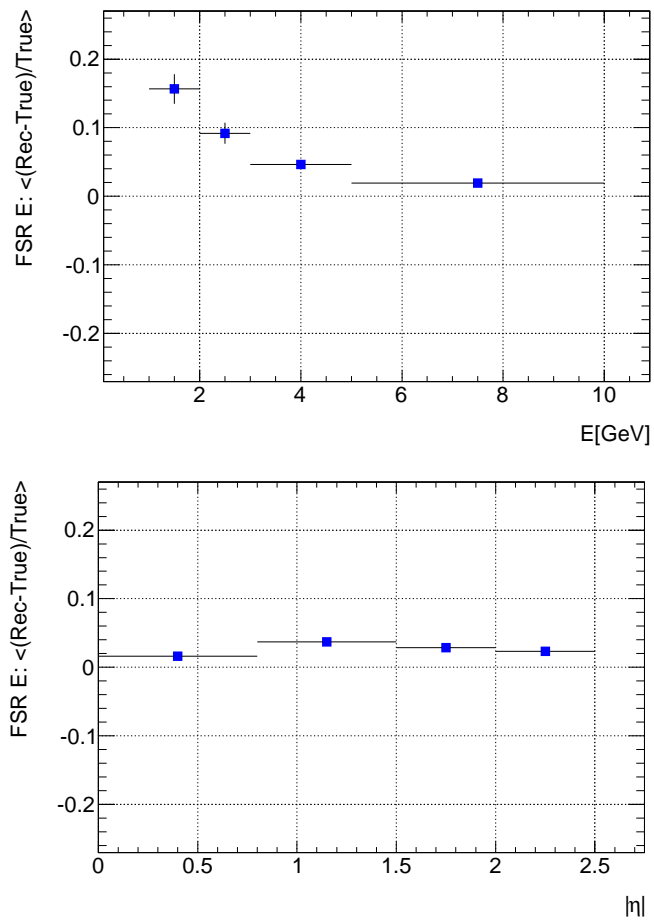


Figure 6.11: Photon energy linearity (top) and uniformity (bottom) before photon energy correction.

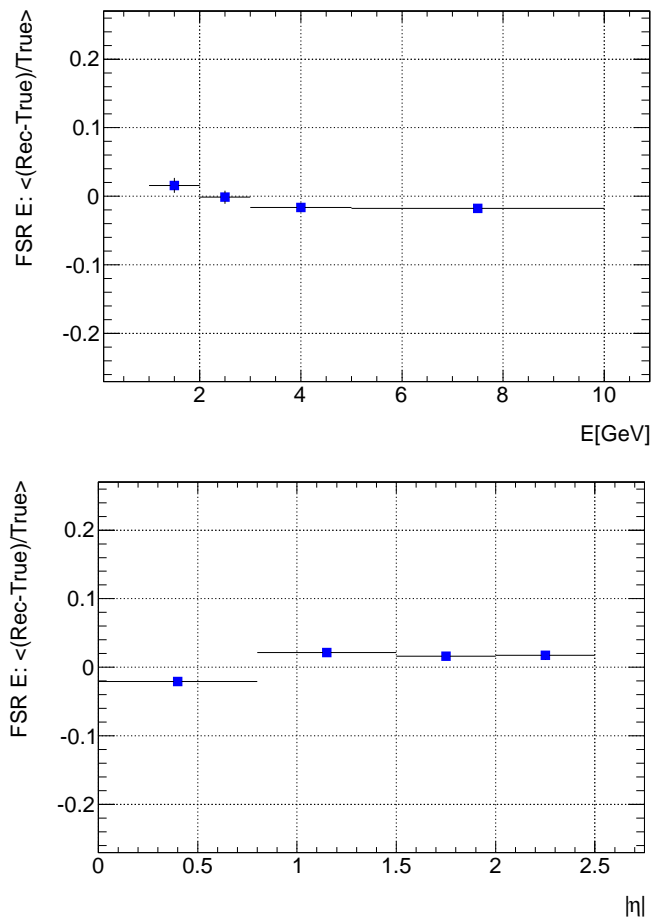


Figure 6.12: Photon energy linearity (top) and uniformity (bottom) after photon energy correction.

Cut description	N_{events}	Rel.Eff.(%)
Generated $Z \rightarrow \mu\mu\gamma$ events within fiducial region ($E_{T,\gamma}^{gen} > 1.3\text{GeV}$, $\Delta R_{\gamma,\mu}^{gen} < 0.15$)	34739.0	100.00
Events with at least one reconstructed γ with $\Delta R_{cluster,\mu} < 0.3$	9788.3	28.18
Cut1: $E_{T,cluster} > 1.3\text{GeV}$	9218.4	94.18
Cut2: $f_1 > 0.15$	8441.3	91.57
Cut3: $\Delta R_{cluster,\mu} < 0.15$	8191.4	97.04

Table 6.7: Cut-flow table for MC signal $Z \rightarrow \mu\mu\gamma$ events. The predicted event numbers are not corrected for trigger efficiency, but they are reweighted to match the pile-up vertex distribution in data. The efficiencies have been investigated systematically by varying the corresponding cut values. The accuracy on efficiency is $\pm 1\%$ due to systematics (see Section 6.6 for more details). The statistic errors are negligible.

	ϵ_{Data}	ϵ_{MC}	SF
Barrel	0.748 ± 0.001	0.738	1.014 ± 0.001
Endcap	0.889 ± 0.001	0.882	1.008 ± 0.001

Table 6.8: Summary of the muon trigger efficiencies and scale factor for EF_mu18_MG , with statistic errors. The statistic errors on ϵ_{MC} are negligible. (taken from Ref. [117]).

6.5.1 Correction of MC predictions for trigger efficiency

Events are required to pass the trigger as part of the event selection. The trigger efficiencies can be different between data and Monte Carlo. Therefore, a scale factor, defined as the ratio between the efficiency on data and the efficiency on Monte Carlo, is required to rescale the number of events measured in Monte Carlo.

The muon trigger efficiency is measured with the “tag-and-probe” method using Z decays. An unbiased high p_T muon sample is selected using Z decaying into di-muon pairs. The events are required to have one good muon with tight selection as the “tag”, and the other muon with loose selection as the “probe”. The tag together with the probe are required to match the signature of a Z boson decay, e.g. the di-muon pair has to be within the correct invariant mass range and with opposite charge. To avoid any bias caused by the trigger, all tags are required to have associated trigger object which pass a trigger decision of an event. The efficiency is determined

Reconstruction of QED final state radiation photons in $Z \rightarrow \mu\mu$ decays in 7 TeV pp collisions
 6.5. Measurements of the $Z \rightarrow \mu\mu\gamma$ yields and the fiducial cross-section

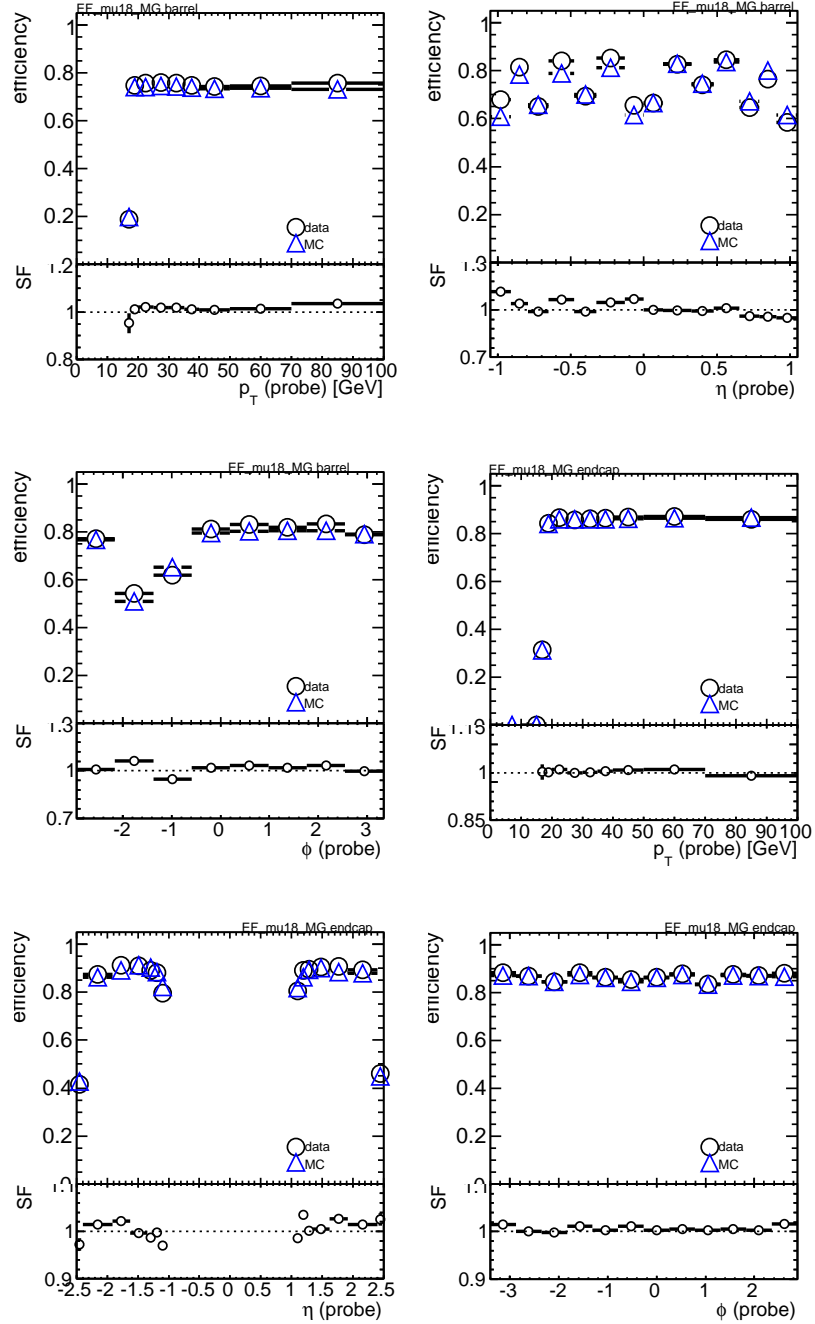


Figure 6.13: The trigger efficiencies as a function of p_T , η and ϕ with respect to selected muons, for barrel region and endcap region (taken from Ref. [117]).

Event type	N_{events}	Fraction
BB	55570	0.281
EE	46714	0.237
BE	95226	0.482

Table 6.9: Numbers and fractions of Z events in Monte Carlo in which two muons go into each of the three possible combinations of barrel and endcap.

from the fraction of probes which are matched to a trigger object. *EF_mu18_MG* is recommended as the lowest threshold single-muon trigger for period B2 and D during 2011 data taking campaign. The trigger efficiencies as a function of p_T , η and φ with respect to selected muons, for barrel region and endcap region, are shown in Figure 6.13. A summary of muon trigger efficiencies and scale factors is given in Table 6.8, with statistical errors. Based on the single muon trigger efficiency, the trigger efficiency and its uncertainty of the Z event can be derived as:

$$\epsilon_Z^{trig} = 1 - (1 - \epsilon_{\mu 1}^{trig})(1 - \epsilon_{\mu 2}^{trig}) \quad (6.2)$$

$$\delta\epsilon_Z^{trig} = (1 - \epsilon_{\mu 1}^{trig})\delta\epsilon_{\mu 2}^{trig} + (1 - \epsilon_{\mu 2}^{trig})\delta\epsilon_{\mu 1}^{trig} \quad (6.3)$$

where two efficiency parameters are used here since the two muons can be both in barrel region (BB), or both in endcap region (EE), or one in barrel and the other in endcap (BE). The single muon trigger efficiencies are different in barrel and endcap, for both data and MC, as listed in Table 6.8. Thus an overall trigger efficiency is calculated as a weighted average to take into account the three different situations.

The fractions of Z candidates of each type BB, EE and BE are estimated using Monte Carlo. The events are required to pass $Z \rightarrow \mu\mu$ selections except the trigger. The numbers and fractions of three types of events are summarized in Table 6.9. The event trigger efficiency for each type is calculated using Equation 6.2, listed in Table 6.10. The overall weighted trigger efficiencies for Z events are obtained using the fractions provided in Table 6.9. The final trigger efficiencies and scale factor are provided in Table 6.11.

Event type	ϵ_{Data}	ϵ_{MC}
BB	0.9365 ± 0.0005	0.931
EE	0.9877 ± 0.0002	0.986
BE	0.9720 ± 0.0004	0.969

Table 6.10: Event trigger efficiencies in data and MC for $Z \rightarrow \mu\mu$ events in which two muons go into each of the three possible combinations of barrel and endcap. The statistic errors on ϵ_{MC} are negligible.

ϵ_{Data}	ϵ_{MC}	SF
0.9657 ± 0.0004	0.962	1.0038 ± 0.0004

Table 6.11: Summary of the trigger efficiencies for data and MC, and scale factor. The statistic errors on ϵ_{MC} are negligible.

6.5.2 Measurements of the $Z \rightarrow \mu\mu\gamma$ yields

The integrated yield for $Z \rightarrow \mu\mu\gamma$ events passing the Z preselection and each of the final event selection cut for an integrated luminosity of 164 pb^{-1} , is shown in Table 6.12 for data and Monte Carlo. The MC has been corrected for trigger efficiency and for pile-up effects and is normalized to the actual luminosity. A $Z \rightarrow \mu\mu\gamma$ event will pass a particular cut only if at least one photon cluster is found that passes the cut. From Table 6.12, one can see that the data systematically overshoot the MC expectation by about 5%. This is comparable to the systematic uncertainties discussed in the next Section. It is also consistent with an excess with respect to the MC, in the background normalization observed in a background-rich control region (see Section 6.6).

The leading candidate photon transverse energy, energy, $|\eta|$, φ , f_1 and $\Delta R_{\text{cluster},\mu}$ for $Z \rightarrow \mu\mu\gamma$ events passing the Z preselection and with at least one reconstructed cluster within a cone of $\Delta R_{\text{cluster},\mu} < 0.3$ are shown in Figure 6.14. The same distributions after the full event selection are shown in Figure 6.15. In all plots the Monte Carlo expectations are normalized to the measured integrated luminosity. The MC samples have been corrected for trigger efficiency and for pile-up effects. In these plots a good agreement between data and the MC prediction is found. As expected the signal purity improves dramatically at high photon E_T : the S/B becomes greater than 10/1 for $E_T > 3 \text{ GeV}$. The efficiency of finding the signal $Z \rightarrow \mu\mu\gamma$ events within the fiducial region is $\sim 70\%$, with respect to the reconstructed Z events that

Reconstruction of QED final state radiation photons in $Z \rightarrow \mu\mu$ decays in 7 TeV pp collisions
6.5. Measurements of the $Z \rightarrow \mu\mu\gamma$ yields and the fiducial cross-section

Cut description	Data N_{events}	MC prediction
Events with at least one reconstructed γ		
with $\Delta R_{\text{cluster},\mu} < 0.3$	61676	56882
Cut1: $E_{T,\text{cluster}} > 1.3\text{GeV}$	10583	9999
Cut2: $f_1 > 0.15$	7909	7554
Cut3: $\Delta R_{\text{cluster},\mu} < 0.15$	4593	4303

Table 6.12: Cut-flow table for data and Monte Carlo corresponding to an integrated luminosity of 164 pb^{-1} . The Monte Carlo has been corrected for trigger efficiency and has been normalized to the full integrated luminosity. A $Z \rightarrow \mu\mu\gamma$ event will pass a particular cut only if at least one photon cluster is found that passes the cut. The statistic errors are negligible.

have true FSR photons within the fiducial region. The efficiency plots as a function of true FSR photon transverse energy, energy, $|\eta|$, φ and $\Delta R_{\gamma,\mu}$ are shown in Figure 6.16. It can be noted that the efficiency increases with photon energy.

A study of the systematic uncertainties associated with the background normalization are presented in Section 6.6.

6.5.3 Measurement of the $Z \rightarrow \mu\mu\gamma$ fiducial cross-section

In this section the measurement of the cross-section of the $Z \rightarrow \mu\mu\gamma$ process with at least one hard FSR photon ($E_T > 1.3 \text{ GeV}$) radiated collinearly to the emitting muon ($\Delta R_{\gamma,\mu} < 0.15$) is presented. This cross-section can be obtained from:

$$\sigma_{Z \rightarrow \mu\mu\gamma}^{\text{fid}} = \frac{N^{\text{Signal}}}{C_{\text{FSR}} \times L_{\text{int}}} (E_{T,\gamma} > 1.3\text{GeV}, \Delta R_{\gamma,\mu} < 0.15), \quad (6.4)$$

where

- $N^{\text{Signal}} = N - B$. N is the number of $Z \rightarrow \mu\mu\gamma$ events in data passing all selection requirements, and B is the number of background events extracted from MC.
- L_{int} is the integrated luminosity corresponding to the run selections and trigger employed.

Reconstruction of QED final state radiation photons in $Z \rightarrow \mu\mu$ decays in 7 TeV pp
6.5. Measurements of the $Z \rightarrow \mu\mu\gamma$ yields and the fiducial cross-section collisions

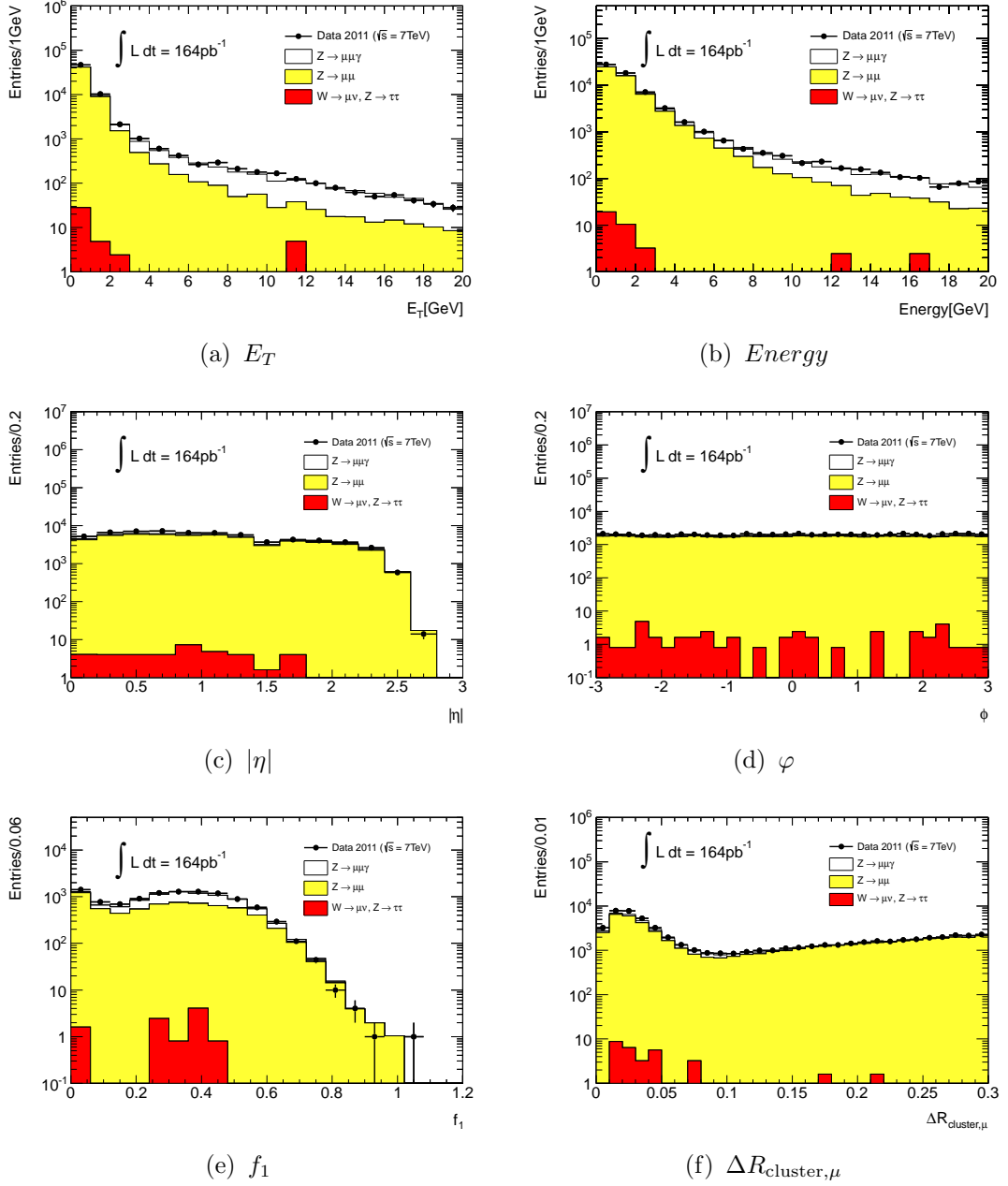


Figure 6.14: FSR photon transverse energy, energy, $|\eta|$, φ , f_1 and $\Delta R_{cluster,\mu}$ for events passing Z-boson preselection and FSR search.

Reconstruction of QED final state radiation photons in $Z \rightarrow \mu\mu$ decays in 7 TeV pp
6.5. Measurements of the $Z \rightarrow \mu\mu\gamma$ yields and the fiducial cross-section collisions

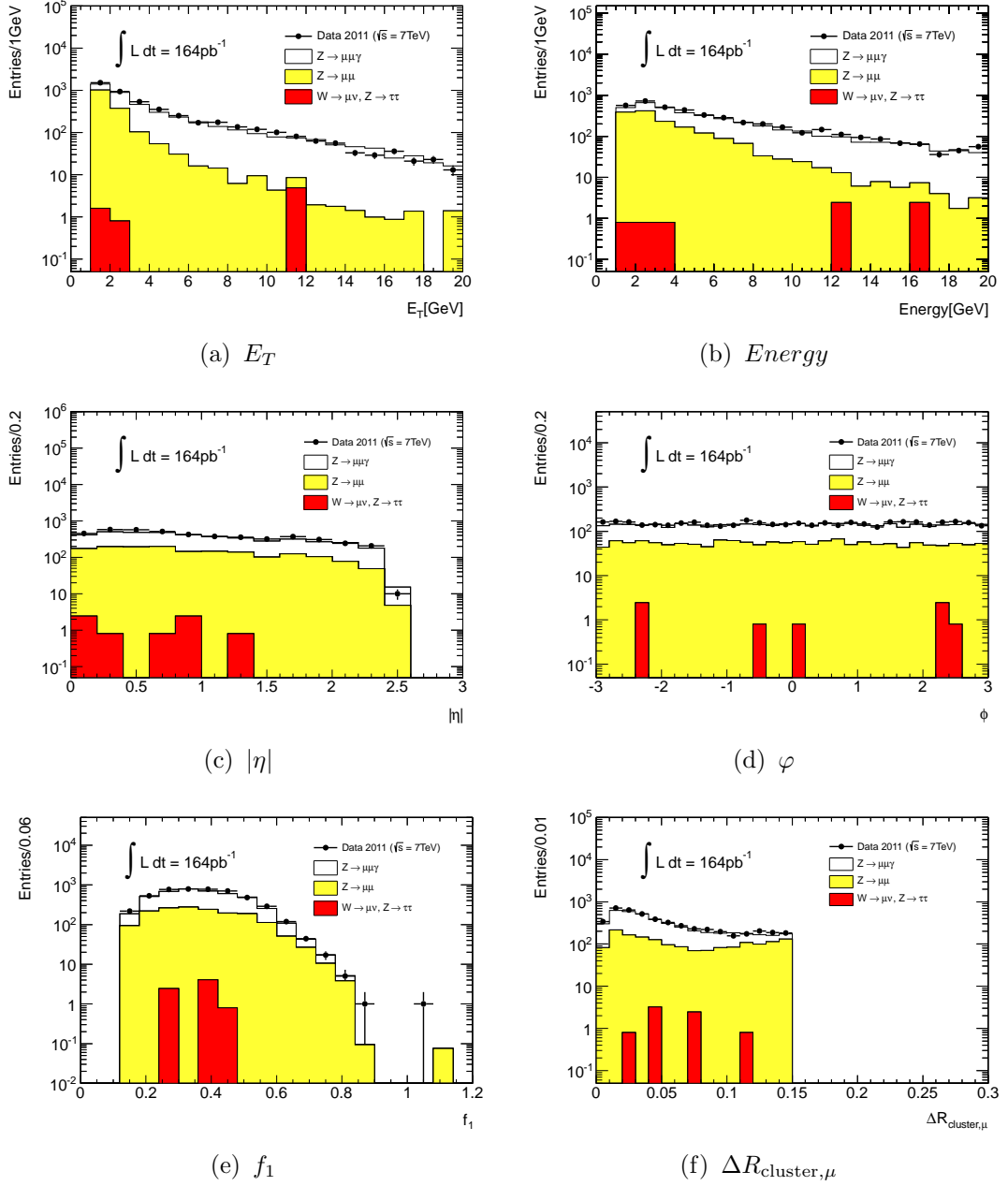


Figure 6.15: FSR photon transverse energy, energy, $|\eta|$, φ , f_1 and $\Delta R_{cluster,\mu}$ for events passing the FSR final selection.

Reconstruction of QED final state radiation photons in $Z \rightarrow \mu\mu$ decays in 7 TeV pp collisions
 6.5. Measurements of the $Z \rightarrow \mu\mu\gamma$ yields and the fiducial cross-section

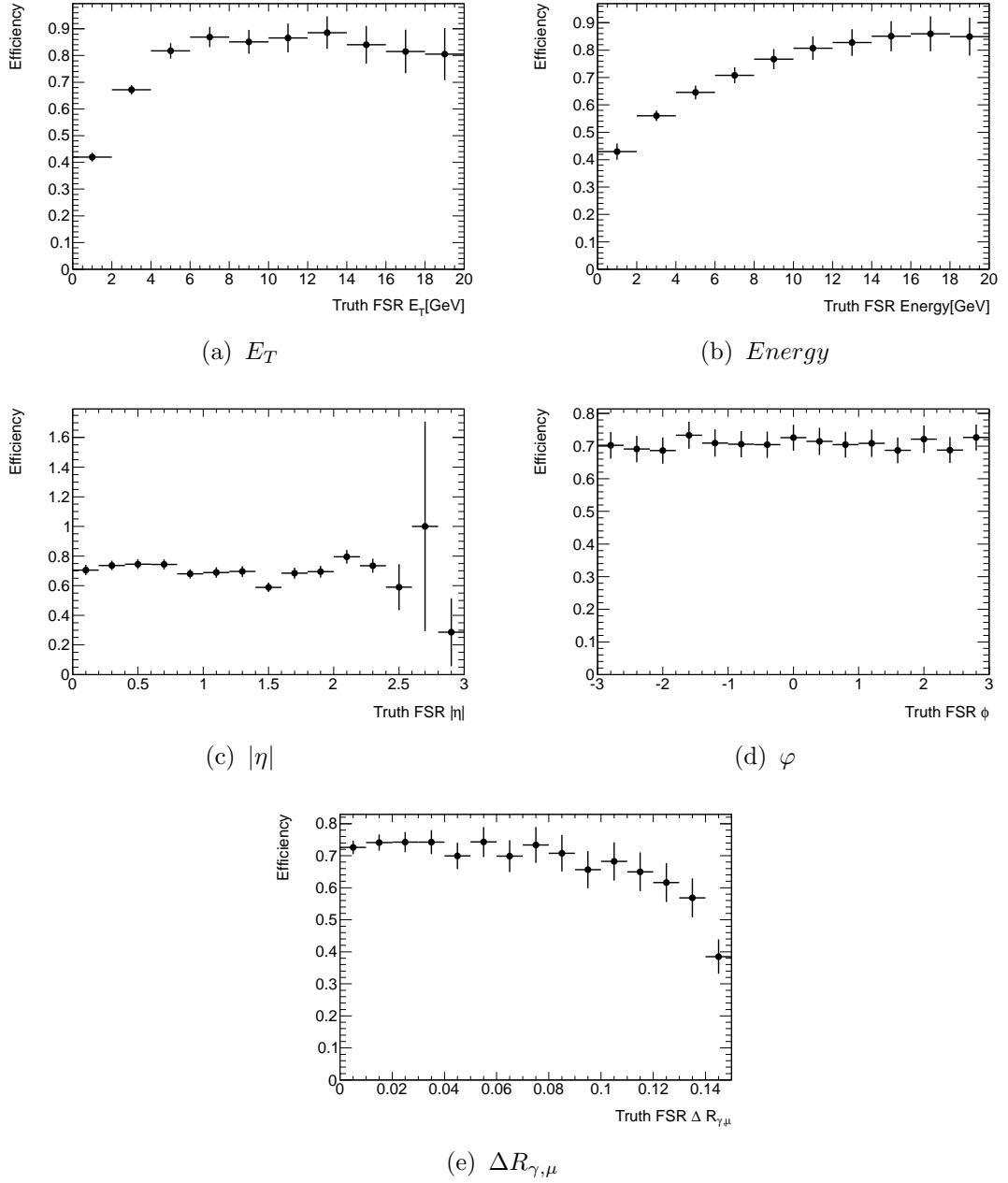


Figure 6.16: Efficiency as a function of true FSR photon transverse energy, energy, $|\eta|$, φ and $\Delta R_{\gamma,\mu}$.

	value
N^{Signal}	2847
$L_{int}[pb^{-1}]$	164
C_{FSR}	0.2367

Table 6.13: Summary of input quantities to the calculation of the $Z \rightarrow \mu\mu\gamma$ fiducial cross-section. N^{Signal} is the observed number of signal events after background subtraction, L_{int} is the integrated luminosity and C_{FSR} is an efficiency correction factor. The trigger efficiency scale factors used to correct the simulation for differences between data and MC are included in C_{FSR} . The statistic errors are negligible.

- C_{FSR} is the combined efficiency factor. This is the ratio of the total number of signal $Z \rightarrow \mu\mu\gamma$ events passing the selection requirements divided by the total number of generated $Z \rightarrow \mu\mu\gamma$ events with at least one photon within the fiducial region. It is calculated from simulation and corrected for the difference in trigger efficiency between data and simulation (see Tables 6.7 and 6.11).

The observed number of signal events after background subtraction, the correction factor C_{FSR} and the integrated luminosity are summarised in Table 6.13. The trigger efficiency scale factors used to correct the simulation for differences between data and MC are included in the C_{FSR} factor.

The measured $Z \rightarrow \mu\mu\gamma$ fiducial cross-section is:

$$\sigma_{Z \rightarrow \mu\mu\gamma}^{fid} = 0.073 \pm 0.001(\text{stat}) \pm 0.006(\text{sys}) \pm 0.002(\text{lum}) \text{ nb.} \quad (6.5)$$

The sum of the statistical and systematic uncertainties with the luminosity uncertainty reported separately, is of order 10%. The systematic uncertainties are discussed in Section 6.6. The measured $Z \rightarrow \mu\mu\gamma$ fiducial cross-section is consistent with the Monte Carlo prediction using NNLO QCD calculation including QED FSR. This was estimated using the fraction of generated $Z \rightarrow \mu\mu\gamma$ events with at least one photon in the fiducial region ($E_{T,\gamma} > 1.3 \text{ GeV}, \Delta R_{\gamma,\mu} < 0.15$) divided by the number of generated $Z \rightarrow \mu\mu$ events (Table 6.2) and the inclusive $Z \rightarrow \mu\mu$ cross-section provided in Table 6.1.

6.6 Systematic Uncertainties

In this section the various systematic uncertainties entering the measurement of the $Z \rightarrow \mu\mu\gamma$ yields are discussed. The systematic uncertainty on the luminosity is $\pm 3.4\%$ [118]. Theoretical uncertainties in the prediction of the background and the signal $Z \rightarrow \mu\mu\gamma$ yields are discussed. Uncertainties in the prediction of the background originate from the MC description of the Z preselection and the final event selection. Finally the predicted background normalization carries an uncertainty that can in principle be controlled using background-rich control regions.

6.6.1 Theoretical uncertainties

A comparison of the measured $Z \rightarrow \mu\mu\gamma$ yield with the expectation from Monte Carlo is limited by a number of theoretical uncertainties. These include the theoretical uncertainties on the Z geometrical acceptance, the theoretical uncertainties due to the FSR fiducial cuts at generator level, and the theoretical uncertainties from the QED FSR generator (PHOTOS). In the case of this chapter theory uncertainties coming from the photon generator level fiducial cuts are ignored. Instead the uncertainties on the reconstruction efficiencies originating from the E_T and ΔR cuts are considered.

The Z geometrical acceptance in this analysis is close to the one used in the inclusive $Z \rightarrow \mu\mu$ cross-section measurement [112]. The central values of the acceptance is calculated using the PYTHIA samples generated with the modified LO PDF MRSTLO*. The statistical uncertainty is negligible. The dominant contribution to the systematics is due to the limited knowledge of the Parton Density Functions (PDF) used to model the Z production at LHC. This affects directly the measurement of the acceptance parameter. The relative uncertainty on the acceptance can be obtained by combining three different components: the uncertainties within one PDF set, the uncertainties due to differences between PDF sets, the uncertainties due to the parton shower model. More detailed descriptions can be found in the Ref. [112]. The total uncertainty on the Z geometrical acceptance factors is 3.8%.

Theory uncertainties coming from the MC generator prediction are relatively small. The QED FSR generator PHOTOS [66] can be used for simulation chains at LHC aiming at 0.2% precision tag in single Z or W production and at their common studies [76]. Agreement better than 0.2% in experimental cuts (ATLAS, CDF) between PHOTOS and KKMC [78] was found. The recent ongoing study between PHOTOS and SANC [52] has already shown a reasonable agreement of 0.2%

for the QED FSR in the inclusive $Z \rightarrow \mu\mu$ and $Z \rightarrow ee$. More details can be found in Ref. [77].

6.6.2 Systematic Uncertainties due to the event selection

There are additional systematics due to disagreements in the selection discriminants between data and Monte Carlo. These are split into two categories: (i) the Z preselection systematics and (ii) the final (FSR) event selection systematics.

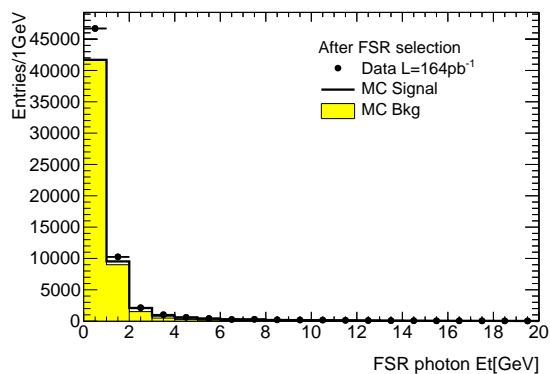
The total experimental uncertainty on the Z preselection is 0.9%, which is taken from the inclusive $Z \rightarrow \mu\mu$ cross-section measurement [44].

For the FSR final event selection cuts, the agreement between data and MC is shown in Figures 6.17, 6.18 and 6.19. Three graphs are provided for each cut. The first shows the distribution of the variable in data and MC. The second shows the fractional deviation (Data-MC)/(MC). The third graph shows the fraction of reconstructed $Z \rightarrow \mu\mu\gamma$ events passing the cut as a function of the cut threshold, for data and MC. The uncertainties coming from the E_T and ΔR cuts can be extracted by systematically varying the cut values. To estimate the uncertainty coming from the $E_T > 1.3$ GeV cut, the generator level photon $E_{T,\gamma}^{\text{gen}}$ is varied to estimate the difference in efficiency. The range of this variation is determined by the photon energy scale uncertainty at 1.3 GeV. After varying the generator level $E_{T,\gamma}^{\text{gen}}$ cut by $\sim \pm 5\%$, there is less than $\pm 0.5\%$ effect in the efficiency. The generator level $\Delta R_{\gamma,\mu}^{\text{gen}}$ cut is also varied from 0.145 to 0.155, and an effect not larger than $\pm 0.6\%$ has been observed. All these results are listed in Tables 6.14 and 6.15.

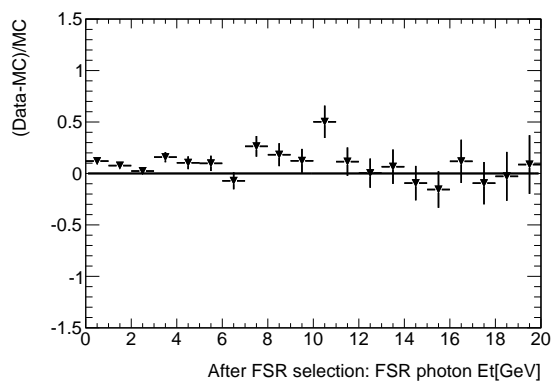
Cut Description	Efficiency[%]	Eff. Variation[%]
$E_{T,\gamma} > 1.3$ GeV	22.52	-
$E_{T,\gamma} > 1.235$ GeV	22.97	+0.45
$E_{T,\gamma} > 1.365$ GeV	22.11	-0.41

Table 6.14: Systematic uncertainty on $Z \rightarrow \mu\mu\gamma$ yields due to the photon $E_{T,\gamma}$ cut.

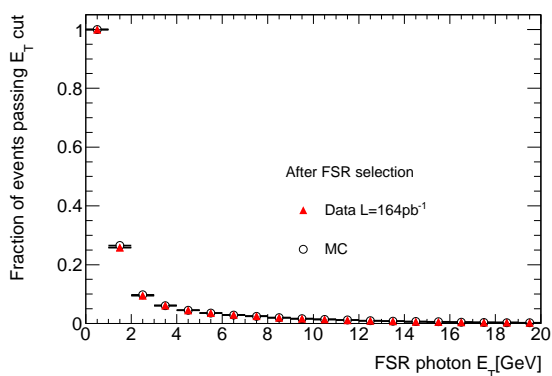
The systematic uncertainty on the longitudinal shower shape f_1 is estimated by applying variations of the cut value. Table 6.16 shows that the cut is varied from 0.14 to 0.16 with an impact on efficiency less than $\pm 1\%$.



(a) Data vs MC

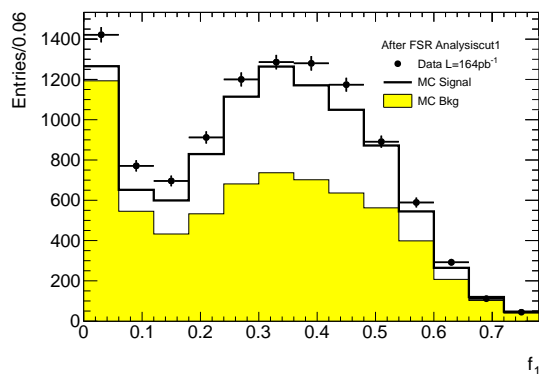


(b) $(Data-MC)/MC$

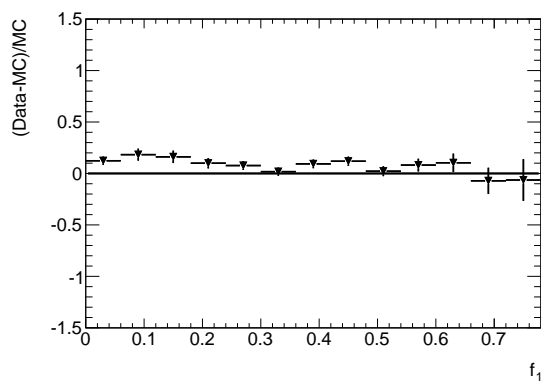


(c) Fraction of reconstructed events passing an E_T cut as a function of the cut

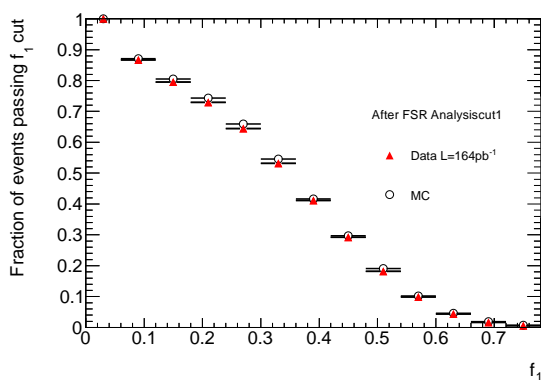
Figure 6.17: Comparison between Data and MC for reconstructed FSR photon E_T .



(a) Data vs MC

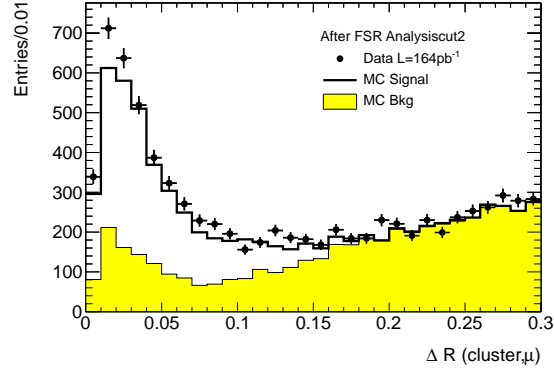


(b) (Data-MC)/MC

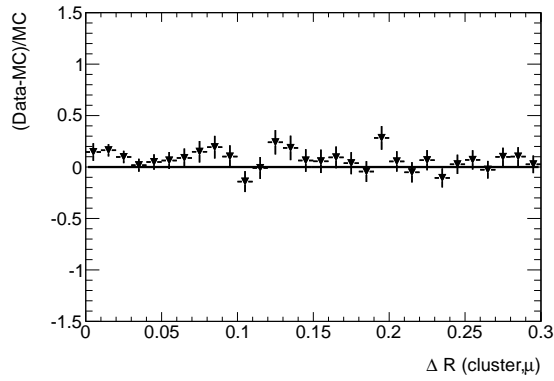


(c) Fraction of reconstructed events passing an f_1 cut as a function of the cut

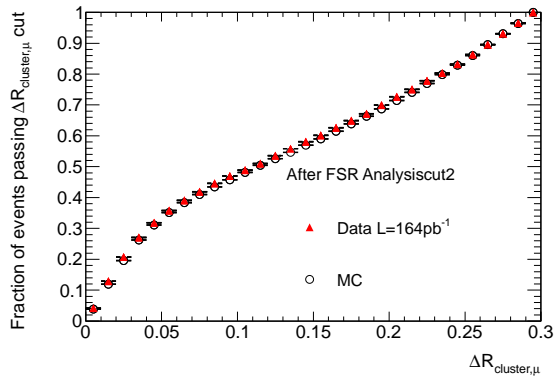
Figure 6.18: Comparison between Data and MC for reconstructed FSR photon f_1 .



(a) Data vs MC



(b) (Data-MC)/MC



(c) Fraction of reconstructed events passing a $\Delta R_{\text{cluster},\mu}$ cut as a function of the cut

Figure 6.19: Comparison between Data and MC for reconstructed FSR photon $\Delta R_{\text{cluster},\mu}$.

Cut Description	Efficiency[%]	Eff. Variation[%]
$\Delta R_{\gamma,\mu} < 0.15$	52.16	-
$\Delta R_{\gamma,\mu} < 0.145$	51.61	-0.55
$\Delta R_{\gamma,\mu} < 0.155$	52.67	+0.51

Table 6.15: Systematic uncertainty on $Z \rightarrow \mu\mu\gamma$ yields due to the photon $\Delta R_{\gamma,\mu}$ cut.

Cut Description	Efficiency[%]	Eff. Variation[%]
$f_1 > 0.15$	91.57	-
$f_1 > 0.14$	92.49	+0.92
$f_1 > 0.16$	90.63	-0.94

Table 6.16: Systematic uncertainty on $Z \rightarrow \mu\mu\gamma$ yields due to the photon f_1 cut.

6.6.3 Systematic uncertainties on the background normalization

Uncertainties on the background normalization are estimated using a background-rich control region. The control region is defined by inverting the f_1 cut. In Figure 6.20, four control plots defined by a cut inversion ($f_1 < 0.15$) are shown. The photon candidate transverse energy, energy, $|\eta|$ and $\Delta R_{\text{cluster},\mu}$ for events passing the inverted cut $f_1 < 0.15$ are plotted for data and MC. The signal events are shown in white, the μ background in blue and the hadronic background in green. An uncertainty band of $\pm 20\%$ for the background is also shown, with the boundaries shown in red. The data points are contained within the background uncertainty band. Based on these results a flat $\pm 20\%$ uncertainty on the background normalization has been considered. The impact of this normalization error on the overall measured $Z \rightarrow \mu\mu\gamma$ yield, is based on the background fraction after event selection: $B/(S+B) \simeq 38\%$. This leads to a $\pm 7.6\%$ uncertainty in the predicted $Z \rightarrow \mu\mu\gamma$ yield.

6.6.4 Summary

The full list of systematic uncertainties is given in Table 6.17.

Reconstruction of QED final state radiation photons in $Z \rightarrow \mu\mu$ decays in 7 TeV pp collisions
6.6. Systematic Uncertainties

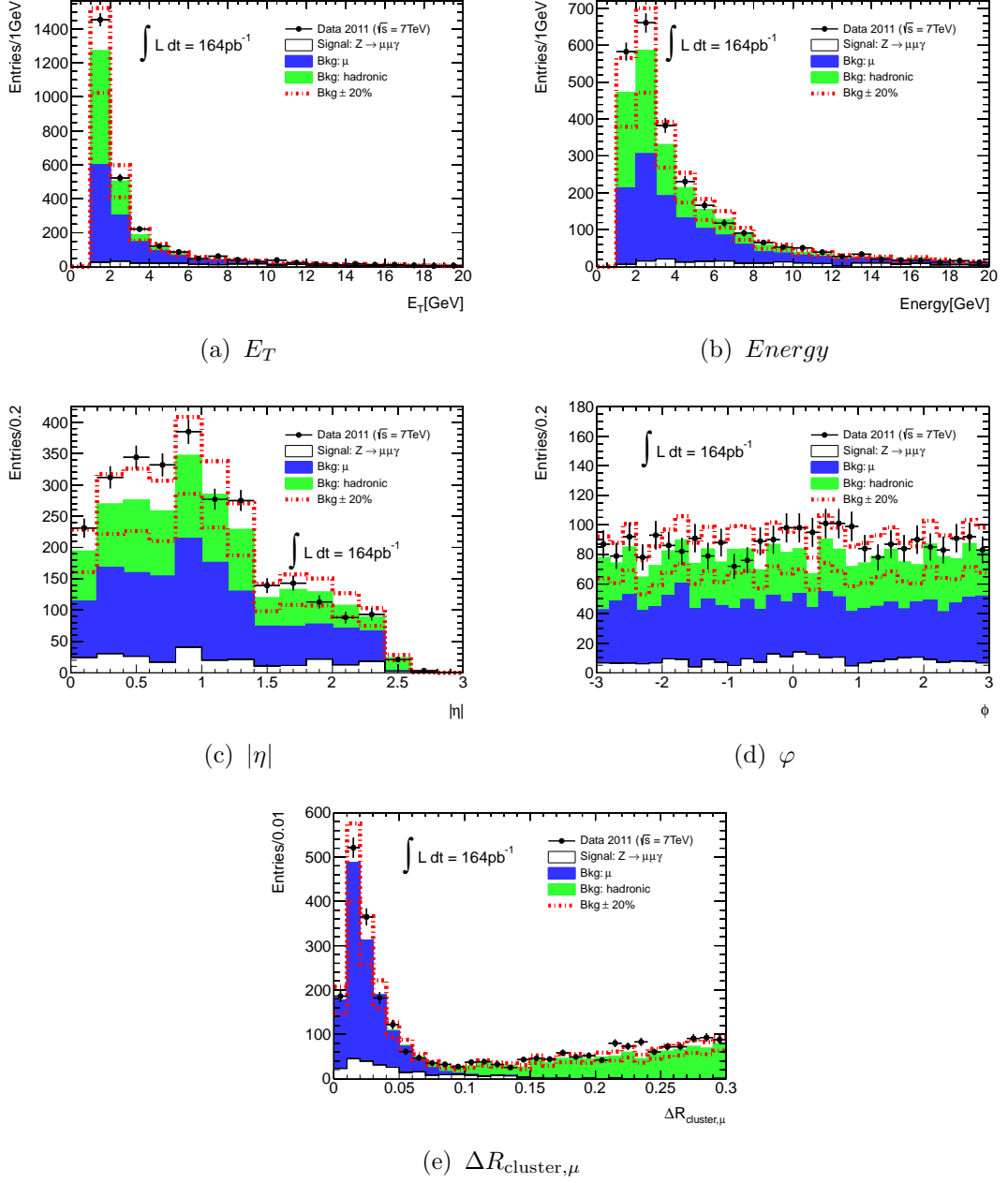


Figure 6.20: Control plots for the background normalization in a background-rich region defined by an $f_1 < 0.15$ cut inversion. The photon candidate transverse energy, energy, $|\eta|$, φ and $\Delta R_{\text{cluster},\mu}$ for events passing the inverted cut are shown for data and MC. As an example, an uncertainty band of $\pm 20\%$ for the background is also shown. Based on these studies a 20% uncertainty on the background normalization has been considered leading to a 7.6% uncertainty contribution to the predicted $Z \rightarrow \mu\mu\gamma$ yields.

Cut Description	Systematic Uncertainty
(Theory) Z geometrical acceptance	$\pm 3.8\%$
(Theory) PHOTOS	$\pm 0.2\%$
Z preselection [44]	$\pm 0.9\%$
$E_{T,\gamma}$ cut	$\pm 0.5\%$
$\Delta R_{\gamma,\mu}$ cut	$\pm 0.6\%$
f_1 cut	$\pm 1.0\%$
Background normalization	$\pm 7.6\%$
Total excluding luminosity	$\pm 8.6\%$
Luminosity	$\pm 3.4\%$

Table 6.17: Systematic Uncertainties.

6.7 Improvement of the Z invariant mass

Improving the Z invariant mass resolution and scale is an immediate application of the reconstructed FSR photons which also consists an independent check of the signal purity. Figure 6.21 shows the Z invariant mass only for the events which pass our final selection. The mass is shown before and after including the reconstructed FSR photons. The black dash-dotted line and circles represent the $\mu\mu$ invariant mass for data and MC, while the triangles show the $\mu\mu\gamma$ invariant mass. The MC after adding the FSR candidates is fitted with a Gaussian function, with a mean value of 91.31 ± 0.06 GeV. A clear improvement in resolution and scale is observed. In particular the low energy tail of the resonance is significantly suppressed. Even though the improvement shown here represents only the $\simeq 7\%$ of the inclusive $Z \rightarrow \mu\mu$, it does make a significant contribution to the Z-boson lineshape, because most of the corrected events are from the tail of the distribution.

An extra test was made to check the fraction of FSR multiple photon emission after final selection. Figures 6.22 and 6.23 show the Z invariant mass for events passing the final event selection, before/after the addition of the reconstructed photons. Signal events are shown in yellow (single photon emission) and blue (multiple photon emission). The data is denoted by triangles. Multiple emission here means that more than one true FSR photons ($E \gtrsim 500$ MeV) have been emitted from the same muon. This FSR multi-emission represents $\lesssim 5\%$ of the final reconstructed events. Notice that in the mass tail region (< 80 GeV), the final corrected $Z \rightarrow \mu\mu$ events are nearly pure $Z \rightarrow \mu\mu\gamma$ signal events. In Figure 6.24, the fraction of the corrected $Z \rightarrow \mu\mu\gamma$ signal events with respect to the total inclusive $Z \rightarrow \mu\mu$ events is shown,

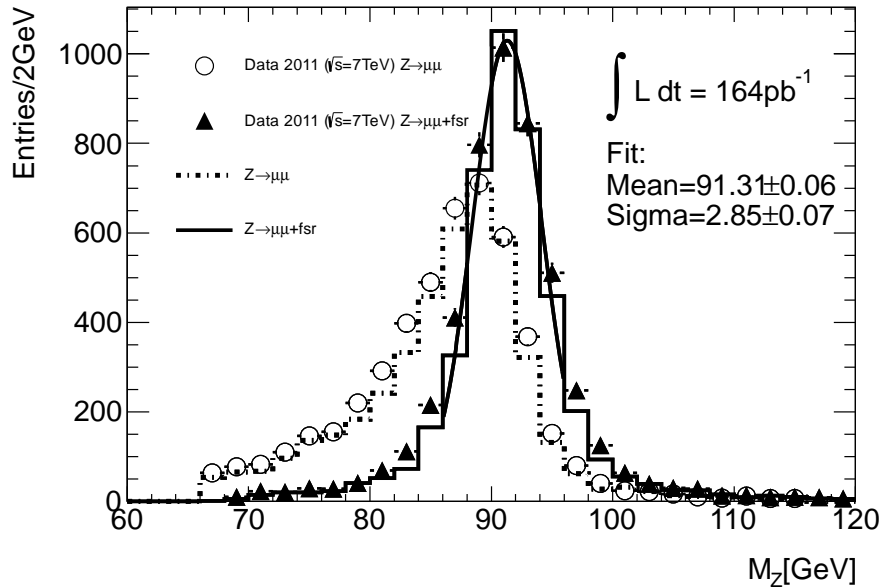


Figure 6.21: Z-boson invariant mass distribution for events passing the event selection, before and after the addition of the reconstructed candidate FSR photons.

as $\frac{N_{signal,Z \rightarrow \mu\mu\gamma}}{N_{Z \rightarrow \mu\mu}}$. It can be seen that in the original inclusive Z mass tail (< 80 GeV), 20% of the inclusive $Z \rightarrow \mu\mu$ are signal FSR events. This is to be compared with a $\sim 2\%$ -8% in the bulk of the invariant mass distribution. As a consequence, the tail of the Z invariant mass is significantly reduced by adding the reconstructed FSR photons. This improvement is summarized in Table 6.18 where the migration of signal $Z \rightarrow \mu\mu\gamma$ events from the tail to the bulk of the invariant mass is presented.

6.8 Pile-up effects and Monte Carlo reweighting

During the 2011 data taking, the LHC bunch trains had an inter-train bunch separation of 50 ns. In addition, due to the overlapping signals in the detector from other neighbouring bunch crossings, the out-of-time pile-up has to be taken into account. The Monte Carlo is provided before or during a given data taking period. Therefore, only a best-guess of the data pile-up conditions can be put into the MC. Thus, there is the need at the analysis level to reweight the MC pile-up conditions to what is found in the data.

M_Z [GeV]	<80	80-88	88-94 (peak region)	94-102	>102
Data					
before correction	829	1780	1620	287	77
after correction	147	783	2576	920	167
fraction of corrected events					
w.r.t. inclusive $Z \rightarrow \mu\mu$	20.5%	15.5%	4.1%	3.3%	5.9%
MC signal					
before correction	2030	3881	1868	291	121
after correction	220	1378	5263	1062	269

Table 6.18: Effect of adding the FSR photon to the invariant $Z \rightarrow \mu\mu$ mass as a function of the mass. A significant fraction ($\simeq 20\%$) of the inclusive $Z \rightarrow \mu\mu$ events are corrected in the tail of the distribution. These events (signal to the 90% level) are moved to the bulk of the invariant mass distribution, as shown in the last two rows using Monte Carlo.

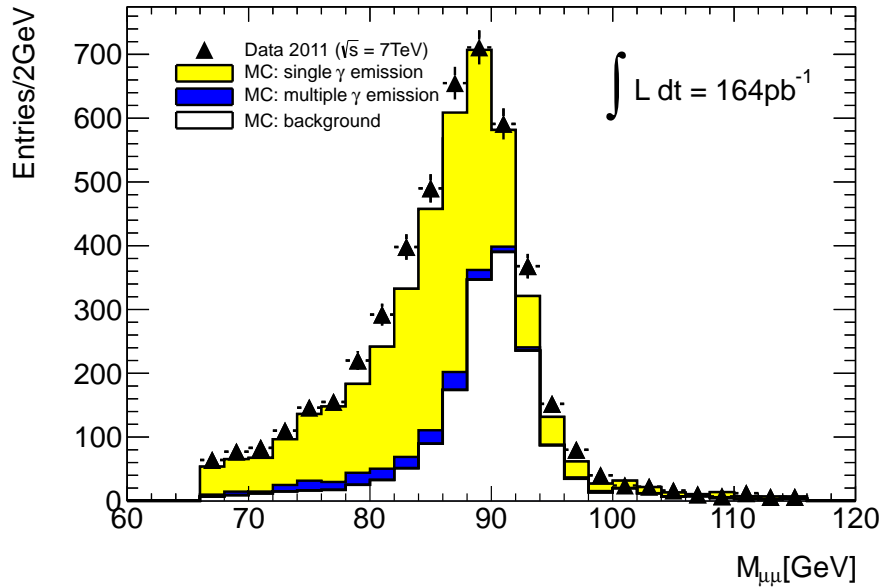


Figure 6.22: Z invariant mass distribution for events passing the event selection, before the addition of the reconstructed FSR photons, with signal shown in blue and yellow.

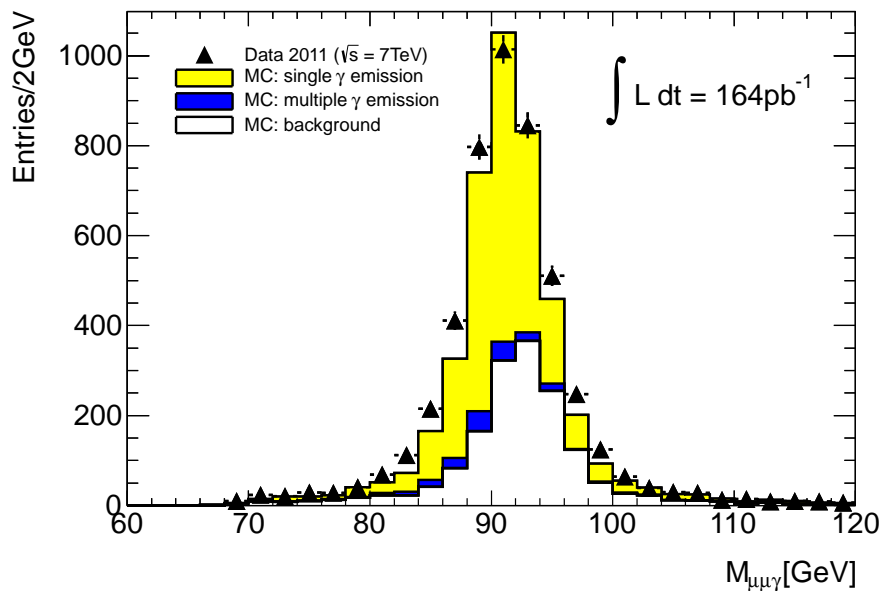


Figure 6.23: Z invariant mass distribution for events passing the event selection, after the addition of the reconstructed FSR photons, with signal shown in blue and yellow.

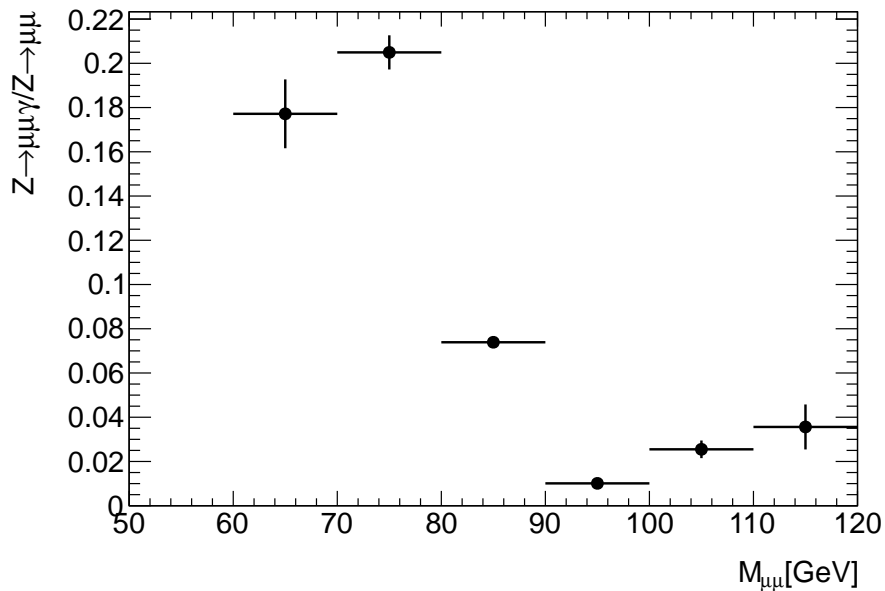


Figure 6.24: Fraction of corrected $Z \rightarrow \mu\mu\gamma$ signal events with respect to the total inclusive $Z \rightarrow \mu\mu$ events.

The very low energy reach of the EM topo-seeded clustering can be used to validate the pile-up reweighting performance and check the behaviour of the different background components around the neutral Z-boson muon line. A large cone $\Delta R_{\text{cluster},\mu} < 0.5$ is opened about the muon and the most energetic EM topo-seeded cluster is selected. The distribution of the $\Delta R_{\text{cluster},\mu}$ gives information on the activity around the muon. A very low transverse energy cut ($E_T > 1$ GeV) is applied on the cluster. This cut is sensitive to the description of the pile-up by the Monte Carlo: for lower transverse energy cut higher yields of EM topo-seeded clusters are expected. Figure 6.25 shows the $\Delta R_{\text{cluster},\mu}$ distribution in a linear and logarithmic scale before pile-up reweighting. The black points represent the data. The white histograms show the true FSR photons from $Z \rightarrow \mu\mu\gamma$ decays. The yellow histograms show the clusters mainly contributed by muon ionization. The green histograms show the clusters having pure hadronic origin (mainly $\pi_0 \rightarrow \gamma\gamma$). All clusters receive a contribution from pile-up. From this figure it is apparent that the MC without pile-up reweighting disagrees with the data, especially in the large ΔR region where the reconstructed clusters are fully dominated by hadronic background.

Pile-up leads to different vertex distributions in data and MC. To test the simulation performance without being affected by pile-up, the $\Delta R_{\text{cluster},\mu}$ distributions for a fixed number of pile-up vertices are plotted. Figure 6.26 and Figure 6.27 show the $\Delta R_{\text{cluster},\mu}$ distribution after a cluster $E_T > 1$ GeV cut, in linear and logarithmic scale, for events with 5 and 7 primary vertices respectively ($N_{PV} = 5$ and $N_{PV} = 7$). Data and MC agree when the same number of pile-up vertices is used. This implies that the MC simulation predicts well the behaviour in the data for a fixed number of vertices. The difference between MC and data in Figure 6.25 is thus expected to be due to the different distributions of the number of pile-up vertices between data and MC. This necessitates the procedure of pile-up reweighting. Figure 6.28 shows the $\Delta R_{\text{cluster},\mu}$ distribution after pile-up reweighting. A reasonable agreement between data and MC is now observed, demonstrating the good performance of the pile-up reweighting procedure. The agreement between data and MC persists for higher values of the E_T cut. This is shown in Figure 6.29, the $\Delta R_{\text{cluster},\mu}$ distribution after pile-up reweighting with $E_T > 3$ GeV transverse energy cut on the cluster.

6.9 Conclusions

A method for including the final state radiation photon in the reconstruction of Z bosons decaying into pairs of muons ($Z \rightarrow \mu\mu\gamma$) was presented. The method exploits the longitudinal segmentation of the ATLAS liquid argon calorimeter to reconstruct

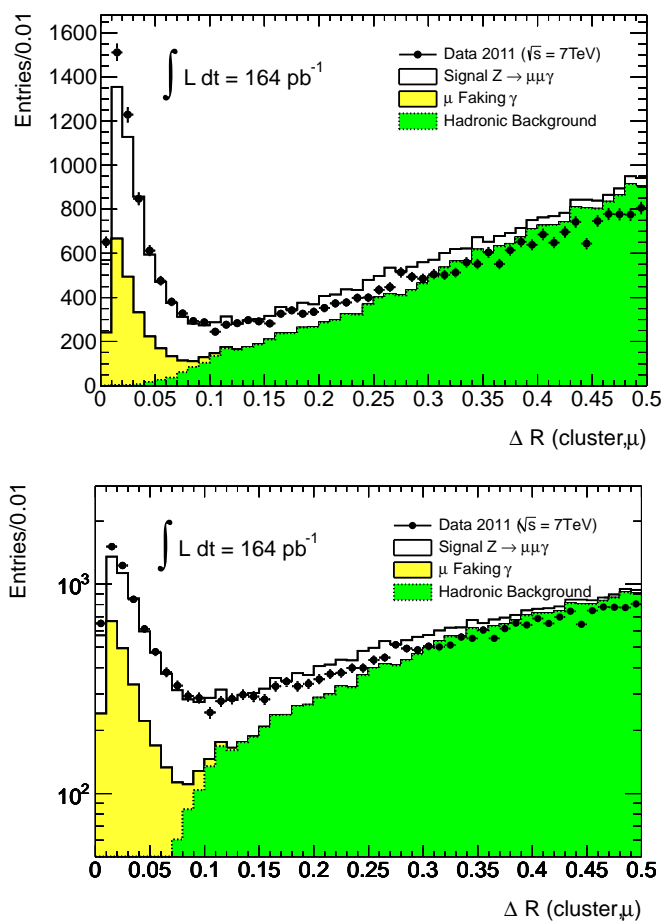


Figure 6.25: $\Delta R_{\text{cluster},\mu}$ distribution between the cluster and the closest muon ($E_T > 1$ GeV) in linear scale (top) and log scale (bottom) before pile-up reweighting.

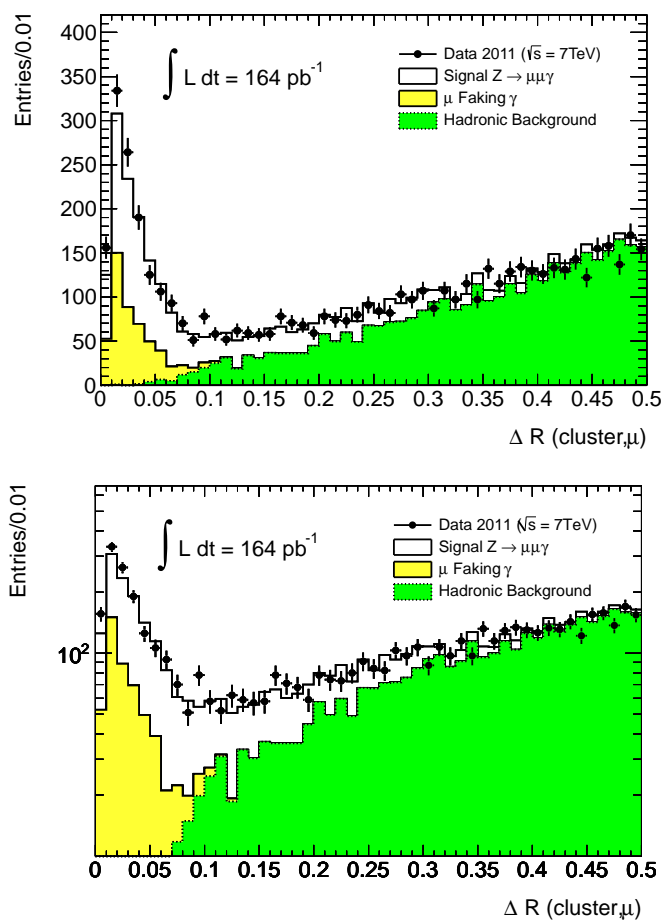


Figure 6.26: $\Delta R_{\text{cluster}, \mu}$ distribution between the cluster and the closest muon for fixed number of pile-up vertices ($N_{pv} = 5$) in linear scale (top) and log scale (bottom).

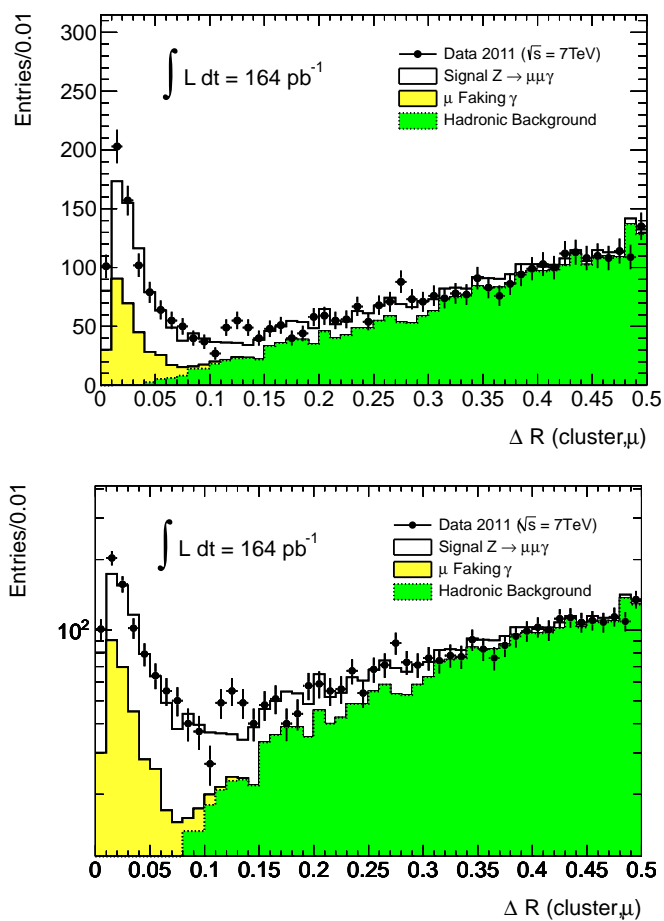


Figure 6.27: $\Delta R_{\text{cluster}, \mu}$ distribution between the cluster and the closest muon for fixed number of pile-up vertices ($N_{pv} = 7$) in linear scale (top) and log scale (bottom).

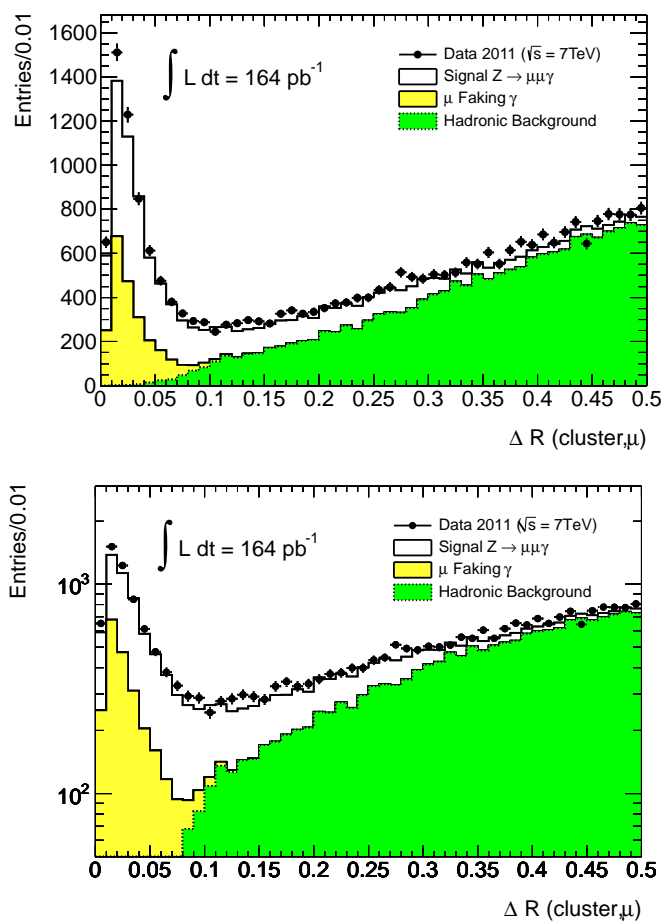


Figure 6.28: $\Delta R_{\text{cluster},\mu}$ distribution between the cluster and the closest muon ($E_T > 1$ GeV) in linear scale (top) and log scale (bottom) after pile-up reweighting.

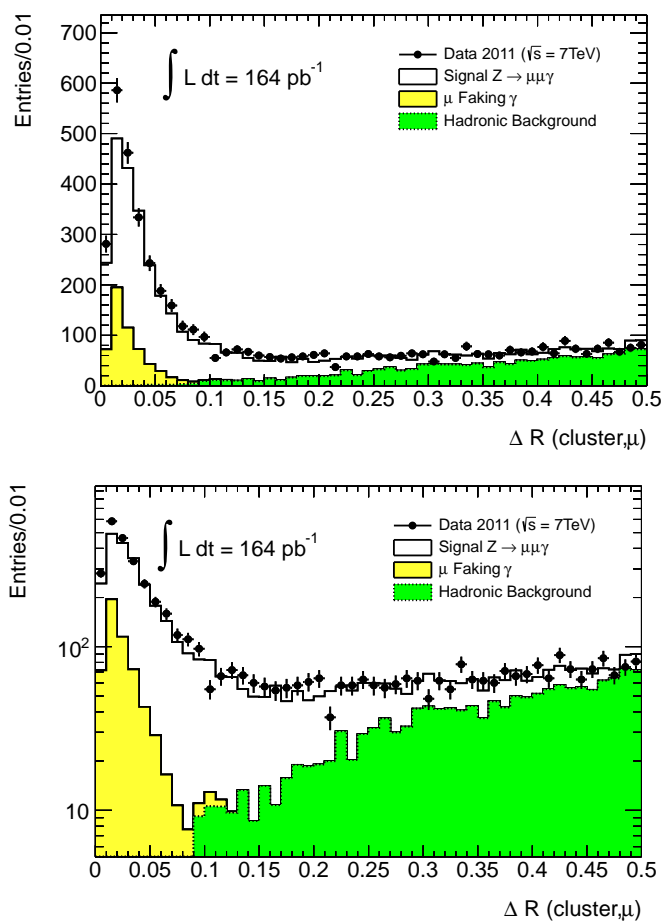


Figure 6.29: $\Delta R_{\text{cluster},\mu}$ distribution between the cluster and the closest muon ($E_T > 3 \text{ GeV}$) in linear scale (top) and log scale (bottom) after pile-up reweighting.

photons collinear with the muons emitted from the Z. An algorithm for the reconstruction of FSR photons was developed. The FSR candidates with $E_{T,\gamma} > 1.3$ GeV were reconstructed within a $\Delta R_{\gamma,\mu} < 0.15$ cone about the axis defined by the muon momentum direction at the interaction point, using the LAr calorimeter of ATLAS and a special clustering efficient at low energies. Based on an integrated luminosity of 164 pb^{-1} , the yield of Z events with at least one reconstructed FSR photon was measured as a function of the photon energy, transverse energy and pseudorapidity. The measured $Z \rightarrow \mu\mu\gamma$ yields were found to be consistent with the expectation from a NNLO QCD calculation including QED FSR. The measured $Z \rightarrow \mu\mu\gamma$ fiducial cross-section is presented: $\sigma_{Z \rightarrow \mu\mu\gamma}^{fid} = 0.073 \pm 0.001(\text{stat}) \pm 0.006(\text{sys}) \pm 0.002(\text{lum}) \text{ nb}$.

Photons within the ΔR and E_T fiducial region are reconstructed with a 70% average efficiency which increases to 85% for $E_T > 4$ GeV. Inclusion of these photons in the dimuon invariant mass calculation was shown to lead to improved Z-boson invariant mass resolution and scale: a Gaussian fit shows that the peak of the distribution moves from 89 GeV to 91.31 ± 0.06 GeV with a standard deviation of 2.5 ± 0.07 GeV. A $\simeq 20\%$ of all inclusive $Z \rightarrow \mu\mu$ events are corrected in the tail of the invariant mass ($M < 80$ GeV). These events are signal to the 90% level and migrate from the tail to the bulk of the distribution as shown in Table 6.18.

Chapter 7

Improving the invariant mass of Higgs $\rightarrow ZZ(^*) \rightarrow 4l(l = e, \mu)$ by adding FSR photons

7.1 Introduction

The search for the Standard Model Higgs boson is the major goal of the LHC. The decay channel Higgs $\rightarrow ZZ(^*) \rightarrow 4l(l = e, \mu)$ provides the cleanest experimental signature for the Higgs boson discovery, in the range between 130 GeV and 600 GeV [3]. However, the high mass region large tails have been observed in the m_{4l} invariant mass (Figure 7.1). One of the most important contribution to these tails is the omission of FSR photons. The QED FSR contribution is potentially larger in the electron channel, but the overall effect is in fact smaller than for the muon channel, since the nearby photons are automatically included in the electron cluster [4][5]. Currently, in the Higgs mass reconstruction, only four leptons are considered as the final state of the Higgs $\rightarrow ZZ(^*) \rightarrow 4l$. As described in Chapter 6, QED Final State Radiation photons from the Z leptonic decay can lead to a non-negligible FSR-induced distortion on the Z invariant mass. In the case of Higgs $\rightarrow ZZ(^*)$, the effect of distortion could be worse. Also, in the high Higgs mass region, the outgoing radiated photon can carry an even larger energy since the Z's can be boosted. By reconstructing and adding back the FSR photons to the invariant mass of Higgs, the energy resolution and scale of the m_H can be significantly improved.

This Chapter proposes a method for improving the Higgs $\rightarrow 4l$ mass resolution

by using the QED FSR photons obtained by the techniques presented in this thesis. The improvement of the Higgs invariant mass resolution and scale is presented.

7.2 Monte Carlo Samples

The Monte Carlo samples for the Higgs signal were generated using PYTHIA [57], including both the gluon fusion(ggF), $gg \rightarrow H$, and the vector boson fusion(VBF), $qq' \rightarrow qq' H$, production mechanisms. The PYTHIA generator is interfaced to PHOTOS [66] to include final-state radiation. The Higgs masses considered in this analysis range from 200 GeV to 360 GeV. The samples are summarised in Table 7.1.

Process	Dataset	Generator	Cross section(fb)	N_{evt}
$H[200] \rightarrow 4l$	116200	PYTHIA	3.9033	49949
$H[220] \rightarrow 4l$	116201	PYTHIA	7.5081	49953
$H[240] \rightarrow 4l$	116202	PYTHIA	6.6149	49948
$H[260] \rightarrow 4l$	116203	PYTHIA	5.7780	49951
$H[280] \rightarrow 4l$	116204	PYTHIA	5.0931	49946
$H[300] \rightarrow 4l$	116205	PYTHIA	4.5956	49944
$H[320] \rightarrow 4l$	116206	PYTHIA	4.2226	49941
$H[340] \rightarrow 4l$	116207	PYTHIA	4.0569	48949
$H[360] \rightarrow 4l$	116208	PYTHIA	3.9033	49944

Table 7.1: Monte Carlo samples used.

7.3 Analysis Overview

The strategy for the reconstruction of the Final State Radiation photons in the Higgs $\rightarrow ZZ(*) \rightarrow 4\mu$ decay is described in this section. Events are required to have at least four muons in pairs of opposite charge. Events passing the four muon selection are considered as the Higgs($\rightarrow ZZ(*) \rightarrow 4\mu$) candidates. For the selected events, around the neutral line from each muon, a FSR search is performed inside a ΔR cone of 0.3. The standard egamma container is used as the source of FSR candidates. If any reconstructed photon or electron is found inside the cone with a transverse energy of $E_T > 1$ GeV, the most energetic one is then picked as the reconstructed FSR candidate around the muon. At the generator level, the same cuts

on ΔR and E_T are applied for the FSR photons coming from $\text{Higgs} \rightarrow \text{ZZ}^* \rightarrow 4\mu$ decays. Therefore, the truth level FSR photons satisfying the selection criteria are kept to evaluate the performance of the method.

7.4 Results

The main goal of this study is the improvement of the $\text{Higgs} \rightarrow \text{ZZ}^* \rightarrow 4\mu$ mass resolution and scale. Figure 7.1 shows the $\text{Higgs} \rightarrow 4\mu$ mass distribution before and after adding the truth FSR photons, with the Higgs mass ranging from 200 GeV to 360 GeV. The black lines in the plots represent the Higgs mass obtained from the four reconstructed muons. The red lines show the Higgs mass when the true FSR photons are added. This is the best possible achievable improvement. A significant improvement in scale and resolution is observed after adding the FSR photons.

Figure 7.2 shows the $\text{Higgs} \rightarrow 4\mu$ mass distribution before and after adding the reconstructed FSR photons for different Higgs masses. The black lines are the same as the black ones in Figure 7.1, corresponding to the Higgs mass reconstructed by the four muons. The red lines represent the Higgs mass obtained when the reconstructed FSR photons are added. Comparing to the Higgs mass in Figure 7.1, the improvement using reconstructed photons is very similar. Figure 7.3 shows the improvement of the Higgs mass after addition of reconstructed FSR photons for the corrected events only. The long tails have been reduced dramatically after the mass correction. The improvement shown here represents the 20-26% of the total $\text{Higgs} \rightarrow 4\mu$ events.

Table 7.2 shows the number of $\text{Higgs} \rightarrow 4\mu$ events, with a mass within one σ around the central Higgs mass, before FSR correction, after adding Truth_{FSR} and after adding the reconstructed FSR. The fractional improvement is defined as

$$\frac{(Events_{aftercorrection} - Events_{beforecorrection})}{Events_{beforecorrection}} \quad (7.1)$$

The corresponding number of events within two σ around the central Higgs mass are shown in Table 7.3. After adding the reconstructed FSR photons, the average improvement of the number of high quality $\text{Higgs} \rightarrow 4\mu$ events within one σ around the central Higgs mass ($\sim 8.0\%$) is larger than the average improvement for the events within two σ ($\sim 6.5\%$). This also indicates the improvement of the Higgs mass resolution and scale after adding the FSR photons.

Improving the invariant mass of $Higgs \rightarrow ZZ() \rightarrow 4l(l = e, \mu)$ by adding FSR photons*

7.4. Results photons

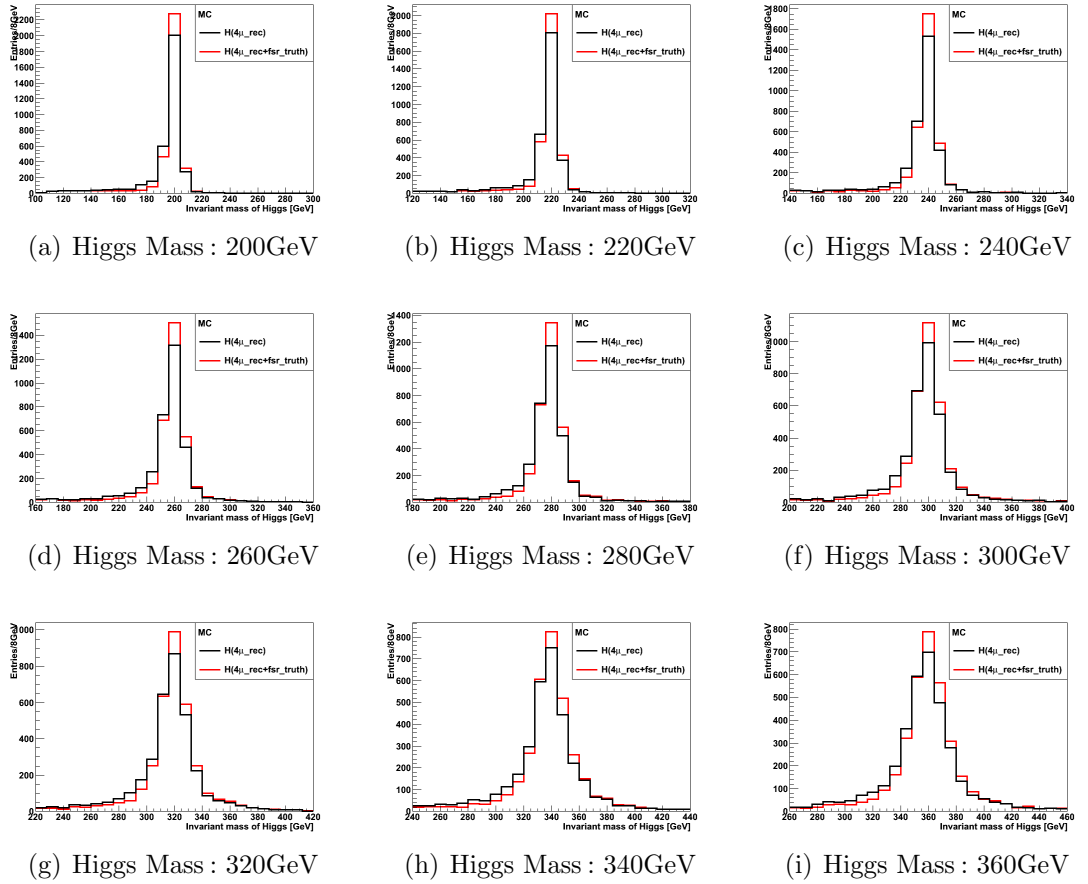


Figure 7.1: Higgs $\rightarrow 4\mu$ invariant mass distributions after addition of true FSR photons.

Improving the invariant mass of $Higgs \rightarrow ZZ() \rightarrow 4l(l = e, \mu)$ by adding FSR photons*

7.4. Results photons

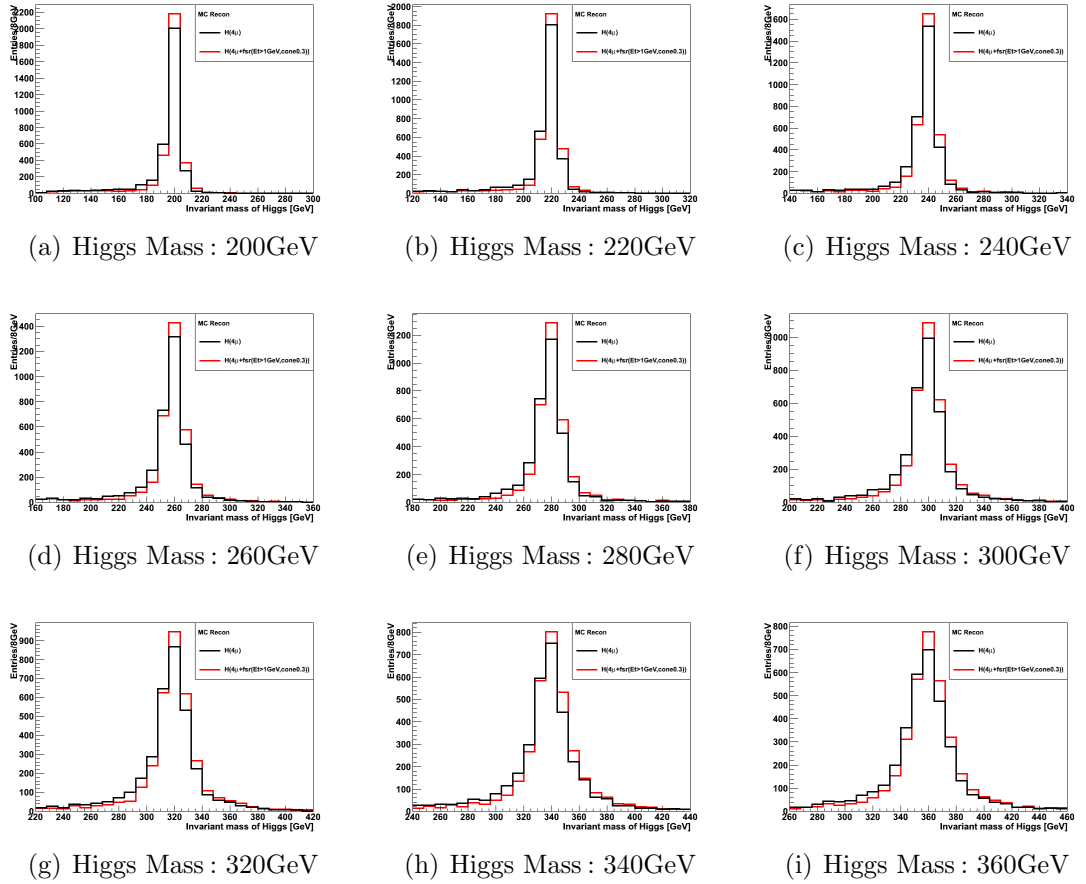


Figure 7.2: Higgs $\rightarrow 4\mu$ invariant mass distributions after addition of reconstructed FSR photons.

Improving the invariant mass of $Higgs \rightarrow ZZ() \rightarrow 4l(l = e, \mu)$ by adding FSR photons*

7.4. Results photons

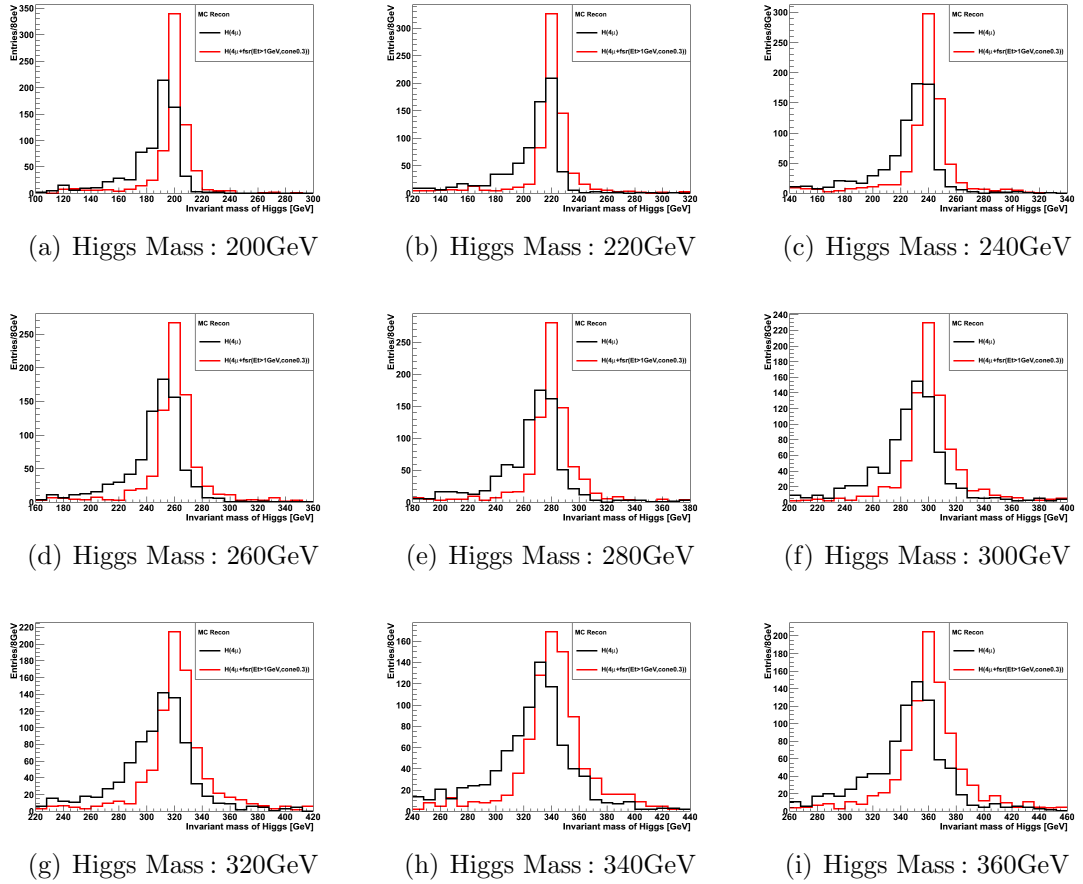


Figure 7.3: Higgs $\rightarrow 4\mu$ invariant mass distributions after addition of reconstructed FSR photons for the corrected events.

Number of Events within $[-\sigma, +\sigma]$ around central Higgs mass					
Process	Before correction	Adding Truth _{FSR}	Improvement (%)	Adding Recon _{FSR}	Improvement (%)
$H[200] \rightarrow 4\mu$	1678	1930	15.0	1830	9.1
$H[220] \rightarrow 4\mu$	1451	1655	14.1	1553	7.0
$H[240] \rightarrow 4\mu$	1535	1754	14.3	1652	7.6
$H[260] \rightarrow 4\mu$	1589	1797	13.1	1715	7.9
$H[280] \rightarrow 4\mu$	1614	1821	12.8	1765	9.4
$H[300] \rightarrow 4\mu$	1619	1800	11.2	1748	8.0
$H[320] \rightarrow 4\mu$	1697	1875	10.5	1841	8.5
$H[340] \rightarrow 4\mu$	1604	1755	9.4	1712	6.7
$H[360] \rightarrow 4\mu$	1768	1943	9.9	1912	8.1

Table 7.2: Number of events within $[-\sigma, +\sigma]$ around central Higgs mass.

Number of Events within $[-2\sigma, +2\sigma]$ around central Higgs mass					
Process	Before correction	Adding Truth _{FSR}	Improvement (%)	Adding Recon _{FSR}	Improvement (%)
$H[200] \rightarrow 4\mu$	2428	2705	11.4	2601	7.1
$H[220] \rightarrow 4\mu$	2279	2534	11.2	2432	6.7
$H[240] \rightarrow 4\mu$	2305	2566	11.3	2478	7.5
$H[260] \rightarrow 4\mu$	2357	2584	9.6	2526	7.2
$H[280] \rightarrow 4\mu$	2413	2638	9.3	2587	7.2
$H[300] \rightarrow 4\mu$	2395	2582	7.8	2545	6.3
$H[320] \rightarrow 4\mu$	2469	2632	6.6	2612	5.8
$H[340] \rightarrow 4\mu$	2308	2478	7.4	2455	6.4
$H[360] \rightarrow 4\mu$	2621	2776	5.9	2746	4.8

Table 7.3: Number of events within $[-2\sigma, +2\sigma]$ around central Higgs mass.

7.5 Conclusion

This chapter presents a method to reconstruct the final state radiation from Higgs $\rightarrow 4\mu$. The simulation study has shown the long tails in the Higgs invariant mass can be reduced by adding the reconstructed FSR photons. It is now being included in the official 4-lepton search and is expected to give a significant contribution to the Higgs search. A dedicated FSR tool has been developed at D3PD level for users to obtain the FSR photons around a given muon. The method and the usage of the tool are introduced in Appendix B.

Chapter 8

Summary

The measurement of the QED Final State Photon Radiation (FSR) from Z and W boson leptonic decays is necessary for controlling QED radiative corrections in W/Z boson cross-section predictions. In the process of muon pair production, the shape of the Z resonance peak obtained from measuring the invariant mass distribution of the $\mu^+\mu^-$ pair is significantly affected by the FSR loss, due to the fact that events belonging to the Z pole are shifted to the low mass region [45]. In the case of resonance pair production, mass distortion effects can arise: e.g. in the search for a Higgs $\rightarrow ZZ^*$ at high masses, long tails in the 4-lepton invariant mass can be observed for muons in the final state. The deterioration of the 4-lepton resolution leads to a reduced sensitivity to the Higgs signal.

This thesis introduces a method for including the QED FSR photons in the reconstruction of Z bosons decaying into pairs of muons ($Z \rightarrow \mu\mu\gamma$). FSR photons emitted with very small angles (e.g. collinear) with respect to muons from $Z \rightarrow \mu\mu$ decays can be reconstructed with the ATLAS LAr EM calorimeter. A special top-seeded clustering is used in the FSR reconstruction for its excellent capability in identifying low-energy deposition patterns in the EM calorimeter. The longitudinal segmentation of the EM calorimeter is exploited to reduce fake photon clusters produced by muon energy loss in the calorimeter. Based on an integrated luminosity of 164 pb^{-1} , the cross-section of the $Z \rightarrow \mu\mu\gamma$ process with at least one FSR photon within the fiducial region ($E_{T,\gamma} > 1.3 \text{ GeV}, \Delta R_{\gamma,\mu} < 0.15$) was measured:

$$\sigma_{Z \rightarrow \mu\mu\gamma}^{fid} = 0.073 \pm 0.001(\text{stat}) \pm 0.006(\text{sys}) \pm 0.002(\text{lum}) \text{ nb}, \quad (8.1)$$

which is consistent with the expectation from a NNLO QCD calculation including QED FSR.

An advantage of this analysis is the usage of the special topo-seeded clustering. This is particularly useful for low energy photon reconstruction and can also be used to validate the pile-up reweighting in ATLAS. A test has been performed in this thesis, showing a good agreement between data and MC after pile-up reweighting.

Another advantage of this analysis is the possibility of verifying the signal purity by comparing the improvement of the $Z \rightarrow \mu\mu$ invariant mass resolution with the expected improvement from Monte Carlo. The presence of an excess of fake clusters in the data with respect to MC would distort the $Z \rightarrow \mu\mu\gamma$ invariant mass. The level of agreement between data and MC constrains the value of the purity, usually extracted from MC. The signal purity of the reconstructed FSR photons improves dramatically at high photon E_T . A dedicated tool [119] to search for FSR photons around a reconstructed muon has been requested by ATLAS users. This is now an official part of the ATLAS offline software package. With the increasing luminosity at LHC, the tool can search for high E_T FSR photons with very high purity, which can be further useful for the extraction of electron/photon efficiency scale factors, photon energy calibration studies, etc. A good control of the final state radiation is also crucial in searches for anomalous three body Z decays into a photon and a pair of leptons, for which FSR photons are the main source of background [120]. Those potential measurements are expected to be exploited in the future.

Finally, inclusion of FSR photons in the dimuon invariant mass calculation leads to improved Z-boson invariant mass resolution and scale, observed both in data and MC. These improvements are important in the Higgs $\rightarrow ZZ^{(*)} \rightarrow 4\ell$ search, since two Z-bosons are involved. Based on MC Higgs $\rightarrow ZZ^{(*)} \rightarrow 4\mu$ studies, more than 20% of the events are expected to have a reconstructed FSR photon. In this thesis the improvements of the Higgs invariant mass resolution and scale by adding the reconstructed FSR photons were presented.

Appendix A

Monte Carlo Event Generator

PHOTOS	A universal Monte Carlo algorithm simulating the effects of QED radiative corrections in decays of particles and resonances. More details can be found in Chapter 3.
TAUOLA	A library of Monte Carlo programs for leptonic and semileptonic decays of τ leptons.
PHOJET	A generator suited for minimum bias processes (double-, semi- and non-diffractive).

Table A.1: Specific purpose generators.

MC@NLO	A Fortran package for combining a Monte Carlo event generator with NLO calculations for QCD processes. A key ingredient is the use of a modified subtraction method for dealing with infrared and collinear singularities.
POWHEG	The Positive Weight Hardest Emission Generator implements NLO calculations in shower Monte Carlo programs. The method provides the inclusion of NLO corrections with angular ordering, thus avoiding the problem of negative weighted event.
ALPGEN	A generator for hard multi-parton process in hadronic collisions. It allows complete and accurate studies of SM backgrounds to a large fraction of the most interesting new physics phenomena accessible at the LHC.

Table A.2: Parton level generators.

PYTHIA	Multi-purpose Leading Order Generator. Pythia 8 is the successor to Pythia 6, representing a complete rewrite in C++. More details can be found in Chapter 3.
HERWIG++	Multi-purpose Leading Order Generator. HERWIG++ is written in C++ with many modifications and improvements on Fortran HERWIG (A package for simulating Hadron Emission Reactions With Interfering Gluons). It includes the simulation of hard lepton-lepton, lepton-hadron and hadron-hadron collisions. A number of important hard scatterings are available, with specialized matrix element generators for additional processes. The simulation of Beyond the Standard Model physics includes a range of models and allows new models to be added by encoding the Feynman rules. The parton-shower approach is used to simulate initial- and final-state QCD radiation, including colour coherence effects, with special emphasis on the correct description of radiation from heavy particles. The underlying event is simulated using an eikonal multiple parton-parton scattering model. The formation of hadrons is described by the cluster-hadronization model. Hadron decays are simulated using matrix elements, where possible including spin correlations and off-shell effects.
SHERPA	A multi-parton generator for the Simulation of High-Energy Reactions of PArticles in lepton-lepton, lepton-photon, photon-photon, lepton-hadron and hadron-hadron collisions. It contains a flexible tree-level matrix-element generator for the calculation of hard scattering processes within and beyond the SM. The additional initial- and final- states QCD radiation is described by parton-shower. To consistently combine multi-parton matrix elements with the QCD parton cascades the Catani-Krauss-Kuhn-Webber approach is employed. A simple model of multiple interactions is used for underlying events. The fragmentation is described using the cluster-hadronisation model. A library is provided for simulating tau-lepton and hadron decays. Available form-factor models and matrix elements are used to include spin correlations. Effects of virtual and real QED corrections are included using the approach of Yennie-Frautschi-Suura.

Table A.3: Full generators.

Appendix B

FSR Tool

The FSR Tool [119] returns a list of candidate Final State Radiation photons found within a cone about the muon neutral line defined by the muon momentum at the perigee. The first version of the tool was intended for use at the D3PD level (D3PD is a common ATLAS analysis data-file format). The tool is now part of the ATLAS software package *egammaAnalysisUtils*. The FSR photon candidates are required to be inside a ΔR cone around the muon neutral line, to pass the E_T and the $f_1 (= E_{strip}/E_{cluster})$ cuts. By using the f_1 cut the longitudinal segmentation of the LAr calorimeter is exploited. This cut is effective for low energy photons where a large fraction of the EM energy is deposited in the strip section of the calorimeter. The f_1 cut helps in discriminating against background induced by the muon itself via ionization producing low energy clusters. A muon energy deposition follows the Landau distribution with a mean energy of 300 ± 50 MeV. Landau fluctuations may lead to a small fraction of higher energy clusters passing the cluster energy threshold of $E_T > 1.3$ GeV used in this thesis. These clusters have typically small $f_1 < 0.15$.

The tool operates in a way similar to the analysis discussed in Chapter 6. There are two main differences: (i) the tool returns all available FSR candidates satisfying the selection criteria, allowing users to decide on particular further selection criteria; (ii) due to the fact that the EM topo-seeded clustering overlaps with the standard sliding-window egamma clustering at high energy, only topo-seeded photons with transverse energies between 1-10 GeV are stored in the D3PD. Thus, when calling the tool, FSR photon candidates can be obtained from any of the three egamma categories:

- EM topo-seeded photons for E_T above the required threshold and below 3.5

GeV. These are photons used by π^0 analyses and the FSR analysis in Chapter 6. TopoSeededPhotons are efficient for low energy photon reconstruction (down to 1 GeV). They are overlapping with standard egamma Photons in the transverse energy 3-10 GeV in D3PD. Thus, in this analysis, Standard Egamma Photons are used for $E_T > 3.5$ GeV. EM topo-seeded photons are used only for very low energies $E_T < 3.5$ GeV.

- Standard egamma photons when $E_T > \text{Max}(\text{the required threshold}, 3.5 \text{ GeV})$.
- Standard egamma electrons when E_T is above the required threshold. The reason to look for candidates in the electron collection is due to the muon-track photon-cluster matching in egamma: the reconstruction software consider all inner detector tracks that match LAr EM clusters as electron candidates.

The threshold of the three cuts ($\Delta R < dR_{CUT}$, $E_T > Et_{CUT}$, $f_1 > f1_{CUT}$) can be set by the users in the tool argument list. By default, $dR_{CUT} = 0.3$, $Et_{CUT} = 1000.0$ (1 GeV), $f1_{CUT} = 0.15$. Also, the users will pass the muon, photon, electron information in the argument list. Note that for high energies the f_1 cut may be lowered (e.g. 0.0005). Studies involving photon or EM shapes should consider potential biases from applying this cut. The tool will return a list of FSR candidates, from which the user can retrieve the container name (photon or electron), the index of this candidate in its container, and the ΔR between the candidate and the muon.

Conversion Issues: Note that the case of conversions has not been studied in detail. However for very low photon energies an early conversion is expected to be swept away by the B-field.

Calibration Issues: Note that all clusters in the categories above are calibrated. However, the user should consider that when the muon itself passes through the cluster, it adds a small amount of energy to the true photon deposition. Studies have shown that a removal of an average energy of 300 MeV gives reasonable linearity (2% for 1-10 GeV using topo-seeded photons, see Chapter 6). This correction is not applied by the tool.

An example of a use-case of the tool is presented here. The Z boson invariant mass for events for which at least one FSR photon was found, before and after the addition of the reconstructed photons (with E_T above 4 or 10 GeV), using 2011 data from period B to period K, is shown in Figure B.1 and Figure B.2. Three parameters set in the tool argument list are $dR_{CUT} = 0.15$, $Et_{CUT} = 4000$ or 10000 (4 or 10 GeV), $f1_{CUT} = 0.15$. The significant improvement in the invariant mass confirms the high purity of the selected photon samples, which allow for further applications

of these photons in performance studies (e.g. extraction of egamma scale factors, photon energy uniformity measurements).

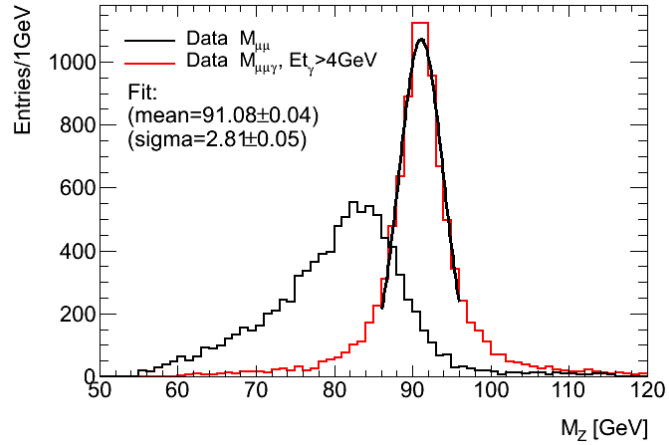


Figure B.1: Z boson invariant mass for events for which at least one FSR photon was found, before and after the addition of the reconstructed photons (with $E_T > 4$ GeV), using 2011 data from period B to period K.

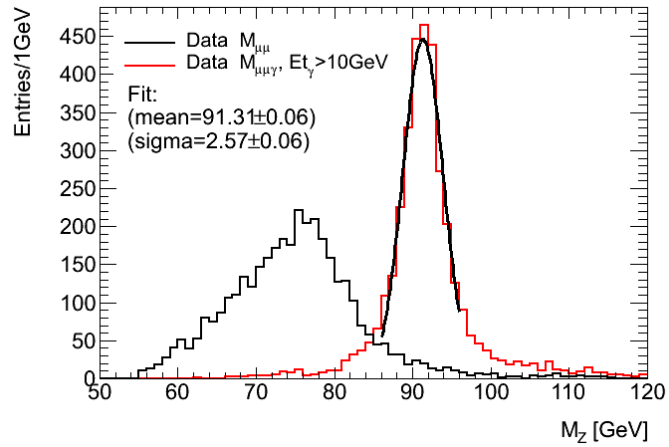


Figure B.2: Z boson invariant mass for events for which at least one FSR photon was found, before and after the addition of the reconstructed photons (with $E_T > 10$ GeV), using 2011 data from period B to period K.

Bibliography

- [1] M. G. Albrow, *QCD in hadron-hadron collisions*, Fermi National Accelerator Laboratory .
- [2] W. Beenakker, F. Berends, and A. Chapovsky, *Final-state radiation and line-shape distortion in resonance pair production*, Phys. Lett. **B435** (1998) 233–239.
- [3] D. Rebutzi, *Search for the higgs boson in the channel $H \rightarrow ZZ^* \rightarrow 4l$ with the ATLAS detector*, ATLAS internal note: ATL-PHYS-INT-2009-127.
- [4] L. Poggioli, *$H \rightarrow ZZ^* \rightarrow 4\text{leptons}$. A comparison of ATLAS and CMS potentials*, ATLAS internal note: PHYS-NO-066, 1995.
- [5] O. Linossier and L. Poggioli, *Final state inner-bremsstrahlung effects on $H^0 \rightarrow ZZ^* \rightarrow 4l$ channel with ATLAS*, ATLAS internal note: PHYS-NO-075, 1995.
- [6] F. Halzen and A. D. Martin, *Quarks and leptons: an introductory course in modern particle physics*, p. 396. New York, US, 1984.
- [7] B. Povh, K. Rith, C. Scholz, and F. Zetsche, *Particles and Nuclei*. Addison-Wesley, Reading, Massachusetts, 1995.
- [8] K. Nakamura et al., *Review of Particle Physics*, J. Phys. **G37** (2010) 075021.
- [9] S. L. Glashow, *Partial Symmetries of Weak Interactions*, Nucl. Phys. **22** (1961) 579–588.
- [10] A. Salam, *Elementary Particle Theory*, p. 367. Almqvist and Wiksell, Stockholm, 1968.
- [11] S. Weinberg, *A Model of Leptons*, Phys. Rev. Lett. **19** (1967) 1264–1266.
- [12] D. Griffiths, *Introduction to elementary particles*, p. 454. Weinheim, US, 2008.

- [13] P. Higgs, *Broken symmetries and the masses of gauge bosons*, Phys. Rev. Lett. **13** (1964) 508–509.
- [14] CDF and D0 Collaboration, *Combined CDF and D0 Upper Limits on Standard Model Higgs-Boson Production with 2.1 - 5.4 fb⁻¹ of Data*, arXiv:0911.3930v1 [hep-ex].
- [15] M. Spira et al., *Concepts of Electroweak Symmetry Breaking and Higgs Physics*, arXiv:0712.2419 [hep-ph].
- [16] T. Junk, *Confidence level computation for combining searches with small statistics*, Nucl. Instrum. Meth. **A434** (1999) 435.
- [17] R. Barate et al., *Search for the standard model Higgs boson at LEP*, Phys. Lett. **B565** (2003) 61–75.
- [18] ATLAS Collaboration, *Combined search for the Standard Model Higgs boson using up to 4.9 fb⁻¹ of pp collision data at $\sqrt{s} = 7$ TeV with the ATLAS detector at the LHC*, CERN-PH-EP-2012-019. arXiv:1202.1408v2 [hep-ex].
- [19] S. D. Drell and T.-M. Yan, *Massive lepton-pair production in hadron-hadron collisions at high energies*, Phys. Rev. Lett. **25** (1970) no. 5, 316.
- [20] J. M. Campbell, J. W. Huston, and W. J. Stirling, *Hard Interactions of Quarks and Gluons: A Primer for LHC Physics*, Rept. Prog. Phys. **70** (2007) 89, arXiv:hep-ph/0611148v1.
- [21] G. Altarelli and G. Parisi, *Asymptotic Freedom in Parton Language*, Nucl. Phys. **B126** (1977) 298.
- [22] P. M. Nadolsky et al., *Implications of CTEQ global analysis for collider observables*, Phys. Rev. **D78** (2008) 013004, arXiv:0802.0007 [hep-ph].
- [23] H. L. Lai et al., *New parton distributions for collider physics*, Phys. Rev. **D82** (2010) 074024, arXiv:1007.2241 [hep-ph].
- [24] A. D. Martin, W. J. Stirling, R. S. Thorne, and G. Watt, *Parton distributions for the LHC*, Eur. Phys. J. **C63** (2009) 189, arXiv:0901.0002 [hep-ph].
- [25] S. Alekhin, J. Blumlein, S. Klein, and S. Moch, *The 3-, 4-, and 5-flavor NNLO Parton from Deep-Inelastic-Scattering Data and at Hadron Colliders*, Phys. Rev. **D81** (2010) 014032, arXiv:0908.2766 [hep-ph].

- [26] P. Jimenez-Delgado and E. Reya, *Dynamical NNLO parton distributions*, Phys. Rev. **D79** (2009) 074023, arXiv:0810.4274 [hep-ph].
- [27] H1 and ZEUS Collaboration, F. D. Aaron et al., *Combined Measurement and QCD Analysis of the Inclusive ep Scattering Cross Sections at HERA*, JHEP **01** (2010) 109, arXiv:0911.0884 [hep-ex].
- [28] H1 and ZEUS Collaboration, V. Radescu, *HERA Precision Measurements and Impact for LHC Predictions*, arXiv:1107.4193 [hep-ex].
- [29] R. D. Ball et al., *Impact of Heavy Quark Masses on Parton Distributions and LHC Phenomenology*, Nucl. Phys. **B849** (2011) 296, arXiv:1101.1300 [hep-ph].
- [30] R. D. Ball et al., *A first unbiased global NLO determination of parton distributions and their uncertainties*, Nucl. Phys. **B838** (2010) 136, arXiv:1002.4407 [hep-ph].
- [31] J. M. Butterworth et al., *Single Boson and Diboson Production Cross Sections in pp Collisions at $\sqrt{s} = 7$ TeV*, ATLAS internal communication: ATL-COM-PHYS-2010-695.
- [32] I. R. Kenyon, *The Drell-Yan process*, Rep. Prog. Phys. **45** (1982) 1261.
- [33] M. Aharrouche et al., *Double differential Z,W cross sections and their ratios in the electron channels*, ATLAS internal note: ATL-PHYS-INT-2011-081.
- [34] H. D. Politzer, *Gluon corrections to Drell-Yan processes*, Nucl. Phys. **129** (1977) 301.
- [35] C. Sachrajda, *Lepton pair production and the Drell-Yan formula in QCD*, Phys. Lett. **73B** (1978) 185.
- [36] D. Amati, R. Petronzio, and G. Veneziano, *Relating hard QCD processes through universality of mass singularities*, Nucl. Phys. **B140** (1978) 54.
- [37] D. Amati, R. Petronzio, and G. Veneziano, *Relating hard QCD processes through universality of mass singularities(II)*, Nucl. Phys. **B146** (1978) 29.
- [38] S. Frixione and B. R. Webber, *Matching NLO QCD computations and parton shower simulations*, JHEP **06** (2002) 029, arXiv:0204244 [hep-ph].
- [39] J. M. Campbell and R. K. Ellis, *An update on vector boson pair production at hadron colliders*, Phys. Rev. **D60** (1999) 113006, arXiv:9905386 [hep-ph].

- [40] C. Anastasiou, L. Dixon, K. Melnikov, and F. Petriello, *High precision QCD at hadron colliders: Electroweak gauge boson rapidity distributions at NNLO*, Phys. Rev. **D69** (2004) 094008, arXiv:0312266 [hep-ph].
- [41] R. Hamberg, W. L. van Neerven, and T. Matsuura, *A Complete calculation of the order α_s^2 correction to the Drell-Yan K factor*, Nucl. Phys. **B359** (1991) 343.
- [42] T. Binoth, M. Ciccolini, N. Kauer, and M. Kramer, *Gluon-induced W-boson pair production at the LHC*, JHEP **12** (2006) 046.
- [43] T. Binoth, N. Kauer, and P. Mertsch, *Gluon-induced QCD corrections to $pp \rightarrow ZZ \rightarrow \ell\bar{\ell}'\bar{\ell}'$* , arXiv:0807.0024.
- [44] ATLAS Collaboration, *Measurement of the inclusive W^\pm and Z/γ^* cross sections in the e and μ decay channels in pp collisions at $\sqrt{s} = 7\text{TeV}$ with the ATLAS detector*, arXiv:1109.5141v3 [hep-ex].
- [45] S. Dittmaier and M. Huber, *Radiative corrections to the neutral-current Drell-Yan process in the Standard Model and its minimal supersymmetric extension*, arXiv:0911.2329v2 [hep-ph].
- [46] S. Dittmaier and A. Kaiser, *Photonic and QCD radiative corrections to Higgs-boson production in $\mu^+\mu^- \rightarrow f\bar{f}$* , arXiv:0203120v1 [hep-ph].
- [47] T. Kinoshita, *Mass singularities of feynman amplitudes*, J. Math. Phys. **3** (1962) 650.
- [48] T. D. Lee and M. Nauenberg, *Degenerate systems and mass singularities*, Phys. Rev. **133** (1964) 1549.
- [49] N. Nakanishi, *General theory of infrared divergence*, Progr. Theor. Phys. **19** (1958) 159.
- [50] C. Buttar et al., *Standard Model Handles and Candles Working Group: Tools and Jets Summary Report*, arXiv:0803.0678v1 [hep-ph].
- [51] C. M. C. Calame, G. Montagna, O. Nicrosini, and M. Treccani, *Multiple photon corrections to the neutral-current Drell-Yan process*, JHEP **0505** (2005) 019, arXiv:0502218v1 [hep-ph].
- [52] A. Andonov et al., *SANCScope – v.1.00*, Comput. Phys. Commun. **174** (2006) 481, arXiv:0411186 [hep-ph].

- [53] D. Bardin et al., *SANCnews: Sector $f\bar{f}b\bar{b}$* , Comput. Phys. Commun. **177** (2007) 738, [arXiv:0506120 \[hep-ph\]](#).
- [54] U. Baur, O. Brein, W. Hollik, C. Schappacher, and D. Wackerroth, *Electroweak Radiative Corrections to Neutral-Current Drell-Yan Processes at Hadron Colliders*, Phys. Rev. **D65** (2002) 033007, [arXiv:0108274 \[hep-ph\]](#).
- [55] P. Ciafaloni and D. Comelli, *Sudakov effects in electroweak corrections*, [arXiv:9809321v2 \[hep-ph\]](#).
- [56] F. Siegert, *Monte-Carlo event generation for the LHC*. PhD thesis, Durham University, 2010. <http://etheses.dur.ac.uk/484/>.
- [57] T. Sjostrand, S. Mrenna, and P. Skands, *PYTHIA 6.4 physics and manual*, JHEP **05** (2006) 026.
- [58] T. Sjostrand, S. Mrenna, and P. Skands, *A Brief Introduction to PYTHIA 8.1*, [arXiv:0710.3820v1 \[hep-ph\]](#).
- [59] G. Corcella et al., *HERWIG 6: an event generator for hadron emission reactions with interfering gluons*, JHEP **01** (2001) 010.
- [60] M. Bahr et al., *Herwig++ Physics and Manual*, [arXiv:0803.0883v3 \[hep-ph\]](#).
- [61] P. Bartalini et al., *Multi-Parton Interactions at the LHC*, [arXiv:1111.0469v2 \[hep-ex\]](#).
- [62] ATLAS internal website about AthenaFramework: <https://twiki.cern.ch/twiki/bin/viewauth/Atlas/AthenaFramework>.
- [63] M. Dobbs and J. Hansen, *The HepMC C++ Monte Carlo event record for High Energy Physics*, Comput. Phys. Commun. **134** (2001) 41.
- [64] C. Ay et al., *Monte Carlo Generators in ATLAS software*, J. Phys. **219** (2010) 032001.
- [65] T. Gleisberg et al., *Event generation with SHERPA 1.1*, [arXiv:0811.4622v1 \[hep-ph\]](#).
- [66] P. Golonka and Z. Was, *PHOTOS Monte Carlo: a precision tool for QED corrections in Z and W decays*, Eur. Phys. J. **C45** (2006) 97, [arXiv:0506026v2 \[hep-ph\]](#).

- [67] S. Jadach, J. H. Kuhn, and Z. Was, *TAUOLA - a library of Monte Carlo programs to simulate decays of polarized τ leptons*, *Comp. Phys. Commun.* **64** (1991) 275.
- [68] F. W. Bopp, R. Engel, and J. Ranft, *Rapidity gaps and the PHOJET Monte Carlo*, [arXiv:9803437v1](https://arxiv.org/abs/9803437v1) [[hep-ph](#)].
- [69] S. Frixione, P. Nason, and C. Oleari, *Matching NLO QCD computations with Parton Shower simulations: the POWHEG method*, *JHEP* **11** (2007) 070, [arXiv:0709.2092](https://arxiv.org/abs/0709.2092) [[hep-ph](#)].
- [70] M. L. Mangano, *ALPGEN, a generator for hard multiparton processes in hadronic collisions*, *JHEP* **07** (2003) 001.
- [71] M. R. Whalley, D. Bourilkov, and R. C. Group, *The Les Houches Accord PDFs (LHAPDF) and Lhaglu*, [arXiv:0508110v1](https://arxiv.org/abs/0508110v1) [[hep-ph](#)].
- [72] W. M. Yao et al., *Review of Particle Physics*, *J. Phys.* **G33** (2006) 1.
- [73] ATLAS Collaboration, *New ATLAS event generator tunes to 2010 data*, ATLAS note: ATL-PHYS-PUB-2011-008.
- [74] A. Sherstnev and R. Thorne, *Different PDF approximations useful for LO Monte Carlo generators*, [arXiv:0807.2132](https://arxiv.org/abs/0807.2132) [[hep-ph](#)].
- [75] ATLAS Collaboration, *ATLAS tunes of PYTHIA6 and PYTHIA8 for MC11*, ATLAS note: ATL-PHYS-PUB-2011-009.
- [76] Z. Was, *Bremsstrahlung, electroweak corrections τ -leptons in Z, W production and decays at LHC*, 2011. <http://wasm.web.cern.ch/wasm/talks.html>.
- [77] Z. Was. Bremsstrahlung in Z and W decays: <http://wasm.home.cern.ch/wasm/newprojects.html>.
- [78] S. Jadach. KKMC Status Report: <http://home.cern.ch/jadach/>.
- [79] B. P. Kersevan and E. R. Was. Processing generated events with TAUOLA and PHOTOS using the Athena interface: https://svnweb.cern.ch/trac/atlasoff/browser/Generators/Photos_i/trunk/doc.
- [80] *The large hadron collider: Conceptual design*, CERN-AC-95-05-LHC, 1995.
- [81] *LEP design report*, CERN-LEP-TH-83-29, CERN-LEP-84-01.
- [82] ALICE Collaboration, *Alice: Technical proposal for a large ion collider experiment at the cern lhc*, CERN-LHCC-95-7, 1995.

- [83] ATLAS Collaboration, *The ATLAS Experiment at the CERN Large Hadron Collider*, JINST **3** (2008) S08003.
- [84] CMS Collaboration, *CMS, the Compact Muon Solenoid : technical proposal*, CERN-LHCC-94-38, 1994.
- [85] S. Amato et al., *Lhcb technical proposal*, CERN-LHCC-98-04.
- [86] ATLAS public website about Luminosity Public Results:
<https://twiki.cern.ch/twiki/bin/view/AtlasPublic/LuminosityPublicResults>.
- [87] ATLAS TRT Collaboration, *The ATLAS Transition Radiation Tracker (TRT) proportional drift tube: design and performance*, 2008 IOP Publishing Ltd and SISSA .
- [88] C. Gabaldon, *Electronic Calibration of the ATLAS LAr Calorimeter and commissioning with Cosmic Muon Signals*, J. Phys. Conf. Ser. **160** (2009) 012050.
- [89] G. Barrand et al., *GAUDI - The software architecture and framework for building LHCb data processing applications*, Proc. of CHEP (2002) .
- [90] The GLAST experiment:
http://wwwalt.tp4.ruhr-uni-bochum.de/tp4/experimente/glast_intro-eg.html.
- [91] HARP Experiment:
http://astronu.jinr.ru/wiki/index.php/HARP_Experiment.
- [92] K. S. Cranmer, *The ATLAS analysis architecture*, Nucl. Phys. B **177** (2008) 126.
- [93] M. V. Gallas et al., *ATLAS Detector Simulation: Status and Outlook*, IEEE Nuclear Science Symposium Conference Record (2005) .
- [94] Athena Pile-up Requirements:
<http://hep.physics.indiana.edu/~luehring/pile-up.html>.
- [95] ATLAS Collaboration, *Performance of the ATLAS Muon Trigger Slice with Simulated Data*, ATLAS note: ATL-PHYS-PUB-2006-000, 2008.
- [96] ATLAS internal website about Muon Trigger Documentation:
<https://twiki.cern.ch/twiki/bin/viewauth/Atlas/MuonTriggerDocumentation>.
- [97] S. Hassani et al., *A muon identification and combined reconstruction procedure for the ATLAS detector at the LHC using the (MUONBOY, STACO, MuTag) reconstruction packages*, Nucl. Instrum. Meth. **A572** (2007) 77.

- [98] T. Lagouri et al., *A muon identification and combined reconstruction procedure for the ATLAS detector at the LHC at CERN*, IEEE Trans. Nucl. Sci. **51** (2004) 3030.
- [99] K. Nikolopoulos et al., *Event-by-event estimate of muon energy loss in ATLAS*, IEEE Trans. Nucl. Sci. **54** (2007) 1792.
- [100] W. Lampl et al., *Calorimeter Clustering Algorithms : Description and Performance*, ATLAS note: ATL-LARG-PUB-2008-002.
- [101] ATLAS internal website about TopologicalClustering:
<https://twiki.cern.ch/twiki/bin/viewauth/Atlas/TopologicalClustering>.
- [102] ATLAS internal website about SlidingWindowClustering:
<https://twiki.cern.ch/twiki/bin/viewauth/Atlas/SlidingWindowClustering>.
- [103] M. Agustoni et al., *Electron energy scale in-situ calibration and performance*, ATLAS internal communication: ATL-COM-PHYS-2011-263.
- [104] ATLAS Collaboration, *Electron performance measurements with the ATLAS detector using the 2010 LHC proton-proton collision data*, CERN-PH-EP-2011-117. [arXiv:1110.3174v1](https://arxiv.org/abs/1110.3174) [hep-ex].
- [105] M. Aharrouche et al., *Energy Linearity and Resolution of the ATLAS Electromagnetic Barrel Calorimeter in an Electron Test-Beam*, 2006. [arXiv:physics/0608012v1](https://arxiv.org/abs/physics/0608012).
- [106] C. Anastopoulos, *Electron performance studies for the Higgs \rightarrow 4 lepton search in proton-proton collisions at $\sqrt{s} = 7$ TeV, with the ATLAS detector at the Large Hadron Collider*. PhD thesis, Sheffield University, 2010.
- [107] M. Aharrouche et al., *The ATLAS liquid argon calorimeter: Construction, integration, commissioning and combined test beam results*, Nucl. Instrum. Meth. **A581** (2007) 373–376.
- [108] ATLAS Collaboration, *Performance of the ATLAS electromagnetic calorimeter for $\pi^0 \rightarrow \gamma\gamma$ and $\eta \rightarrow \gamma\gamma$ events*, ATLAS conference note: ATLAS-CONF-2010-006.
- [109] J. Adelman et al., *ATLAS offline data quality monitoring*, J. Phys. Conf. Ser. **219** (2010) 042018.
- [110] S. Agostinelli et al., *Geant4 - A Simulation Toolkit*, Nucl. Instrum. Meth. **A506** (2003) 250.

- [111] A. Sherstnev and R. Thorne, *Parton Distributions for LO Generators*, Eur. Phys. J. **C55** (2008) 553.
- [112] M. Aharrouche et al., *Supporting Document: Total inclusive W and Z boson cross-section measurements and cross-section ratios in the electron and muon decay channels at $\sqrt{s} = 7$ TeV*, ATLAS internal communication: ATL-COM-PHYS-2010-703.
- [113] S. Moch and P. Uwer, *Heavy-quark pair production at two loops in QCD*, Nucl. Phys. Proc. Suppl. **183** (2008) 75, [arXiv:0807.2794](https://arxiv.org/abs/0807.2794) [hep-ph].
- [114] ATLAS internal website about Muon Girl:
<https://twiki.cern.ch/twiki/bin/viewauth/Atlas/MuGirl>.
- [115] ATLAS internal website about Muon Performance:
<https://twiki.cern.ch/twiki/bin/viewauth/AtlasProtected/MuonPerformance>.
- [116] M. Aharrouche et al., *Measurement of the response of the ATLAS liquid argon barrel calorimeter to electrons at the 2004 combined test-beam*, Nucl. Instrum. Meth. **A614** (2010) 400–432.
- [117] T. Kubota and T. Matsushita, *Muon trigger SFs for Moriond 2012 w.r.t staco combined/loose*, 2012.
https://twiki.cern.ch/twiki/pub/Atlas/TrigMuonEfficiency/sf_moriond.pdf.
- [118] ATLAS Collaboration, *Updated Luminosity Determination in pp Collisions at $\sqrt{s} = 7$ TeV using the ATLAS Detector*, ATLAS conference note: ATLAS-CONF-2011-011.
- [119] ATLAS internal website about FSR Study:
<https://twiki.cern.ch/twiki/bin/viewauth/Atlas/FSRStudy>.
- [120] OPAL Collaboration, *A measurement of photon radiation in lepton pair events from Z^0 decay*, Phys. Lett. B **273** (1991) .